Flinders UNIVERSITY
ADELAIDE · SOUTH AUSTRALIA

Implementation of the Hexapod Cradle

By

Tiffany Yuen-Munn Teh

Supervisor: Associate Professor John Costi

A thesis submitted to the College of Science and Engineering in partial fulfilment of the degree of Master of Engineering (Biomedical)
Flinders University, Adelaide, Australia
October 2018

Abstract

The study of biomechanical function provides beneficial insight into human motion, injury, rehabilitation and surgical techniques. Flinders University have a six degree of freedom Hexapod robot which performs in-vitro biomechanical testing. The Hexapod can only mimic flexion and extension of approximately 50° which means that specimens such as elbows and knee are unable to reach full range of motion. The purpose of this thesis was to increase the range of motion to test as many joints as possible. A cradle device was designed to insert into the inner space of the Hexapod while simulating flexion and extension. Crucial requirements included successfully synchronising movement between the cradle and Hexapod assembly while closely imitating physiological joint motion and load.

A major design requirement was to increase the range of motion of the cradle while avoiding collision between the cradle device and moving encoders. These encoders make up the inner space of the Hexapod. Due to the tight space, a computational model and physical prototype was created to ensure accuracy. There was a strong association between these measurements. The cradle was designed to create 140º flexion while avoiding any collisions between the cradle and Hexapod.

Static and dynamic requirements determined the stiffness and motor specifications of the cradle device. These requirements were based around joint specimen failure loads and motion found in the literature. Finite Element Analysis was performed to analyse the stiffness of the cradle at certain flexions. Reiterations of the design were made according to these results. Stiffnesses were in the range of 3701 – 17334.3 N/mm which complies with biological specimen and hexapod stiffnesses. However, undesirable displacements were found at 3.07 mm. Next, motor and gearbox selections were analysed based on the dynamic simulation requirements. A superior actuator with a unique strain wave gear was identified as a suitable actuator to integrate into the cradle system. This motor consisted of 58 Nm continuous torque with a compact actuator length of 93 mm, this satisfies walking loads and motion however it will not be capable of withstanding failure loads and motion.

A suitable plan included manufacturing the cradle with a lock system to validate the structure followed by integrating the SHA series actuator into the system at a later point in time. Future work will include further structural analysis, manufacturing, generating funds and integrating this actuator into the complex hexapod control system.

Declaration

I certify that this thesis does not incorporate without acknowledgment any material previously submitted for a degree or diploma in any university; and that to the best of my knowledge and belief, does not contain any material previously published or written by another person except where due reference is made in the text.

Tiffany Teh

15/10/2018

Acknowledgements

I appreciate the time, support, patience and guidance provided by my supervisor, Associate Professor John Costi. He provided me a space to explore challenges in a field I wasn't too familiar with. Thank you to the whole Engineering Services Group at Flinders University. Almost every single one of them has assisted me with laser cutting, printing, electronics or advising me on ideas. Thank you to Michael Russo who controlled the Flinders Hexapod during prototype validation. Finally, thank you to my family, housemates and friends who have provided me with support during busy times.

Table of Contents

List of Figures

List of Tables

Chapter 1 Introduction

1.1 Background

The United Nations Population Fund reported that the percentage of elderly people will triple by 2050 (UNFPA 2009). As life expectancy rises, worldwide health issues become an increasingly larger problem (Scully 2012). Musculoskeletal disorders are a key health issue for the ageing population (Woolf 2000). From 1990 to 2010, Hoy et al. (2014) found that musculoskeletal conditions increased by 60% in developing countries. Woolf and Pfleger (2003) discuss four major musculoskeletal conditions identified by the World Health Organization (WHO). These include; lower back pain, osteoarthritis, rheumatoid arthritis, and osteoporosis. They found that osteoarthritis affects 18% of women and 9.6% of men over 60 years of age. The degeneration of cartilage between joint surfaces triggered osteoarthritis to be the 4th largest cause of joint replacement (Woolf and Pfleger 2003). Osteoporosis is prone to cause hip fractures due to low bone mineral density and weakening of microarchitectural structure. Woolf and Pfleger (2003) also found 20% mortality in the first year after fractures and a 50% permanent loss of function. Additionally, lower back pain is a burden that almost all the population face at one time or another. These conditions effect quality of life, mobility, joint pain, inflammation, independence, the health care system and its related costs.

Furthermore, the WHO found that obesity has more than doubled, worldwide, since 1980 (WHO 2011). Anandacoomarasamy et al. (2007) identified a significant correlation between obesity and musculoskeletal problems. This is due to additional weight exerting stress on joints and bones and in turn affecting gait and other aspects of human motion. The impacts of these issues involve serious problems for the developing world. The health care system will require larger funds for resources, medical devices, training and staff. An even greater physical and mental burden will be put onto individuals requiring support, as well as their carers and family members. While musculoskeletal research is performed, in vitro methods are based on the capabilities of the robotic simulator. It is crucial that more effective solutions, treatments and preventions are found to efficiently improve patient's quality of life and mobility.

Biomechanical studies are used to research musculoskeletal problems. Biomechanics is the study of biological systems using mechanical principles (Ünal, Akkuş, and Marcus 2016). Mechanical measures such as stress and strain are used to examine joints, cartilage, bone, ligament, muscle, tendon etc. and their interactions. Studying the highly complex coordination of these structures will result in a better understanding of human movement, injury and musculoskeletal problems. In turn, this will improve clinical solutions, treatments, prevention, rehabilitation devices and surgical techniques. These biological structures are usually studied using in-vivo, in-vitro and computational modelling methods. This thesis will focus on in-vitro methods.

In-vitro testing involves experiments on cadaver specimens (Bell et al. 2013). Specimens like the knee, hip, spine, ankle etc. can be put under physiological loading conditions to obtain data. The data provides clinically relevant information. In-vitro testing is a key stage in developing an implant, validating a model or discovering more about a structure and how to repair it. For example, testing machines can be used to understand the soft tissue interactions during knee stability (Fukubayashi et al. 1982). These experiments normally involve robotic simulators to replicate human movement. This is a non-trivial task as robotic capabilities may not be sufficient (Fujie et al. 1994). Biomechanical testing machines require mathematics to describe joint motion kinematics and its coordinate system, the manipulator to reconstruct 3D motion along a translation and/or rotation and sensors to measure data. The limitations lie in these variables.

Fukubayashi et al. (1982), among other studies, used a one-axis Instron testing machine which only allowed for testing in one direction. This had to be improved as it didn't allow for movement in three dimensions (Grassmann et al. 1998). In the late 1980's and early 1990's more complex biomechanical robotic testing systems appeared in the literature (Lewis, Lew, and Schmidt 1988; Fujie et al. 1994; Fujie et al. 1993). They allowed for a more accurate simulation of 3D joint motion. This type of testing allowed for unconstrained movement in the other axes. Spine and knee testing were primarily looked at during the 1980's-2000's. During the 2000's, more hip studies begun to appear in the literature. The two main 3D testing systems found in the literature were serial universal force-moment sensor systems (Woo et al. 1999; Mae et al. 2001) and parallel Stewart platform systems (Stokes et al. 2002; Walker and Dickey 2007; Ding et al. 2011).

Ding (2014) developed a custom Stewart platform-based manipulator, herein referred to as the Flinders Hexapod since it is located at Flinders University. The Flinders Hexapod is an excellent 6DOF testing machine however it is limited by its relatively small 50° range of motion. The motivation for this thesis was to improve the range of motion of this manipulator to allow for testing of joints such as the knee, hip, ankle etc. This is an important research aim as this will increase the research depth for in vitro biomechanics at Flinders University. Integrating the ability to test various joints of the body into one simulator will allow for flexibility with different joint specimens and tests that will aid in decreasing costs, resources and time. Chapter 1 will continue by exploring the literature in Section 1.2, followed by a past contribution from a previous student in Section 1.3 and Sections 1.4, 1.5 and 1.6 will introduce the aim of this thesis, discuss the project requirements and outline the subsequent chapters throughout this thesis.

1.2 Literature Review

This literature review will outline the types of biomechanical systems present in the literature, as well as analyse their uses and highlight the need for an improvement to the Flinders Hexapod. Section 1.2.1 will discuss joint kinematics and types of maximum physiological loads found. Section 1.2.2 will explore types of biomechanical testing systems that are in the literature. These include individual joint specific robots, serial robots and Stewart Platform robots. Section 1.2.3 will briefly discuss control methods for testing. Section 1.2.4 will discuss the Flinders Hexapod, which this thesis is based on, and Section 1.2.5 will compare the biomechanical testing systems found in Section 1.2.2 with the Flinders Hexapod from Section 1.2.4.

1.2.1 Joint Kinematics

The requirements of robotic capabilities are dependent on in-vivo joint kinematics. Replication of daily human motion and physiological conditions need to be simulated. The stresses put on joints and interactions between soft tissues leads to complex testing. The term, degrees of freedom, is used to mechanically describe a type of human kinematic motion that may occur. Motion in three-dimensional space is described using six degrees of freedom (6DOF) (Figure 1.1). The x-axis shows rotational flexion/extension with a left/right lateral shear. The y-axis demonstrates translational compression/decompression and an axial

rotation. Finally, the z-axis is translating in an anterior/posterior direction with left/right lateral bending. Biomechanical testing machines need to aim at replicating these movements realistically. Maximum loading, speed and range of motion that a joint will undergo need to be understood to robotically simulate daily activity and causes of joint failure.

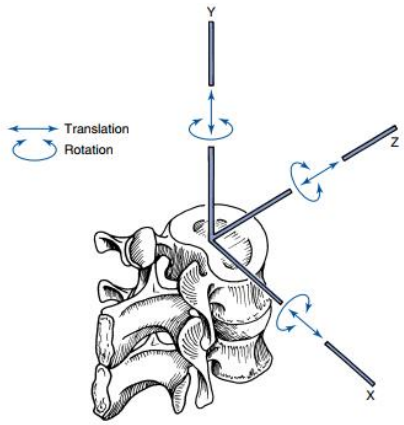

Figure 1.1 Describing six degrees of freedom along the x-y-z axes. One degree of freedom refers to one type of movement along a single axis. These movements include translation and rotation. Therefore, one axes has two degrees of freedom. Three orthogonal axes are used to describe 6DOF (Bergmann and Peterson 2010).

The lower extremities include the hip, knee and ankle joints whereas the upper body includes the shoulder, elbow, wrist and spinal joints. There is a unique range of motion depending on function for each joint and therefore movements vary greatly. The hip performs very versatile movements. Roaas and Andersson (1982) found large end ranges of motion depending on the person with flexion ranging from 90° to 150° while extension behind the midline varies between 0 to 35°, adduction/abduction range was 15° to 55°/15° to 45° and internal/external rotation ranged from 20° to 50°/10° to 55°. The knee joint primarily performs flexion and extension between 0 to 120°. However, Qi et al. (2013) found maximal flexion to be 155°. Similarly, elbow joints flex and extend to 150° with a daily activity range of 100°. Elbows also include varus/valgus rotation and pronate to 75° while supinate to 85° (Tashjian 2016). Meanwhile, the shoulder joint is the hardest to simulate due to its 360° range of motion. This means all-purpose robots need to include a large working space to cater for all motion ranges and joints. It is critical that flexion and extension beyond 120° is possible to allow for adequate daily motion during static and dynamic tests.

Joints undergo large repetitive loading during daily activities and injury prone activities. During vertical jumping and landing, Cleather, Goodwin, and Bull (2013) found landing from

a travelling jump loaded the knee joint 10.4 times the body weight. While a hip joint peak loading was found to be approximately 7.8-8.7 times a person's body weight (van den Bogert, Read, and Nigg 1999; Bergmann, Graichen, and Rohlmann 1993; Cleather, Goodwin, and Bull (2013). A male that weighs 85 kg would need to withstand approximately 7000 N in their hip joint while jumping. Cleather, Goodwin, and Bull (2013) also found the ankle experienced 8.9-10 times body weight. These are all based on extreme movements, and most importantly, that is when injuries occur. Additionally, during upper body movement a common elbow injury is overhand pitching. A pitching motion refer to the all being lifted above the head and as far back as possible then thrown forward. Due to the internal arm rotation action velocities beyond 7000°/s were found with a valgus torque between 64-120 Nm (Tashjian 2016). Joint kinematics is crucial in determining the robot's capabilities.

Table 1.1: Summary of maximum values of lower limb joints.

Joints	**Range of motion (°)**	**Loading**	**Velocity (°/s)**	**Torque (Nm)**
Hip	150 flexion 35 extension (Roaas and Andersson 1982)	7.8-8.7 x BW travelling jump Cleather, Goodwin, and Bull (2013)	570.09 ± 58.44 SD flexion (Zhong et al. 2017)	455.2 ± 198.7 SD in extension (Sun et al. 2015)
Knee	143.8 flexion (Roaas and Andersson 1982)	10.4 x BW travelling jump Cleather, Goodwin, and Bull (2013)	666.92± 112.87 SD extension (Zhong et al. 2017)	218.6 ± 131.0 SD in flexion (Sun et al. 2015)
Ankle	39.7 flexion 15.3 extension (Roaas and Andersson 1982)	9.8-10 x BW travelling jump Cleather, Goodwin, and Bull (2013)	928.19 ± 112.87 SD plantarflexion (Zhong et al. 2017)	234.57± 44.0 SD dorsal extension (Hahn et al. 2011)

1.2.2 Biomechanical Robotic Systems

From the 1990's till now, testing machines have become more accurate due to more complex robotics, control systems and testing methods. Therefore, in vitro testing has become a booming field which greatly benefits the study of human joint function. There are a wide range of biomechanical testing machines. They range from joint specific to universal manipulators. Each robot has their advantages and disadvantages. These will be discussed and outlined during this section.

1.2.2.1 Joint Specific Testing Systems

1.2.2.1.1 Oxford Knee Rig

Zavatsky (1997) validated the Oxford Knee Rig which is a custom-built design specifically for knee joints (Figure 1.2). The Rig was mathematically validated using a 6x6 matrix describing the kinematics (Zavatsky 1997). These simulators are used widely. Coles, Gheduzzi, and Miles (2014) used a version of the oxford rig to investigate patellofemoral joint pain after a total knee arthroplasty. The action of hamstring movement was simulated via actuation of the quadriceps. This study validated realistic physiological loading of 43Nm peak flexion.

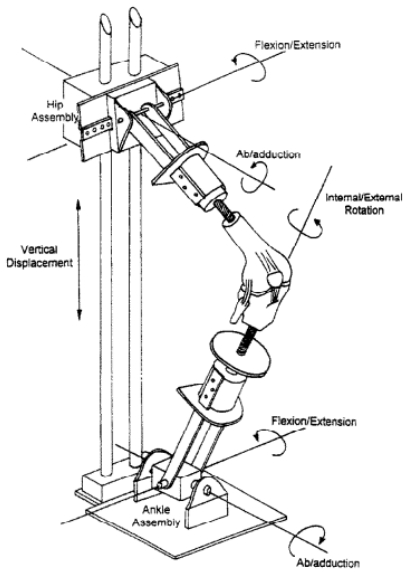

Figure 1.2 Oxford Knee Rig. The fixture at the top is designed to mimic a hip joint while the bottom fixture mimics an ankle joint. There is a rotary bearing located at the ankle assembly and two bearings located at the hip assembly. This allows for all movements created via a simulated hip and ankle. The hip assembly can also take on vertical loads to simulate body weight and displace to move the system vertically (Zavatsky 1997).

Further developments were made by Verstraete and Victor (2015) to improve on the rig. They constrained the hip translation while two servo actuators were used to control the vertical and horizontal position of the ankle assembly. The control system is run via LabVIEW where separate control loops were used for position feedback in a PID loop and each servo actuator. Similar knee rigs have been developed (Chevalier et al. 2017; Annemieke V 2013).

1.2.2.1.2 Elbow testing simulator

An elbow testing apparatus was designed and tested by Ferreira, Johnson, and King (2010) (Figure 1.3). The brachialis, bicep and triceps muscles were activated by servo motor actuators and attached via cables. Strain gauges were used for load feedback on the given muscles. An electromagnetic tracking system is used to transmit elbow kinematics and flexion angles to a receiver fixed on the ulna. One of the given muscles is chosen as the prime mover and then a predetermined motion profile produces a constant flexion rate in varus, valgus or horizontal positions. Active flexion produced more repeatable joint kinematics then passive flexion.

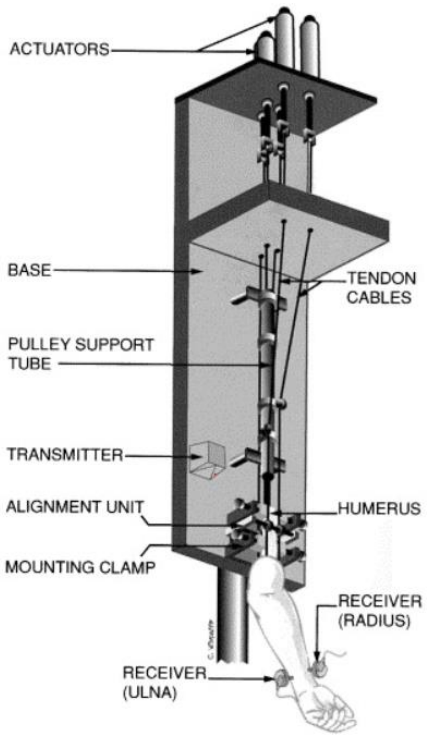

Figure 1.3 Elbow testing apparatus (Johnson et al. 2000).

1.2.2.1.3 Serial robotic testing systems

The serial robot also known as the universal force-moment sensor testing system is one of the most widely used robots in the literature. It is traditionally a commercialized serial robot with custom modifications. It has six degrees of freedom due to its three rotational pivot points. The KUKA KR 60-3 robot includes a bottom pivot point of +35° to - 135°, a middle pivot points of -120° to +158° and the top pivot of ±185° (Wijdicks et al. 2013). This allows for a large workspace of movement. This is a key strength for the serial robot as it is necessary to simulate realistic range of motion. However, unfortunately, the maximum loading capacity is only 589 N (Goldsmith et al. 2014) and joint loading can be significantly greater. Different universal force-moment sensor testing system (UFS) will have slightly different setups however they all include the three pivot points with the end effector connected to the specimen. (Figure 1.4).

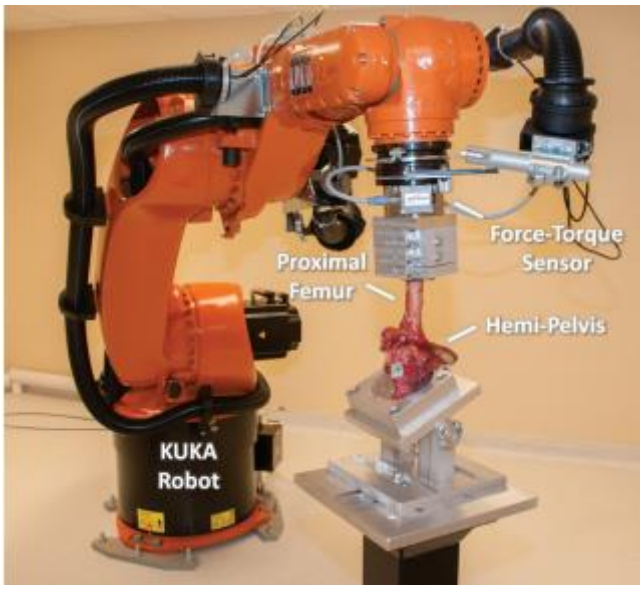

Figure 1.4. KR 60-3 KUKA Robotics Corp This shows the KUKA robot that has a hip specimen fixed into the end effector and the base fixture. There are 3 rotational points which allow the robot to move in 6DOF (Marc et al. 2017).

Simple UFS simulators have been available since the early 1990's (Fujie et al. 1993; Fujie et al. 1994; Woo et al. 1999; Mae et al. 2001; Mabuchi et al. 1992). During this period of time, simulators were custom designed knee experiments that allowed for 6DOF testing. The knee joint was fixed into a rigid fixture at the base and into the potted specimen in the end effector. Thomas et al. (2006) & Mae et al. (2001) prepared the specimen by dissecting the knee joint 15 cm proximally and distally. This allows for stable fixation. Woo and Fisher (2009) used in

vivo kinematic data to validate its mathematical model of the knee and the robot's capabilities.

Anterior cruciate ligament (ACL) and posterior cruciate ligament (PCL) studies were the main knee studies found in the literature (Wijdicks et al. 2013; Mae et al. 2001; Ohori et al. 2017). Flexion/extension motion between 20-120° was generally performed to allow for creep. Mae et al. (2001) examined ACL constructions by applying 100 N of tibial load at 0°, 15°, 30°, 60°, and 90° of flexion to observe the tibial displacement. Ohori et al. (2017) investigated varus/valgus instability in a deficient ACL. This involved testing at 5 Nm varus/valgus torque loaded at 30° and 60° where the force and moment of the tibia relative to the femur was observed. Another study included an assessment of knee stability by applying 88 N of tibial load at 0°, 20°, 30°, 60°, and 90° of flexion. A combination of 10 Nm valgus and 5 Nm internal tibial torques were applied for flexion between 0° to 30° (Wijdicks et al. 2013).

Hip joint in-vitro studies using the UFS became more common in the 2000's. Marc et al. (2017) explain the need for more understanding of the hip stabilizers by determining further information on hip range of motion and repair conditions. Hip studies use the international society biomechanics recommendation to establish hip joint coordinates (Van Arkel and Jeffers 2016). Marc et al. (2017) highlight the design of the UFS where the hemi pelvis potted with PMMA into the rigid fixture and the femur is fixed into the robot end effector (Figure 1.4). The femur was cut 15cm distal to the greater trochanter (Debski et al. 2017; Goldsmith et al. 2015). After neutral alignment was found, passive hip joint position and orientation was observed by applying 10 N of compressive force during flexion of 10° to extension of 100° in 1° increments (Debski et al. 2017; Goldsmith et al. 2015). Lertwanich et al. (2016) performed a study on the labrum's contribution to joint stability. The passive flexion/extension path was performed by moving the femur between 0° and 30° of flexion in 0.5° increments. This study used different loading conditions for flexion between 0 – 30°. Loading included an 80 N axial force on the femoral shaft, combined 80 N axial/60 N anterior force, combined 80 N axial/60 N anterior force and a combined 80 N axial/60 N lateral force.

1.2.2.2 Stewart Platform Testing Systems

Stewart platforms are widely used for applications such as flight simulators and space telescopes (Furqan, Suhaib, and Ahmad 2017). The parallel robot consists of six legs that retract and extend. They are attached to a rigid fixed base and a mobile top plate. A simple Stewart Platform manipulator is shown in Figure 1.5. The movement of all six legs allows for 6DOF motion. The legs are attached to the top and bottom plate via flexible joints. Due to their useful mechanical design they provide high stiffness, position accuracy and a large load capacity. These are all desirable requirements for biomechanical testing (Walker and Dickey 2007).

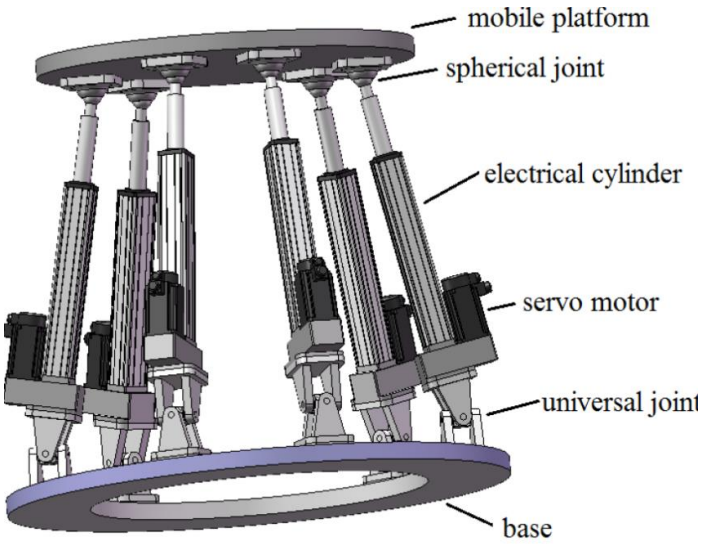

Figure 1.5 A basic Stewart Platform. This shows fundamental parts of a Stewart platform design. It includes a base with six servo motors and encoders attached via a universal joint. These extend and retract to allow the top mobile platform to move (Duan, Mi, and Zhao 2016).

Stewart platforms usually come in two configurations. The specimen is either mounted on top of the Stewart platform with an external frame or within the inner space of the device. Walker and Dickey (2007) & Stokes et al. (2002) use the inner space for specimen fixation whereas Noble et al. (2010) & Colbrunn et al. (2013) fixate the specimen to the top of the Stewart platform. There are positives and negatives to both. The specimen mounted on top of the Stewart platform will allow for a larger working space however mounting the specimen within the inner frame allows for less additional fixtures. Additional fixtures may affect specifications of the initial system and robot compliance leading to an inferior system. Thus, it is important to maintain the integrity of the fundamental design.

1.2.2.2.1 Rotopod R2000

Noble et al. (2010) designed and validated a general robotic testing system to allow for testing of various joints. Their focus was to validate knee and foot systems by simulating physiological loads, scaled velocities that simulate real time dynamics, loading conditions like running and jumping. The Rotopod is set up with the required servomotors and fixture to simulate joint motion. The specimen is mounted onto the top of the Rotopod with a platform size of 780 mm in diameter and six linear actuators with a 50 mm stroke. The Rotopod has a load capacity of 2000 N and a torque capacity of 1000 Nm. It has a translational and angular velocity of 100 mm/s and 120°/s respectively. The x and y axis have a ±110 mm translation with a ±13° roll/+12° to – 19° pitch and a z axis translation of ±93 mm with a rotation of ±720°. These specifications allow for simulated kinematics beyond walking. Other rotary actuators are chosen due to their velocity and acceleration specifications. The actuator has a maximum velocity of 0.4 m/s and an acceleration of 120 m/s². Its peak static force is 6110 N with a constant force of 1880 N. A MicroScribe is used to obtain spatial data for the rotopod, external load sensor and specimen. Other devices such as a force platform are used to obtain ground reaction forces, as well as a six-axis load cell to measure loads.

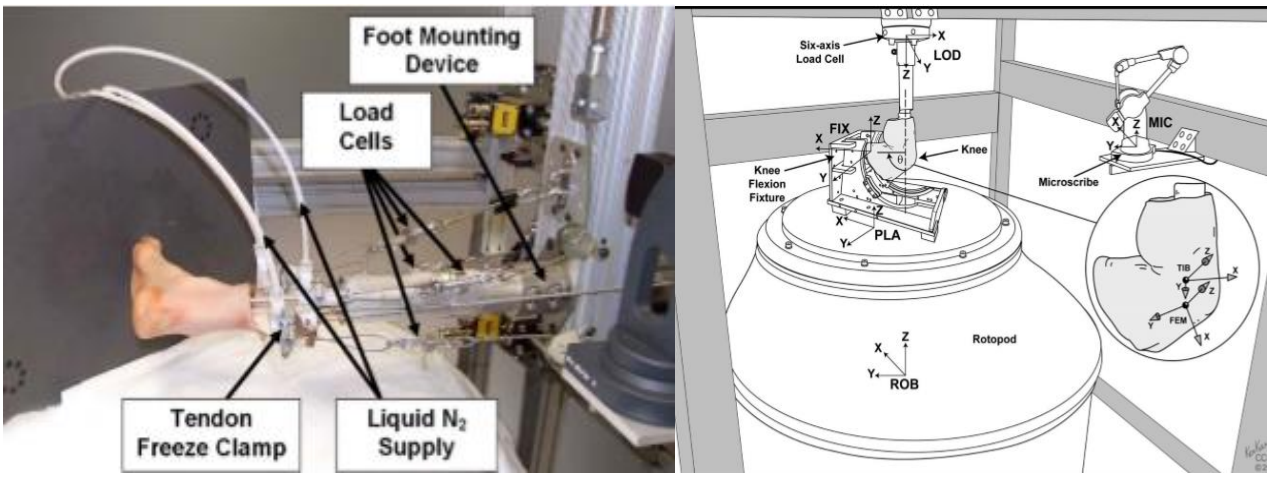

Figure 1.6 The foot and knee configurations. The R2000 Rotopod sits underneath these two additional devices. The left figure shows the ground force plate and the actuators and load cell which are connected to the ankle. The right figure shows a flexion knee fixture which extends and flexes within the fixture. The femur is connected to a sex axes load cell (Noble et al. 2010).

The setup of the knee and foot simulator systems include various additional parts (Figure 1.6). For the foot test, the ground simulator will move via the Rotopod. This foot study simulates one fourth walking speed with varying body weight percentages to simulate gait

kinematics. The ground reaction forces can then be obtained. The knee experiment includes the tibia attached to a load frame while the femur is attached to the flexion fixture to harmonize with the joint coordinate system (Figure 1.6). Either hybrid control or position control can be used. Mutnal et al. (2015) also used the same knee configuration for a posterior cruciate ligament reconstruction study. Various loading conditions were applied to 0°, 30°, 60°, 90°, and 120° of flexion.

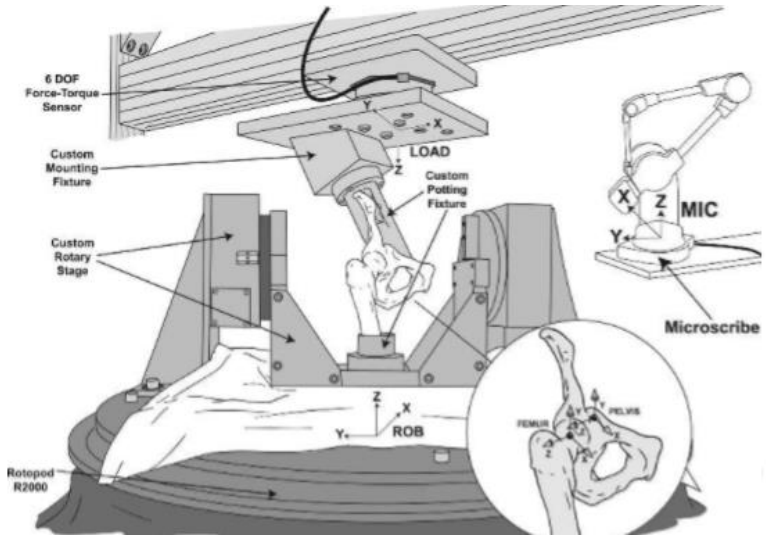

Figure 1.7 Rotopod R2000 hip simulator configuration. This demonstrates a custom rotary stage that sits between two pillars and rotate around the pivot point. It is attached to a custom mounting fixture (Colbrunn et al. 2013).

Another form of fixture can be used on the top of the Rotopod (Figure 1.7). The custom rotary stage will drive the femur in a flexion/extension like motion. Other movements will be created via the Rotopod. Colbrunn et al. (2013) dissected the femur 225 mm from the greater trochanter to enable fixation and potting with an implant. The hip was dissected to secure it to the custom potting fixture. Colbrunn et al. (2013) investigated impingement and stability during a total hip arthroplasty compared with hip resurfacing. The hip was placed in two positions most at risk of dislocation: 0° flexion externally rotated and 10° adduction/90° flexion internally rotated. The joint was rotated anteriorly or internally in the posterior motion until impingement occurred. (Bonner et al. 2015) also performed a study on impingement however they observed the labrums contribution to hip joint stability via a 100 N load on the acetabulum while producing a 2°/s sweep perpendicular to acetabulum until sublaxation occurred. Another study involves Chokhandre et al. (2015) studying joint laxity where flexion angles between 0° to 90° were analysed with internal/external moment between 0 to

±5 Nm, varus/valgus moment from 0 to ± 10 Nm and anterior/posterior forces from 0 to ±100 N.

1.2.2.2.2 Custom Built Parallel Robots

Stokes et al. (2002), Walker and Dickey (2007) & Ding et al. (2011) established custom built Stewart Platform designs with the specimen in the inner space of the actuator legs. The specimens are bolted to the top with the load cell and to a rigid bottom underneath. This can be seen in Figure 1.8. Stokes et al. (2002) designed this testing system for spinal segments. It consists of six linear actuators and encoders. The encoders are glass scales and optical read heads with a 2.54 µm resolution. Since the linear encoders and the actuators are not actually linked, they are independent of the load cell and actuator. Walker and Dickey (2007) also created a custom-built design for spine testing. They attempted to control the robot through position and force control however there were position errors and robot compliance in 6DOF due to hardware. The Flinders Hexapod will be discussed in the last section of the literature review (Ding et al. 2011).

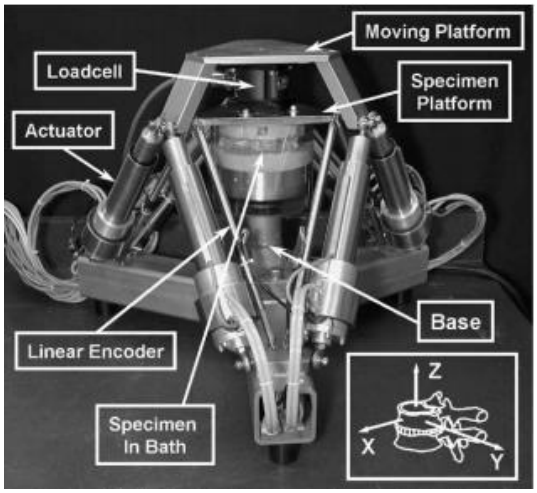

Figure 1.8. Custom built Stewart platform. This hexapod shows the specimen mounted inside the hexapod. (Stokes et al. 2002).

There is a large depth for biomechanical robotic simulators in the literature however there is not a lot of detailed information about designs and specifications. These factors are extremely crucial when performing experiments. Validity of results during experiments rely heavily on the accuracy of the robot. This thesis will be based on the Flinders Hexapod introduced in Section 1.2.4. Therefore, a comparison on the key robots will be discussed in 1.2.5.

1.2.3 Robotic Controlled Testing Methods

Testing methods are vital to ensuring accurate joint motion. Earlier methods of testing usually occurred along one axis of translation which produces constrained loading (Fukubayashi et al. 1982). This meant that the other five degrees of freedom cannot move. This does not replicate joint motion (Grassmann et al. 1998). 6DOF systems allow for unconstrained methods where a pure moment or force can be applied to one degree of freedom and the others are free to displace. Fujie et al. (1996) mathematically described this method by using a 6x6 Jacobian matrix to describe the forces and moments. This allowed for load and displacement-controlled methods. Load control occurs by loading a joint in one axis with a specific force or moment to obtain displacement data whereas displacement control changes the displacement of the joint and load changes are observed. An advantage of displacement control is the rate of displacement can be controlled which allows the robot to be more compliant (Fujie, Sekito, and Orita 2004). Load control can be challenging. Incremental displacements or a control algorithm will change dependent on the target load. This is very dependent on the robot's accuracy and precision. Specimen stiffness and error need to be calculated and updated to avoid error (Walker and Dickey 2007).

The first novel application of velocity based force control for unconstrained spine test was performed by Goertzen and Kawchuk (2009). They explored a velocity-based control for biomechanical testing that isn't dependent on stiffness of the specimen. The goal is for the axis of rotation to follow the specimens preferred motion. This is in the hopes that there is simplicity, stability and performance in biomechanical testing. A jog function was created to adjust the velocity for each axis in proportion to force errors while limiting the maximum velocity of the system. A force error window was used to alter the velocity in position control. The force error window is used to minimize overshoot, maintain stability and a velocity threshold. This runs at a frequency of 20 Hz. Since this study, continuous joint loading has been performed during various hybrid-controlled studies (Debski et al. 2017; Bell et al. 2013; Bell et al. 2015).

1.2.4 Flinders Hexapod Robot

Ding (2014) developed a novel 6 DOF Stewart platform used to perform biomechanical testing. It is based at Flinders University, Australia. This is the manipulator used during this thesis. The hexapod is made up of six VT209 linear ballscrew actuators with a DC brushless rotary servomotor. Each actuator can generate 4 kN with a maximum linear velocity of 200 mm/s and a stroke length of 178 mm. There are also six linear encoders with optical read heads providing a resolution of 0.5 µm. These parts can be seen in Figure 1.9. A maximum of 23000 N of vertical force and 1500 Nm of axial torque can be exerted. It has a position accuracy of ±0.02 mm and a rotational accuracy of ±0.02°. The specimen will be fixed between the mobile top plate connected to the load-cell and a rigid base. The servomotor and actuator change the position of the top plate.

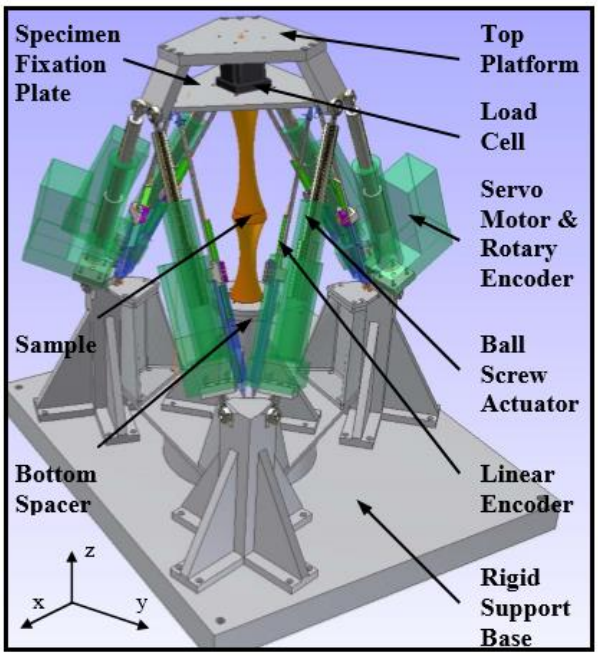

Figure 1.9. A virtual image of the Flinders Hexapod. This is a CAD image of the Flinders Hexapod. It sits on three rigid pillars. Two servomotor and rotary encoders are connected to each pillar which forms the six legs. The sample shows where the specimen will be placed. The load cell sits beneath the top platform which creates the 6DOF motion (Ding et al. 2011).

The movement of the top plate is restricted by the actuators. This means that there can only be a maximum angular rotation of ±25° in flexion/extension and lateral bending and ±20° in axial torque. This means the design is not capable of simulating regular motion of joints such as the knee, hip, elbow etc. This is the designs key downfall.

The control system structure is shown in Figure 1.10. The user programs the robot through LabVIEW which directly communicates, via Ethernet, to the Soloist (motor) controllers and the PXI-8106 Real Time Controller. The Soloist Controllers control the Servomotors while the PXI-8106 will communicate the field programmable gate arrays (FPGA) to collect and send data, determine the robot's kinematics and detect error as well as implement safety. The FPGA will also communicate with the Soloist controllers to adjust the torque. The AMTI load cell will send data to the Real Time Controller and the FPGA while the Linear Encoders and Servomotors will communicate with the FPGA and the Soloist controller. This complex control system allows for accuracy and precision.

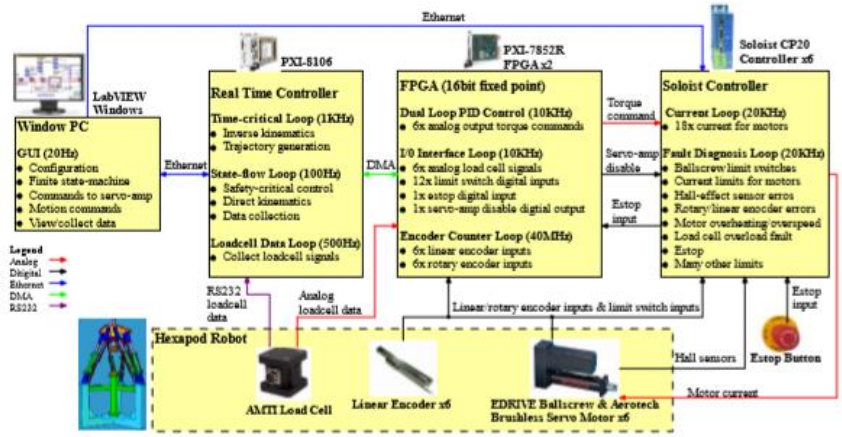

Figure 1.10. Control system structure. This describes the complete control system of the Flinders Hexapod. LabVIEW is used to control the Soloist controllers and the real time controller which is attached to the FPGA card. These systems communicate with the load cell, linear encoders and the servomotor (Ding et al. 2011).

The kinematic relationship of the hexapod is formed via the center of the specimen fixation bottom plate and the position and orientation of the linear encoders. A relationship between the specimen coordinate system and the end-effector (center of specimen fixation plate) coordinate system is established. This is shown in Figure 1.11. Then, the desired end-effector position and orientation is established. As a result, inverse kinematics is used to calculate the movement of the six robot legs for position command. The six soloist controllers will be communicating with the servo motors, rotary encoder and the linear incremental encoder in a PID control loop. There will be a dual loop as the rotary and linear encoders are in different positions. This is called non-collocation which improves accuracy and independent of load frame compliance from measurements. Furthermore, this will allow for backlash, instability and error control. The measured leg length will be fed back into the position command loop

to determine the next position. The 6-DOF load cell will collect the force and moments based on the position control.

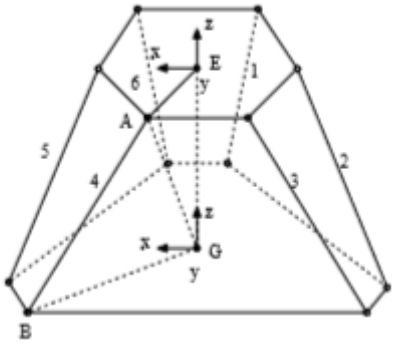

Figure 1.11. Inner sensing frame made up of linear encoders. This shows the kinematic relationship which drives the hexapod (Ding et al. 2011).

The hexapod has an adaptive velocity based control and hybrid force control to increase loading rate (Lawless et al. 2014). To achieve the control method the FPGA boards are used to implement feedback control. A 6x6 decoupled time-varying stiffness matrix with diagonal terms only will be used to represent the gain of the specimen stiffness. From this desired velocities and displacements are determined to change the position of the robot. The adaptive gain algorithm will send and receive load signals to adjust velocity from the previous second. Root mean square error, oscillation frequency and time weighted average of will be accounted for. The gain will be altered based on these factors. A hyperbolic sine function was used to damp out noise and smoothen out noise from the load cell. This is how the hexapod will adapt to system stiffness in real time.

1.2.5 Comparison of Biomechanical Robotic Systems in the Literature

Section 1.2.2 discusses biomechanical robotic testing systems in the literature. It was concluded that many in vitro studies use robotic machines however there isn't vast amount of literature based the design and specification of systems used. The main testing systems can be categorized into Serial, Stewart platform or custom joint specific testing machines. Therefore, an analysis can only be made about the robots that discuss their specifications and designs (Table 1.2). The main type of serial robot is the KUKA KR 60-3. It has high ranges of motion and speed however it has a low force capacity and stiffness. There is a trade-off between the large working space and the stiffness/maximum load capacities (Table 1.2). This is a concern because control, precision and repeatability are necessary when analysing joint kinematics

and forces. The other key system is the Stewart platform represented by the R2000 Rotopod and the Flinders hexapod. The R2000 Rotopod includes additional fixtures which are added on to the top of the Stewart platform depending on use. However, the flinders hexapod uses the inner space of the Stewart platform to fixate the specimen. The load capacity and velocities are significantly greater for the Flinders hexapod however the R2000 has a larger range of motion. The Flinders hexapod has superior specifications apart from the range of motion and workspace. This will be the focus of this thesis.

Table 1.2: Comparison of specifications on key biomechanical robots

6DOF Robots	**Load Capacity**	**Workspace**	**Velocities**	**Accuracy / repeatability**
***Serial Robot* – KUKA KR 60-3 (KUKA 2018)**	Max: 589 N	Maximum reach: 2033 mm Workspace: 27.2 m^3	-	Repeatability: <±0.06 mm
***Stewart platform Robot* – R2000 + additional knee fixture (Noble et al. 2010)**	Max: 2000 N Knee specific: Fx, Fy: 1500 N Fz: 3750 N Mx, My: 240 Nm Mz: 240 Nm	X-axis: ±110 mm Y-axis: ±110 mm Z-axis: ±93 mm Mz: ±13° Mx: ±13° My: +12° / -19° *Knee specific:* *Flexion: 120°*	Translational: 100 mm/s Angular: 120°/s	±50/25 µm
***Stewart platform Robot* – Flinders Hexapod (Ding et al. 2011)**	Max: 23000 N Torque: Mx, My: 2000 Nm Mz: 1500 Nm.	X & Y-axis: ±150 mm Z-axis: 90 mm Mx, My: ±25º Mz: ±20º	Translational: Fx: 480 mm/s Fy: 540 mm/s Fz: 210 mm/s Angular: Mx: 60°/s My: 63°/s Mz: 135°/s	Accuracy at 2 Hz Fx, Fy: 0.1 mm Fz: 0.07 mm Mx, My, Mz: 0.07°

There are many trade-offs between various biomechanical testing machines discussed in Section 1.2.2. All round superior testing systems are very rare. However, if the gap in the Flinders Hexapod can be bridged, it will allow for a very superior and valuable system. This

is because a variety of joints can be tested allowing for flexibility, a larger depth research and lower costs since other systems don't need to be created from scratch. Set ups for various specimen fixtures, testing methods and designs were noted as they may motivate ideas.

1.3 Past Thesis Contribution

A past Honours student, Bradley Hocking, wrote an Honours Thesis evaluating various mechanical designs to increase the range of motion capabilities of the hexapod (Hocking 2015). Different design options were analysed, and a cradle device was chosen as the most suitable. This device will be placed in the inner space of the hexapod. The concept is that the base is fixed to the specimen pillar with two stands attached. These two stands were attached to the cradle allowing for rotation (Figure 1.12). This was a very general concept requiring further investigation.

Figure 1.12. Cradle prototype from Bradley Hocking's Thesis (Hocking 2015).

1.4 Project Aim

The cradle design required further development before actually manufacturing a device and implementing it into the complex Hexapod system. Deeper investigation was necessary to understand the interaction of the cradle inside the hexapod. Complexities of the mechanical design were studied in detail and a motor was determined. A suitable motor is required to be compatible with the cradle design and hexapod control system. The aim of the project was to ultimately increase the range of motion within the hexapod. More specifically, the intention for this thesis was to properly develop the cradle device to be ready for manufacturing and realistically implemented into the Hexapod.

Achieving this aim ultimately increases the variety of joint specimen testing performed by the Hexapod. Due to its accuracy and ability to withstand high loads, the Flinders Hexapod already has a superior design to other biomechanical testing robots, however it is limited by range of motion in flexion and extension. A successfully implemented design into the Hexapod will be a substantial feat for the biomechanical research conducted at Flinders University. Great flexibility with one simulator accurately mimics many physiological loadings and motion of joints. Significant improvements through the cradle results in the ability to perform a greater variety of scientific tests and subsequently increases knowledge in understanding biomechanical movement, joint function, degeneration and injury. The integration and flexibility of the cradle also decreased the amount of resources, time and money spent on creating custom fixtures and devices for various experiments.

1.5 Cradle Design Requirements

Due to the nature of this project it was crucial that methodical engineering design processes are followed to ensure successful outcomes. Fulfilling the cradle requirements involved analysing and prioritising needs of the product by thoroughly analysing cradle function. The key overall requirements, as stated in the aim, was to increase the range of motion for the hexapod and closely mimic physiological joint loading via the cradle design.

Increasing the range of motion of the hexapod was achieved through the cradle device, however a critical necessity was that the cradle cannot collide with the hexapod. Safety of the cradle and hexapod interaction was a must have part of the design. This requirement was a complex task as the cradle and hexapod are both moving in a small space. Therefore, a key requirement was that the cradle geometry will not collide with the Hexapod even at its end ranges. The second major requirement was that the cradle mimicked physiological joint loading. This requirement was broken down into static and dynamic testing. These types of tests varied greatly since joints undergo many different testing scenarios. Testing may include recreating an injury, investigating ligaments and tendons of the joint, mechanical properties, validating prosthetic designs, observing forces and moments during cyclic or ramp tests, etc. An important static test may include failing a joint where a high load compression will be exerted onto the specimen and cradle. This led to investigating maximum loads and stiffnesses that the cradle needed to undergo. During static loading the cradle was held at

certain positions for long durations of time. Therefore, it was necessary for the design to include a locking mechanism and a durable cradle. Dynamic testing involved kinematic motion of joints, cyclic or ramp loading, compression testing as well as the control of the cradle and hexapod motion. Defined specifications determined measures such as fatigue, frequency, torque and dynamic loading. Consequently, a motor and gearbox selection was dependent on these specifications. Furthermore, the control system of the desired selection needed to be compatible with the current control system. These requirements are summarised in Figure 1.13.

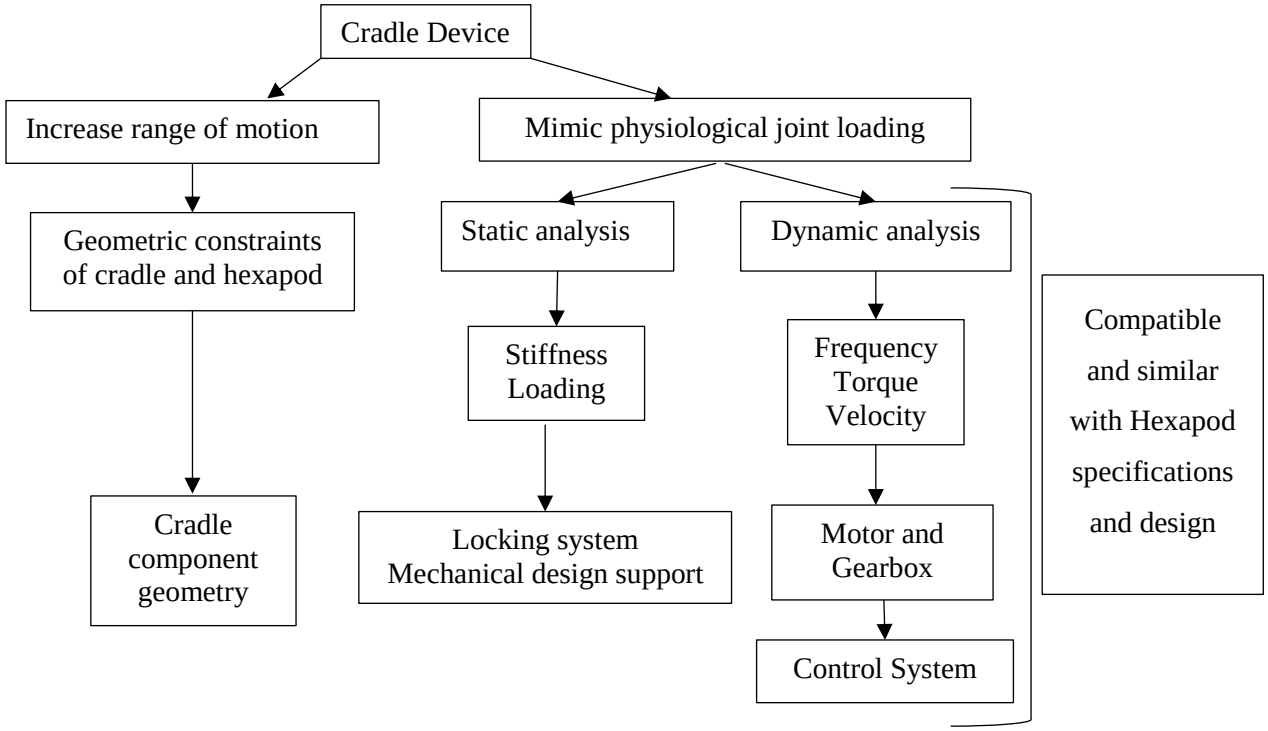

Figure 1.13. Design process tree for cradle device.

These requirements and function of the cradle device determined specifications and design methods. The design process tree determined three clear pathways that develop and detail concepts for a successful cradle design (Figure 1.13). Therefore, this thesis was be broken down in these three pathways forming one chapter each. Detailed and quantifiable specifications were discussed and analysed for each section followed by detailed design and selection processes. Other design requirements such as safety, reliability, cost etc were discussed through or during the final design stage.

1.6 Thesis Outline

Chapter 2 thoroughly analysed the geometric constraints for the cradle and hexapod assembly. Computational methods and kinematics were used to introduce the cradle as an additional degree of freedom to the hexapod. A description of its geometry in relation to the hexapod will be defined. Valuable information was provided for the size of the cradle and whether the cradle can interact with the hexapod at its end ranges of motion. The second section validates the computational calculations by a developed prototype and control system.

Chapter 3 discussed requirements of the cradle based on static testing. Finite Element Analysis (FEA) was performed to explore ideal stiffnesses and loads. Furthermore, the FEA determined redesigns of the cradle. A locking system for a static test was also discussed.

Chapter 4 explored the potential dynamic simulations the cradle was required withstand. The requirements determined a motor and gearbox selection required to automate the cradle and withstand dynamic biomechanical testing.

Chapter 5 compared designs through an analysis of advantages and disadvantages followed by an outline of the final design and a realistic development plan. This plan should bring the cradle design to fruition.

Chapter 6 concluded this thesis and discussed future work for the project.

Chapter 2 Geometric Constraints and Validation of Hexapod and Cradle Assembly

2.1 Introduction

Integrating the cradle design into the Stewart Platform simulator is the most critical and complex aspect of the design process. The Flinders Hexapod has 6DOF which will cause the encoders to move in space. The cradle adds another degree of freedom moving in this space which will result in a complex simulation. This simulation demonstrates seven degrees of freedom rotating and translating within a very compact space. Without deeply investigating these interactions and understanding the hexapod and cradle assembly at its end ranges, the cradle will collide with the encoders causing design failure. The inner space of the Hexapod is a huge limitation that will determine key aspects of the design. Furthermore, the largest joint flexion found in the literature was 150º of the hip (Roaas and Andersson 1982). The cradle design should aim to mimic this to allow for testing of numerous joints. Thus, the specification of cradle rotation should be as close to 150º as possible.

This chapter is dedicated to understanding and analysing the geometric constraints of the inner space of the hexapod and cradle assembly. The aim of this section is to use computational methods to understand repercussions of the mechanical device in the inner space of the hexapod and then validate it through a physical set up. Success of this chapter will fulfil the ultimate requirement of an increase in range of motion in the Hexapod. Section 2.2 explains necessary theoretical background for the chapter. Section 2.3 discussed fundamental cradle geometry. Section 2.4 consisted a thorough mathematical analysis of the cradle and Hexapod assembly. Section 2.5 discussed a prototype design and set up with the Hexapod and validation of results from Section 2.4. Finally, Section 2.6 form the discussion and conclusion for this chapter.

2.2 Theoretical Background

The theoretical background was highlighted to provide the reader with concepts and knowledge behind the motivation for methodology and work performed this section. Section 1.2.4 in the literature review provided a brief overview into the Stewart Platform Manipulator (Flinders Hexapod). This knowledge was assumed during this section.

2.2.1 Stewart platform kinematics

The Stewart platform kinematics, described below, involve the exact Hexapod kinematics developed by Ding (2014). Robotic simulators are described by spatial configurations, for instance, from frame {A} to {B}. Configurations were determined via translations and rotations of the current position and orientation. Position and orientation vectors were generally described via a matrix such as:

$$\mathbf{P}_B^A = \begin{bmatrix} x \\ y \\ z \\ \theta_x \\ \theta_y \\ \theta_z \end{bmatrix} \quad (2.1)$$

This was a vector pose at a certain frame during motion. $[x\ y\ z]^T$ described translation and $\left[\theta_x\ \theta_y\ \theta_z\right]^T$ described rotation in the x, y, z direction. $\mathbf{P}_B^A$ is a zero vector which denoted the robots original end effector position. The corresponding position vector at that frame was:

$$\boldsymbol{T}_B^A = \begin{bmatrix} x_t \\ y_t \\ z_t \end{bmatrix} \quad (2.2)$$

$\boldsymbol{T}_B^A$ referred to {A} which represents the initial frame and {B} which represented the change of position vector after rotations and translations were applied to frame {A}. The subscript t referred the point in space. Similarly, when $\boldsymbol{T}_B^A$ is a zero vector, the robot was at its original position. These vectors were described by the Flinders Hexapod end effector which lies on the centre of the top platform where the encoders and actuators connect (Figure 2.1).

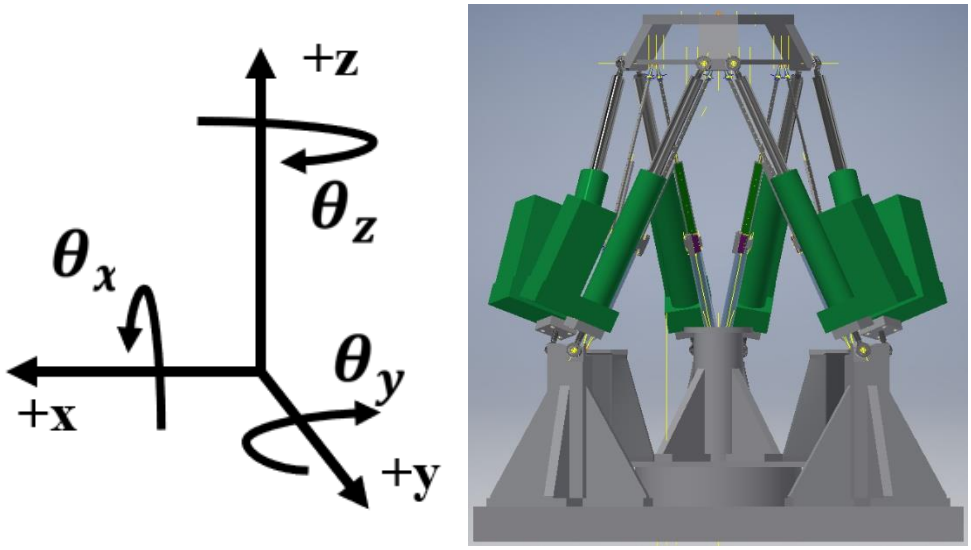

Figure 2.1. Coordinate system axes for Flinders Hexapod.

A general coordinate system was be defined and followed to understand three-dimensional motion as well as performed translations and rotations. The Flinders Hexapods coordinate system included positive z axes is in the upward direction, x positive to the left side and y positive toward the front (Figure 2.1). Translation occurred via the robot pose, $\mathbf{P}_B^A$. The first 3x1 translation matrix was extracted and essentially added to the next coordinate frame. However, rotation was more complex. It involved a 3 by 3 matrix that rotated the frame about a specified axis and therefore the frame shifted position about all three axes. Rotations around x, y and z were represented via the Euler rotation matrix with the 321 sequence indicating rotations occur about the three distinct axes, the equations (2.3) are shown below:

$$\boldsymbol{R}_x(\theta_x) = \begin{bmatrix} 1 & 0 & 0 \\ 0 & \cos(\theta_x) & -\sin(\theta_x) \\ 0 & \sin(\theta_x) & \cos(\theta_x) \end{bmatrix}$$

$$\boldsymbol{R}_y(\theta_y) = \begin{bmatrix} \cos(\theta_y) & 0 & -\sin(\theta_y) \\ 0 & 1 & 0 \\ \sin(\theta_y) & 0 & \cos(\theta_y) \end{bmatrix}$$

$$\boldsymbol{R}_z(\theta_z) = \begin{bmatrix} \cos(\theta_z) & \sin(\theta_z) & 0 \\ -\sin(\theta_z) & \cos(\theta_z) & 0 \\ 0 & 0 & 1 \end{bmatrix}$$

These theories of translation and rotation were applied to the six encoders and actuators that make up the Flinders Hexapod. The top platform and its respective encoders and actuators represented the mobile parts undergoing motion defined via the equations above. Observing the original geometry, it was seen that the encoders make up the space which enclosed the

smallest inner space of the hexapod (Figure 2.1 & Figure 2.2). Therefore, to understand the geometric constraints, only the encoder geometry is required. This was called the inner space of the hexapod.

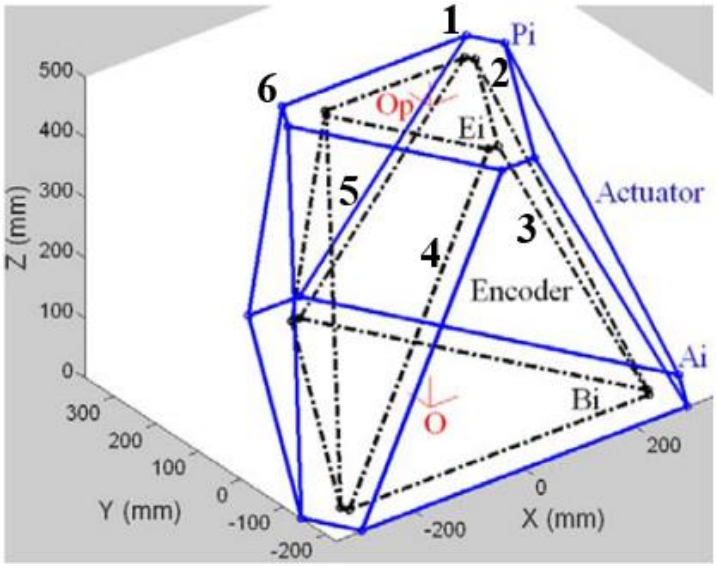

Figure 2.2: Representation of the kinematic model (Ding 2014).

The encoder geometry for a specified pose was derived via inverse kinematics. The encoder legs are defined via the coordinate system, {O}, which represented the base of the encoder endpoints while {Op} denoted the top mobile platform where the centre represented the end effector with end points being the encoder top points. The leg numbers were E_i and B_i which represented the top and bottom of the ith encoder, respectively (Figure 2.2). Since these values were known, the encoder was determined via the vector

$$\boldsymbol{VE0_i} = \boldsymbol{R}(\boldsymbol{E_i}) + \boldsymbol{TR} - \boldsymbol{B_i} \quad (2.4)$$

$\boldsymbol{VE0_i}$ represent the encoder vectors determined by multiplying **R**, the rotation matrix, $\boldsymbol{R}_z(\theta_z)\boldsymbol{R}_y(\theta_y)\boldsymbol{R}_x(\theta_x)$, by the top encoder point, $\boldsymbol{E_i}$, then simply adding the matrix denoting translation, **TR**. This provided the change in translation and rotation of the top encoder point. Finally, the base point, $\boldsymbol{B_i}$, was subtracted from the new top encoder point to produce the encoder vector.

2.2.2 Three-Dimensional Vector Geometry

The cradle introduced further geometric relationships and another degree of freedom that was defined. This degree of freedom interacted with the kinematics defined above. To understand

the relationship between the cradle and the inner space, some simple three-dimensional geometry were revised.

Several relationships needed to be reviewed to add another degree of freedom in the form of the cradle. Parametric equations were useful to relate vectors and points in space. This was because each axes, x, y and z, are a function of one parameter usually termed, t. A parametric equation of a line can be represented via the equations (2.5) below:

$$\boldsymbol{R_{ix}} = \boldsymbol{B_{ix}} + t\,\boldsymbol{VE0_{ix}}$$
$$\boldsymbol{R_{iy}} = \boldsymbol{B_{iy}} + t\,\boldsymbol{VE0_{iy}}$$
$$\boldsymbol{R_{iz}} = \boldsymbol{B_{iz}} + t\,\boldsymbol{VE0_{iz}}$$

To understand the relationship these parametric equations were explained in terms of the encoder vectors. $\boldsymbol{B_i}$ denoted the base point and $\boldsymbol{VE0_i}$ determined the direction of the vector and t represented that point in space. Therefore the $\boldsymbol{R_i}$ value represented the coordinate point for the given axis. The t value represented the distance at that point throughout the vector line. Therefore, the parametric equations of a vector line were determined and correlated to a specific point, $\boldsymbol{R_i}$, by substituting this number into the vector and determining t. From this, the other two coordinates were determined by substituting t into the leftover equations. When t= 0, the vector was represented at the encoder base and as t increased, the position of $\boldsymbol{R_{ix}}$, $\boldsymbol{R_{iy}}$, & $\boldsymbol{R_{iz}}$ was determined for any point in the vector line.

Another important concept that helped to determined relationships was a simple unit vector. Unit vectors provided the direction of a vector with length 1. This was useful for defining geometry when new lines were formed based on an old direction vector.

$$\boldsymbol{U} = \frac{\boldsymbol{VE0_i}}{\left|\left|\boldsymbol{VE0_i}\right|\right|} \qquad (2.6)$$

$\boldsymbol{VE0_i}$ represents the 3x1 matrix denoting the direction vector of a line and $\left|\left|\boldsymbol{VE0_i}\right|\right|$ provided the magnitude of the vector where $\left|\left|\boldsymbol{VE0_i}\right|\right| = \sqrt{x_{VEOix}^2 + y_{VEOiy}^2 + z_{VE0iz}^2}$. Another key but very simple equation needed is the distance between two points:

$$d = \sqrt{(x_2 - x_1)^2 + (y_2 - y_1)^2 + (z_2 - z_1)^2}$$

2.3 Fundamental Cradle Dimensions

Before computing the relationship between the cradle and hexapod, fundamental cradle geometries was obtained. The word fundamental in this context referred to the absolute critical requirements necessary to design the specific components of the cradle. The compact space between the hexapod encoders and the cradle was hypothesised to be extremely close. Therefore, the bare minimum geometry of the cradle parts was useful to know so that maximum space was utilised. It was also useful to use this as a baseline when building and analysing further iterations of this design. At this stage the thickness for all parts was 10 mm. This was analysed later.

The cradle component rotates back and forth simulating flexion and extension in joints. Cradle base dimensions was analysed first. The specimen was typically potted inside the specimen potting cup (Figure 2.3). The diameter of the cup was 91 mm, with a base depth of 13.5 mm. This cup was fixed from the cradle to the using countersunk M6 screws at 70 mm PCD due to threaded holes at the base of the cup. Therefore, the width of the base and length was greater than 91 mm. Width was justified at 100 mm since there were no other functionality constraints. However, the length of the cradle also required consideration of specimen width. An average intact knee joint has a width (medial - lateral) of 100mm - 114 mm however an extra-large size was noted to be 131 mm (Leatt 2018). Furthermore, obese people may be even greater than this. However, this width may decrease for specimens requiring skin and fat removal. Therefore, the distance chosen was between 115-120 mm as this was the minimum distance allowed for an upper average specimen. Keeping in mind it was ideal to increase this length, if possible. Finally, and very importantly, the height of the cradle to the pivot point was based on the centre of rotation (COR). Knee and hip specimen heights seen in literature testing protocols noted that the femur and tibia were truncated 100 - 150 mm (Goldsmith et al. 2015; Wijdicks et al. 2013; Philippon et al. 2017). Therefore, the minimum height required was 160 mm accounting for 13.5 mm depth of the cup and 146.5mm for specimen base to COR (Figure 2.3).

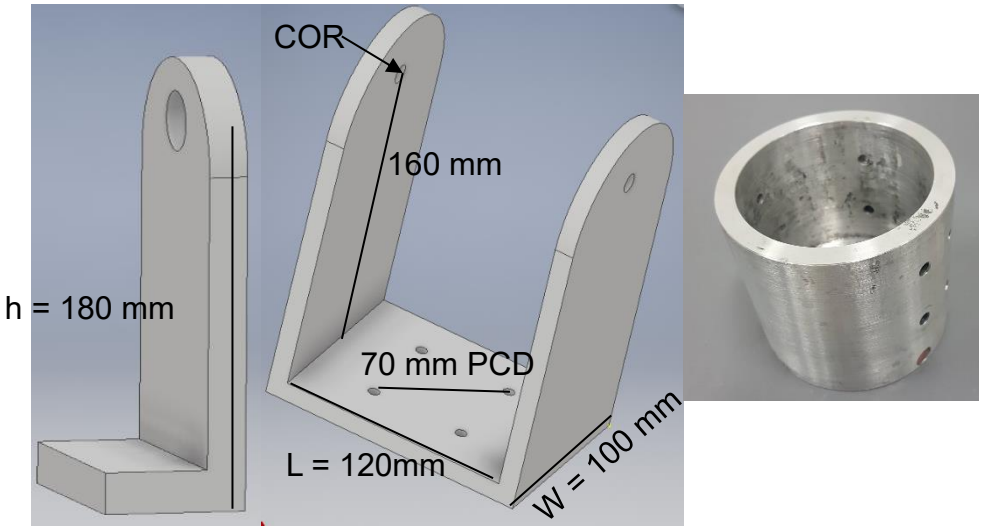

Figure 2.3: Fundamental stand (left), cradle geometry (center), specimen fixation cup (right).

The stand and base component had simple requirements. The stand accounted for the cradle height with clearance for the cradle swing and a section to mount to the base plate (Figure 2.3). Ten millimetres was allowed for the initial clearance when the cradle edge was parallel to the base. Therefore 180 mm was made up of the COR to cradle bottom, thickness of cradle bottom and clearance for the cradle to swing. The base plate length was accounted by the stand, cradle and a clearance between cradle and stand. The base plate was fixed onto the specimen pillar (Figure 2.4). The M10 screw holes are 120 mm PCD which meant that the base plate width needed to be larger than 100 mm, which is the cradle width. To account for this, the width of the base plate was 130 mm.

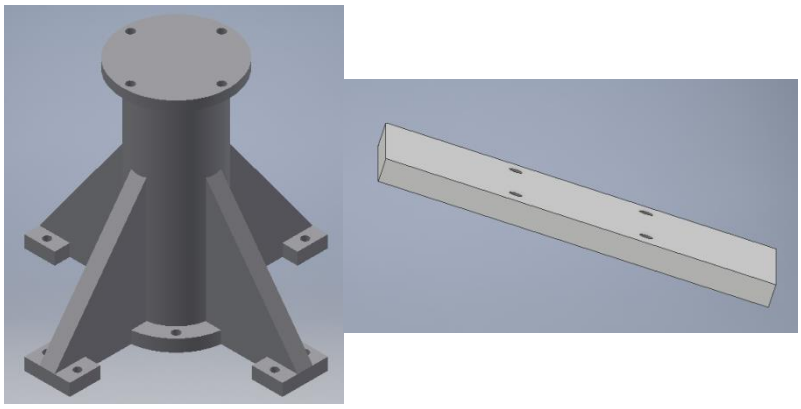
Figure 2.4. Specimen pillar and base plate.

2.4 Computation of Geometric Constraints of the Hexapod and Cradle Assembly

2.4.1 Methods

MATLAB (R2015a, The Mathworks Inc., Natick, MA, USA) was used to computationally calculate kinematics and analyse the geographical representation of the cradle assembly. The code was designed to account for static and dynamic movements of the Hexapod and cradle assembly. Specifically, identifying a Hexapod and cradle robot pose, calculating its geometry and identifying the distance between closest cradle and encoder. Additionally, cyclic motion with the hexapod and cradle were generally represented by the type of motion created during testing. Kinematic data for the cradle was also inputted. A small portion of the code developed for the hexapod encoder kinematics will be extracted from Ding (2014). Table 2.1 listed a list of terms used during this section.

Table 2.1. Revising nomenclature for Hexapod and Cradle assembly kinematics.

Term	Mathematical Representation
Robot pose	$\mathbf{P}_B^A = \begin{bmatrix} x \\ y \\ z \\ \theta_x \\ \theta_y \\ \theta_z \end{bmatrix}$
Position vector	$\boldsymbol{T}_B^A = \begin{bmatrix} x_t \\ y_t \\ z_t \end{bmatrix}$
Encoder base point	$\boldsymbol{B_i}$
Encoder top point	$\boldsymbol{E_i}$
Rotation matrix	$\boldsymbol{R}_x(\theta_x) = \begin{bmatrix} 1 & 0 & 0 \\ 0 & \cos(\theta_x) & -\sin(\theta_x) \\ 0 & \sin(\theta_x) & \cos(\theta_x) \end{bmatrix}$ $\boldsymbol{R}_y(\theta_y) = \begin{bmatrix} \cos(\theta_y) & 0 & \sin(\theta_y) \\ 0 & 1 & 0 \\ -\sin(\theta_y) & 0 & \cos(\theta_y) \end{bmatrix}$ $\boldsymbol{R}_z(\theta_z) = \begin{bmatrix} \cos(\theta_z) & -\sin(\theta_z) & 0 \\ \sin(\theta_z) & \cos(\theta_z) & 0 \\ 0 & 0 & 1 \end{bmatrix}$
Translation matrix	$\boldsymbol{TR} = \begin{bmatrix} x_{TR} \\ y_{TR} \\ z_{TR} \end{bmatrix}$
Encoder Vector	$\boldsymbol{VE0_i = R(E_i) + TR - B_i}$

The inputs into the code include the robot pose $\mathbf{P}_B^A$ and a cradle flexion angle $\{FA\}$ as a single input, sine wave or data file. A coordinate system was defined and demonstrated in Figure 2.5. The origin, $\{\mathbf{O}\}$ is defined in the centre of the encoder base points. The rest of the notation of the coordinate system was denoted in Figure 2.5. It included the $\{BOS\}$, base of stand, $\{COR\}$, middle centre of rotation, $\{CB\}$, centre of cradle base, $\{E_i\}$ and $\{B_i\}$. The geometry for the encoders and cradle were also given in the code. The cradle geometry included the width and length of the cradle base and stand, $\{CB_w\}$, $\{CB_l\}$, $\{BOS_w\}$ & $\{BOS_l\}$, the length of $\{BOS\}$ to $\{COR\}$ and $\{COR\}$ to $\{CB\}$. The encoder geometry was also crucial

to define because it affected the distance from the cradle to encoder. The encoder was made up of the base mount (BM), reader (R), glass scale (GS), and miniature rail (MR) where each had a slightly different physical geometry (Figure 2.6). The thickness and length of each part was measured in Inventor and physically. There were slight discrepancies in comparison of the two. Physical measurements were favoured over CAD models.

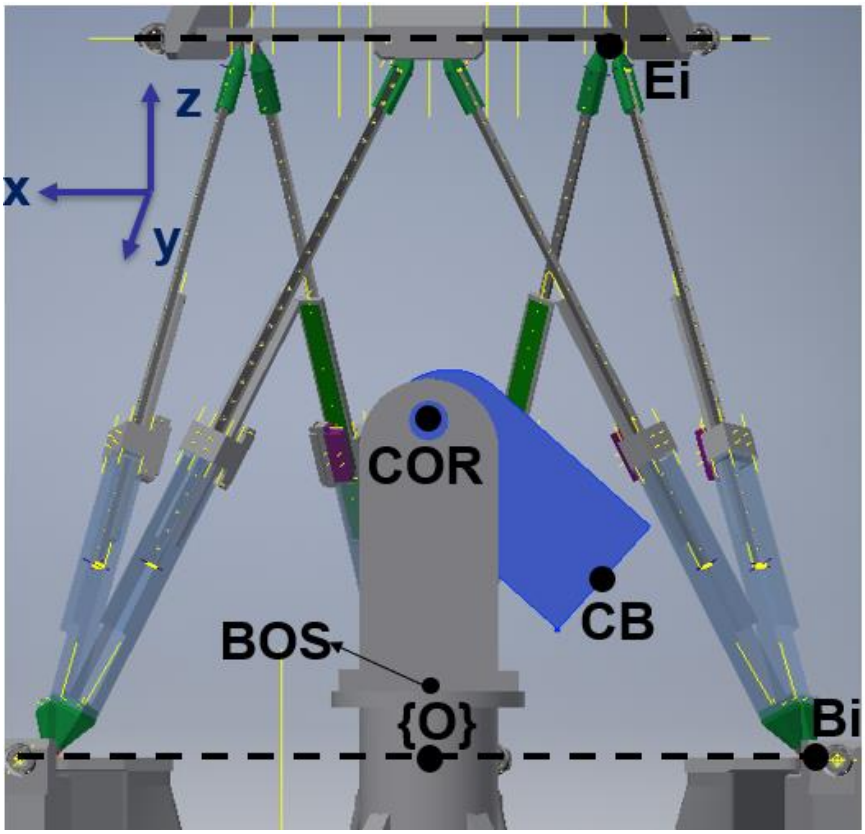

Figure 2.5. Cradle and Hexapod assembly coordinate system. $\{BOS\}$, base of stand, $\{COR\}$, middle centre of rotation, $\{CB\}$, centre of cradle base, $\{E_i\}$ and $\{B_i\}$.

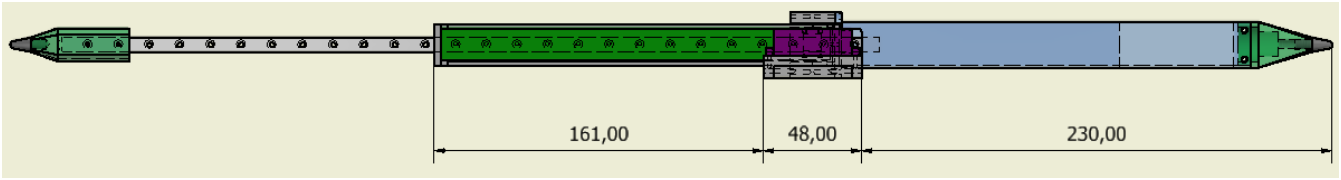

Figure 2.6. Encoder leg geometry. Base mount (BM) is 230 mm, reader (R) is 48 mm, glass scale (GS) was 161 mm and the miniature rail (MR) was the silver structure on the left side.

Since all the geometry was defined, kinematics for a specific frame was found. As discussed in the background, the encoders were plotted in a 3D figure via the equation, $\boldsymbol{VE0_i = R(E_i) + TR - B_i}$. The encoders were also defined at 582 mm which was the approximate

mid stroke of the hexapod actuator and encoders. This was crucial since full functioning motions in the Rx, Ry and Rz directions of the Hexapod is necessary. The physical encoder geometries were taken into consideration by defining its perpendicular distance, then the encoder vector was moved to line to a point on the perpendicular line. This perpendicular line was found by rotating the encoder vector by 90° around the y axis. This defined the perpendicular vectors, $perpen_{EV}$ where EV stands for encoder vector. The encoder and perpendicular unit vectors, $unit_{EV}$ and $Upara_{VE}$ respectively was also be defined via equation $\boldsymbol{U} = \frac{\boldsymbol{VE0_i}}{||\boldsymbol{VE0_i}||}$ (2.6). Therefore $E0 + t\ (Upara_{VE})$ determined the parallel line, $paraVE_{BM}$, to the encoder vector that established the encoders physical inner space position. t represented the thickness of the encoder divided by two as the encoder vectors were defined in the centre of the physical encoder. From this value, a parametric equation was obtained for the shape of the encoder which was parallel to the encoder vector.

$$para\boldsymbol{VE_{BM}} = para_{\boldsymbol{O}} + unit_{\boldsymbol{EV}}\, t$$

t is defined by the length of the physical part of the encoder. These orientations and positions were then plotted onto a figure.

Next the cradle geometry was defined. This was performed via simple geometry of a square and trigonometry to obtain the cradle base at each FA. This was performed by defining the end points of the base and stand by using the width and height given earlier. COR to CB and its end points were determined via applying trigonometric rules for the given FA. Therefore, all cradle key points are determined.

Subsequently, the interaction between CB and the closest encoder leg was determined. CB was the closest encoder, leg two, on the furthest right side (Figure 2.5). Selecting this encoder, parametric equations was used to determine the encoder position closest to the cradle base. The known values were the cradle base end points and the encoder points at each physical part of the encoder. These were important to note. First the cradle base side that was the highest will be selected and the z value will be obtained. If the z value was greater than the reader height, then the base mount, reader and glass scale will need to be considered. A distance from each part of the encoder was obtained via identifying t given the cradle z value. This t value was substituted into the parametric equation for part of the encoder vector geometry. Finally, the distance between the cradle base and the encoder leg was determined by subtracting the x coordinates of the respective components.

The kinematics and interactions between the cradle and hexapod assembly were calculated for each frame. A general overview was shown, and the MATLAB code is found in Appendix A (Figure 2.7). This information was processed into figures and tables as well as dynamically simulated with in clips that show the key interactions.

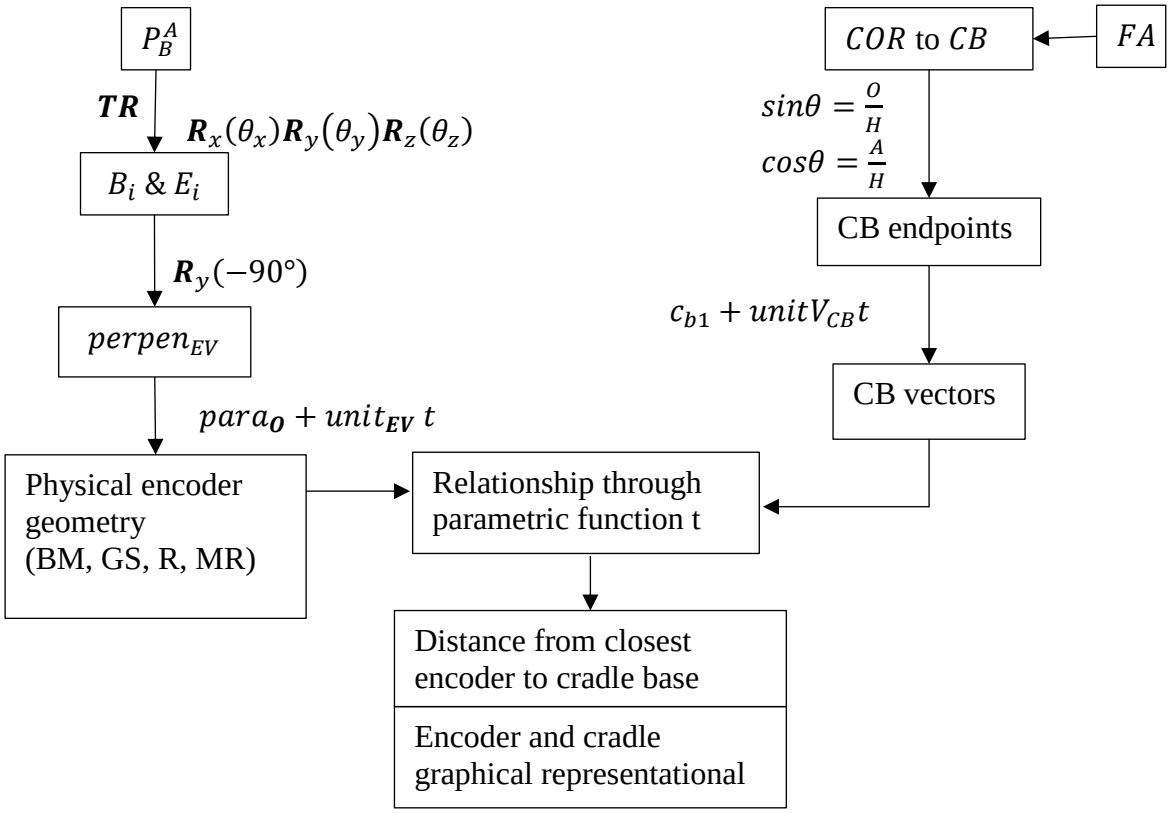

Figure 2.7. Vector geometries were used to define encoder vectors on the left side while cradle points in 3D space were calculated on the right side. Parametric relationships were used to relate the encoder vectors to the cradle geometry. These results produced distances from the closest encoder to cradle and a geographical representation of the encoder and cradle assembly.

2.4.2 Results

Graphical representations via MATLAB code for different robot poses and cradle flexion angles were found (Figure 2.8). The encoder geometry was shown and a difference in each part of the encoder can be seen. A distance was determined for the nearest encoder leg to the cradle base. These scenarios display encoder leg two as the closest leg. Computation methods of the MATLAB code provided the distance produced for its given pose. The distance for 0° and 90° flexion was 199.75 mm and 22.62 mm respectively. These are labelled on Figure 2.8.

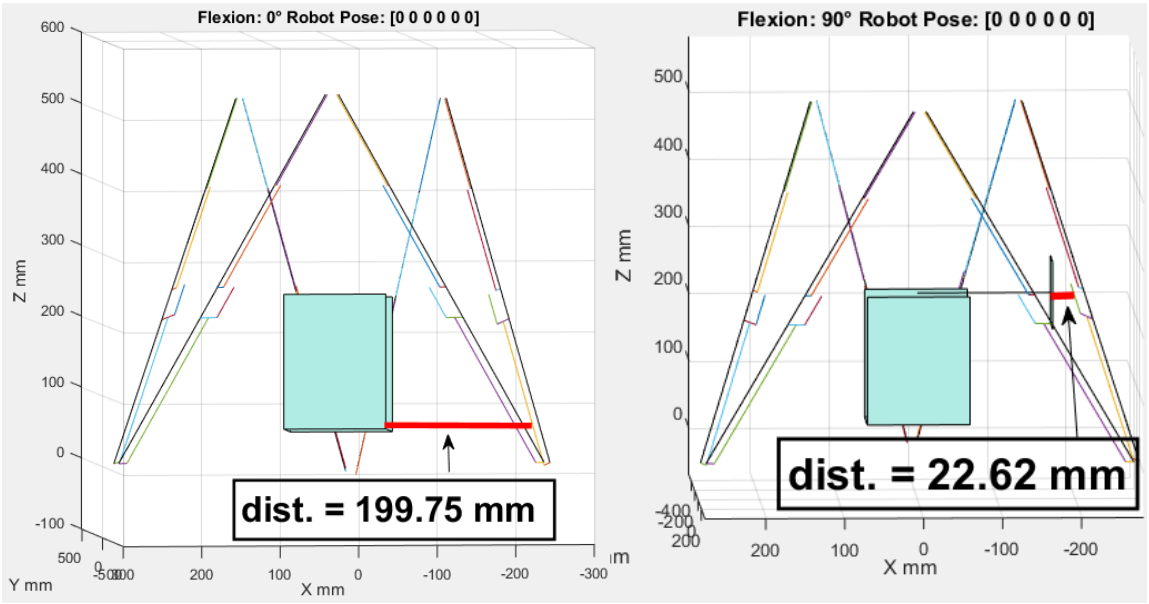

Figure 2.8. Neutral robot pose with cradle flexion at 0° (left) and 90° (right).

Dynamic simulations were also performed to simulate the kinematics of each hexapod and cradle assembly frame. A graphical representation was produced as well as a table of values that indicate the distance between the cradle and hexapod at its given robot pose and flexion angle. For motion demonstration purposes, a cyclic motion of ±10° around the x axis and a flexion angle simulating data of knee kinematics was simulated. An extraction of the last 20 frames were listed in Table 2.2 and a corresponding graph for all distances found during this simulation was shown in Figure 2.9. The highest value seen for cradle flexion was 58.66º with a corresponding distance of -9.3847 º rotation around the x axis. This produced a distance between the encoder and cradle of 49.477 mm.

Table 2.2. last 20 frames of Hexapod ±10° interacting with kinematic data for knee flexion and their corresponding closest distances

Rx (º)	**Flexion Angle (º)**	**Closest distance from encoder to cradle (mm)**
-5.45	38.53	90.58
-6.48	44.92	75.66
-7.40	50.54	63.90
-8.20	54.90	55.75
-8.86	57.63	51.12
-9.38	58.66	49.47
-9.74	58.19	50.25
-9.95	56.51	53.06
-9.99	53.80	57.85
-9.87	50.13	64.86
-9.58	45.57	74.38
-9.14	40.25	86.57
-8.55	34.40	101.18
-7.81	28.37	117.38
-6.95	22.6	133.66
-5.98	17.81	148.09
-4.90	14.24	158.97
-3.75	12.11	165.52
-2.53	11.32	167.94
-1.278	11.62	166.95

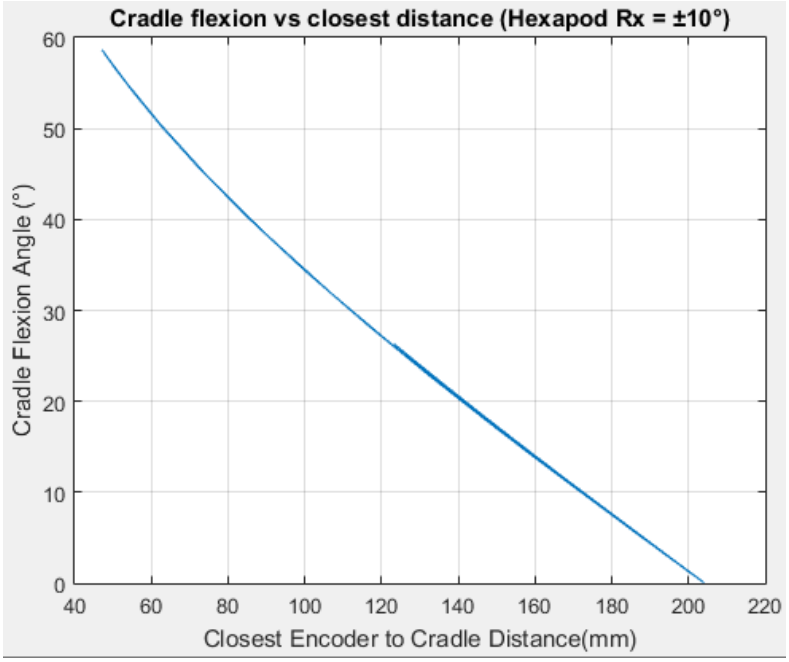

Figure 2.9. Demonstrates closest distance values for cradle flexion angles during a dynamic simulation of kinematic knee motion of cradle with cyclic motion of Hexapod undertaking Internal/External $R_x = \pm 15°$.

The cradle end range of motion was generally at 90°, therefore this angle was observed with hexapods robot poses, 5° away from its end ranges of motion. These included $R_x = \pm 20°$, $R_y = \pm 20°$,$R_z = \pm 15°$. Their corresponding closest distance was also determined and demonstrated in Figure 2.10, Figure 2.11 & Figure 2.12, respectively.

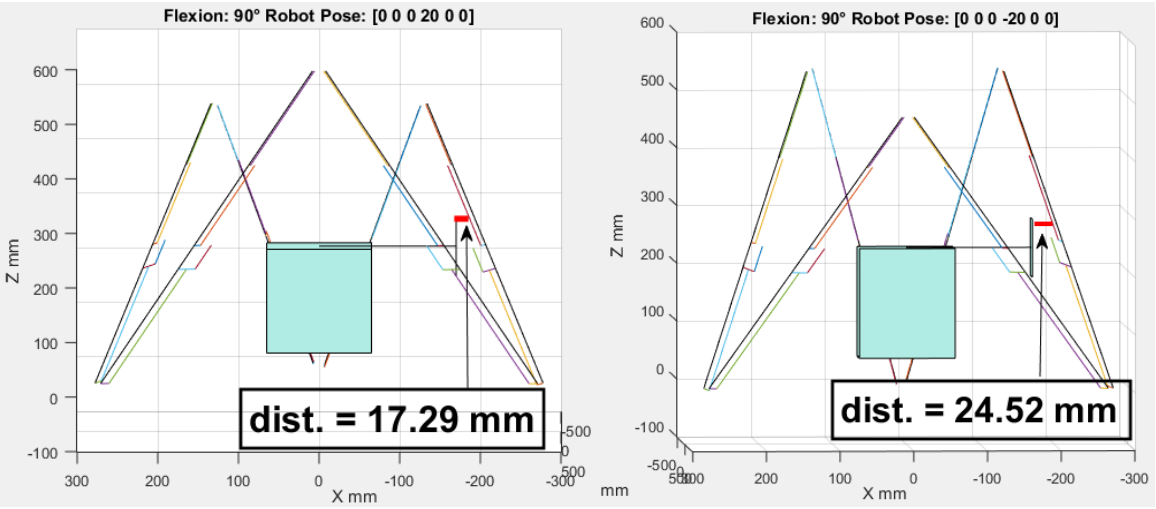

Figure 2.10. Demonstrates cradle flexion of 90º at $R_x = 20°$ (left) and $R_x = -20°$ (right).

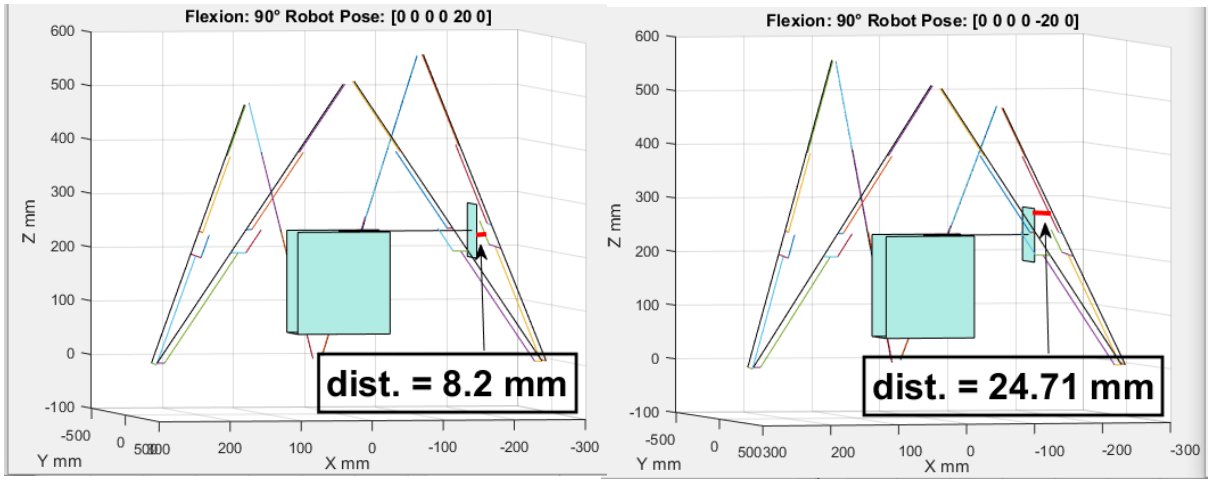

Figure 2.11. Demonstrates cradle flexion of 90º at $R_y = 20°$ (left) and $R_y = -20°$ (right).

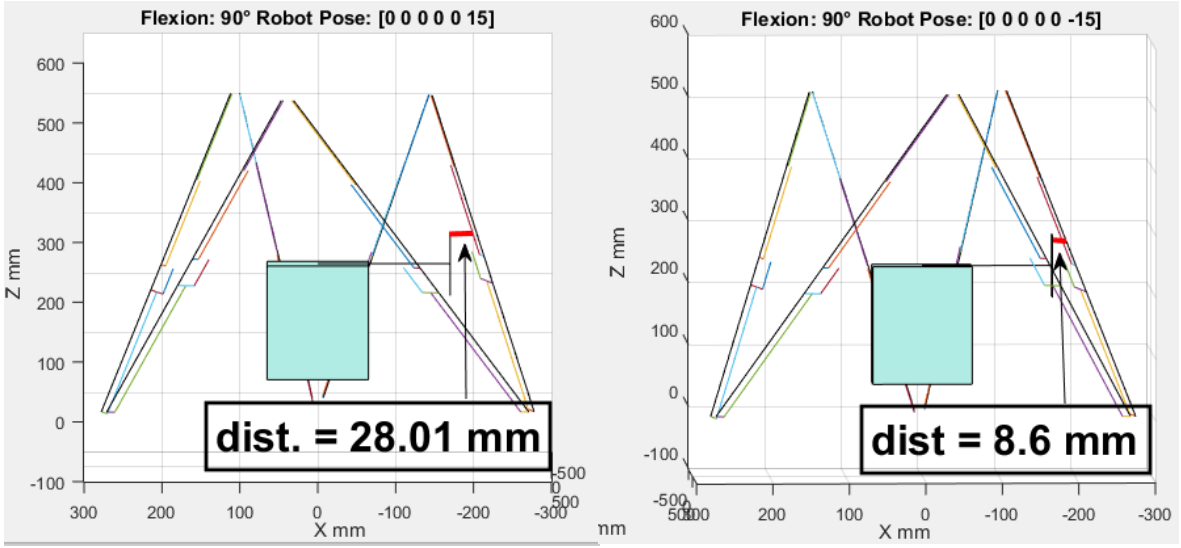

Figure 2.12. Demonstrates cradle flexion of 90º at $R_z = 15°$ (left) and $R_z = -15°$ (right).

2.5 Validation and Design of Hexapod and Cradle Assembly

2.5.1 Methods

This section involved three separate methodologies which were broken down into three sub-headings. First, the design of the proof of concept was found in Section 2.5.1.1 followed by the control system of the prototype in Section 2.5.1.2 and finally the assembly of the Cradle and Hexapod in Section 2.5.1.3.

2.5.1.1 Prototype Design

The prototype design was used to validate work performed in Section 2.4. The use of the prototype was to observe the geometry of the cradle interacting with the Hexapod. This meant that the design was capable of position control allowing the cradle to rotate to a flexion angle and hold as well as fulfilling the fundamental cradle geometry discussed in Section 2.3. Since the only force exerted on the cradle prototype was a plastic knee specimen, the fixation cup as well as any force from the hexapod when fixing the cradle into the system, the material used was acrylic. Each component was designed to be laser cut from 10 mm thick acrylic and glued together via Acrylic Adhesive SCIGRIP Weld-On 3, which was a water thin solvent that acts to weld the acrylic together. To fulfil position control requirements a Pololu 131:1 Metal Gearmotor 37Dx73L mm with 64 CPR Encoder was used to design the cradles pivot point on one side. The other side was designed to include a bearing and allow for smooth actuation. The cradle motor rotational point was designed around the Pololu motor (Figure 2.13).

Countersunk screws were used to secure the motor to the stand and a clearance hole of 13 mm to allow for rotation. The D shaft itself was only 6 mm with a length of 22mm. The shaft was attached to an adapter which was press fitted into the cradle. It was secured further via a grub screw through the cradle and adapter to the shaft. The end of the adapter had a hex shape on the end. Therefore, this was used to ensure the success of the pivot point by creating an acetal hex flange (Figure 2.13) which was fixed to the inside surface of the cradle. The other rotational point contained a bearing press fitted and grub screwed into the stand. A 10

mm shoulder bolt was inserted into the bearing allowing the shoulder bolt to rotate the cradle. The cradle component was cut into three parts and glued together. Similarly, the stand and base were glued together. These drawings can be found in Appendix C.

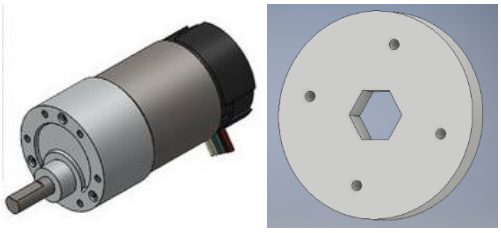

Figure 2.13. Pololu motor (left) and hex flange (right).

2.5.1.2 Control System

Since the program of the final cradle will be controlled through LabVIEW, this prototype system will follow suit. The control system was designed to be simplistic and an easy interface (Figure 2.14). The basic requirement was that the user can input an angle flexion into the program and the cradle will move to that angle. Therefore, this program contained three simple modes; input angle, flexion jogging and cyclic motion. LabVIEW generates an Analog output signal from 0 to 5 V that was acquired by the NI9178 Instruments DAQ Chassis and Analog output module. This signal was sent to a position controller called the Sabertooth and SyRen Kangaroo x2 motion controller. It received the Analog signal and ensured the required position due to the self-tuning PID controller which received quadrature encoder feedback. The position controller outputted to the motor drive generated current via a 12 V power supply sending current to the Pololu motor.

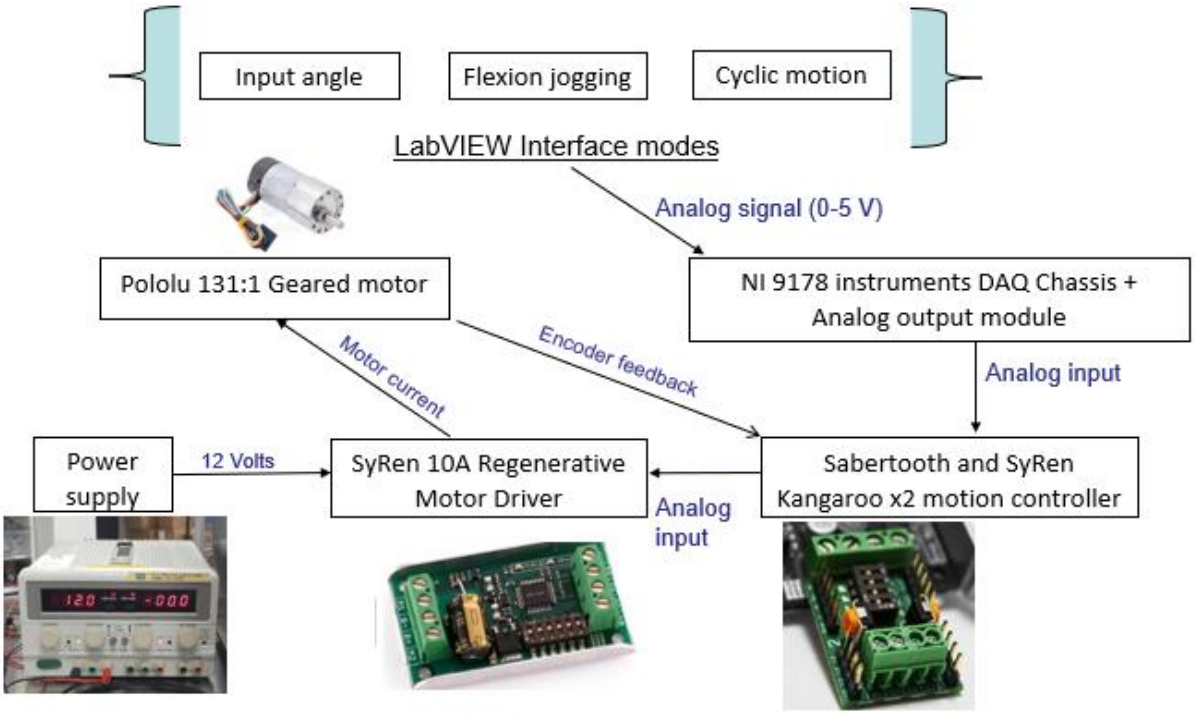

Figure 2.14. Cradle prototype control system.

The main configuration of this set up was the auto tuning of the motion controller. It involves configuring the end ranges of motion by manually guiding the cradle in both directions. This was how the motion controller will understand the motion path. The cradle was rotated 180° in one direction and then 180° in the opposite direction to complete the full 360° of motion. Therefore 0° is defined at 2.5 V, 180° at 5 V and -180° at 0 V. This was programmed into the LabVIEW block diagram allowing the user to see the actual angle. The first mode was very simple as an angle was typed straight into the program. The second mode 'flexion jogging' will allow the user to move a slider and the corresponding angle will be actuated to cradle. The third mode, 'cyclic testing' will input a flexion magnitude and frequency to simulate sinusoidal cyclic motion that is commonly used for biomechanical testing. Small adjustments were made to fulfil each mode. These modes are shown in Figure 2.15. Figure 2.16 demonstrates the signal sent over 20 seconds to the cradle for cyclic motion of 45° and 90° at a frequency of 0.1 Hz and 0.5 Hz. Appendix B provides further information for the block diagrams in LabVIEW.

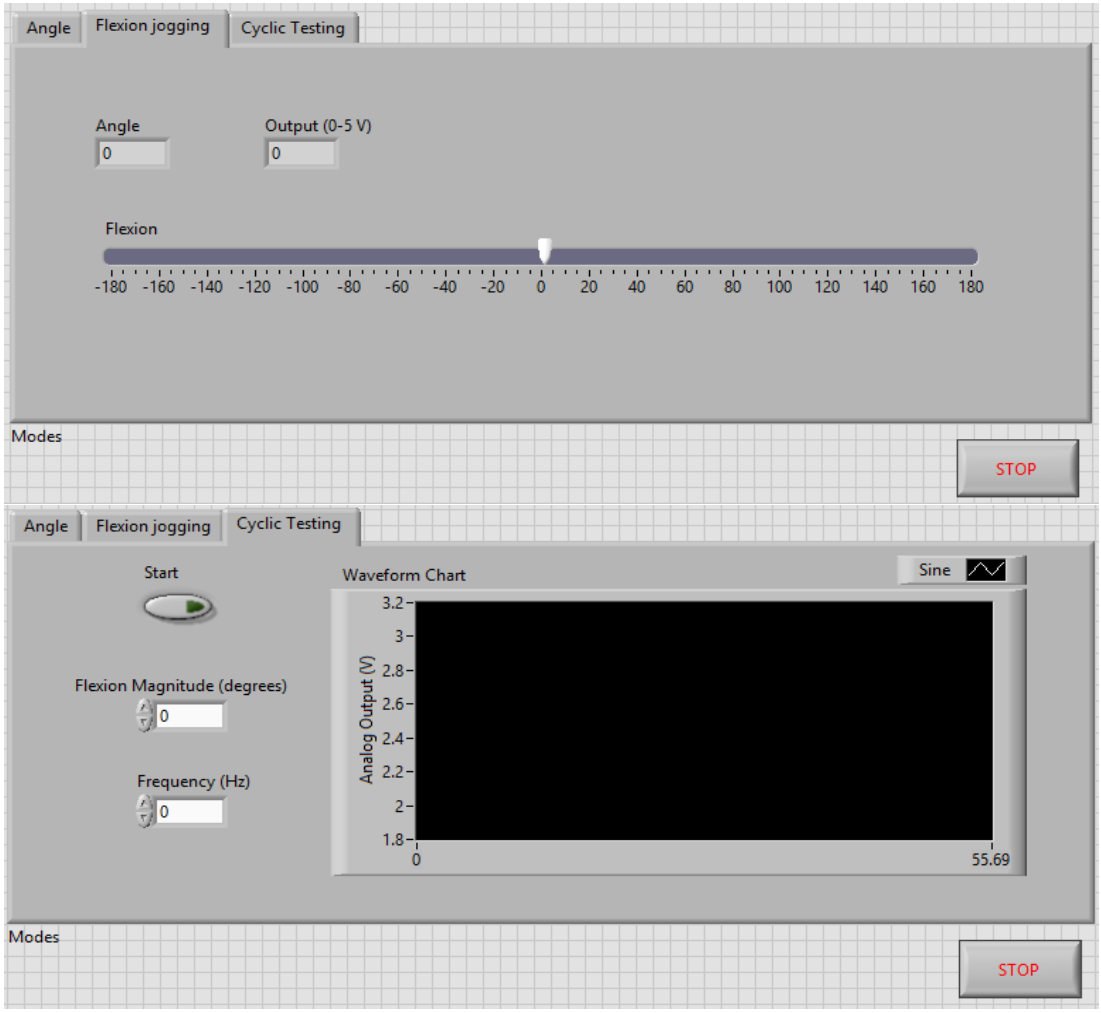

Figure 2.15. LabVIEW interface for flexion jogging (above) and cyclic testing below.

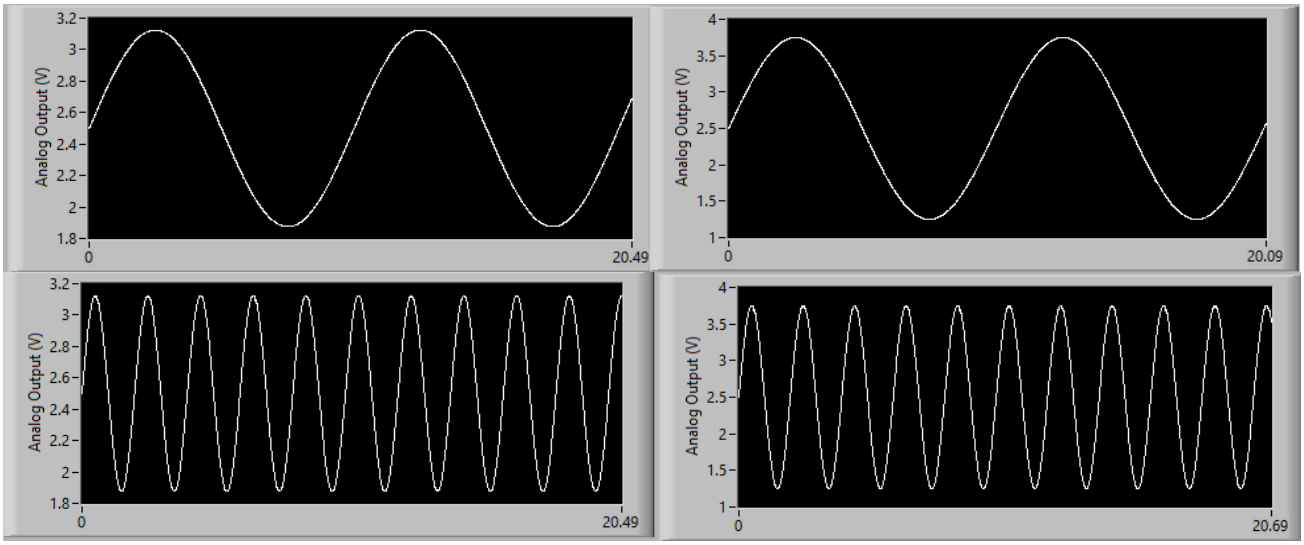

Figure 2.16. Demonstration of cyclic motion sent to cradle device. 45° at 0.1 Hz (top left) and 0.5 Hz (bottom left), 60° at 0.1 Hz (top right) and 0.5 Hz (bottom right).

2.5.1.3 Measurement and Assembly of Cradle and Hexapod Assembly

Physical measurements of results found in Section 2.4.2 were validated. These measurements were taken with a ruler of 1 mm resolution. Before the cradle was fixed into the Hexapod, measurements of the general space in the x and y directions at the centre of rotation will be obtained. The encoder legs began at the mid stroke pose of 582 mm which determined the height required for the specimen and cradle assembly. A measurement of the distance from the specimen pillar to the end effector was also attained.

The cradle was fixed into the hexapod and measurement testing of the closest encoder, leg two, to the cradle base can be determined. Primarily, the hexapod robot will remain in a neutral pose while the distance from the encoder to the cradle base were determined for angles of 15°, 30°, 45°, 60°, 75°, 90° and 120°. Secondly, the end ranges of both the cradle and hexapod assembly were investigated. The end rotational ranges of motion listed for the hexapod were at R_x and R_y at $\pm 25°$ and R_z at $\pm 20°$. To be conservative, these poses were observed for R_x and R_y at $\pm 20°$ and R_z at $\pm 15°$. All six of these hexapod positions were measured with end ranges of cradle flexion at 90° and 120°. Finally, these configurations were compared with the computational results.

Next the configuration of the specimen-cradle-hexapod assembly was investigated. This was based off the mid stroke of the hexapod. The space between the specimen pillar and specimen coupling plate was computationally calculated to be 520 mm with encoder heights of 582 mm. This space was realistically investigated as the physical set up was also crucial to the design. Existing parts and suitable configurations were determined.

2.5.2 Results

2.5.2.1 Cradle Prototype

The cradle prototype was made and that was controlled through LabVIEW (Figure 2.17).

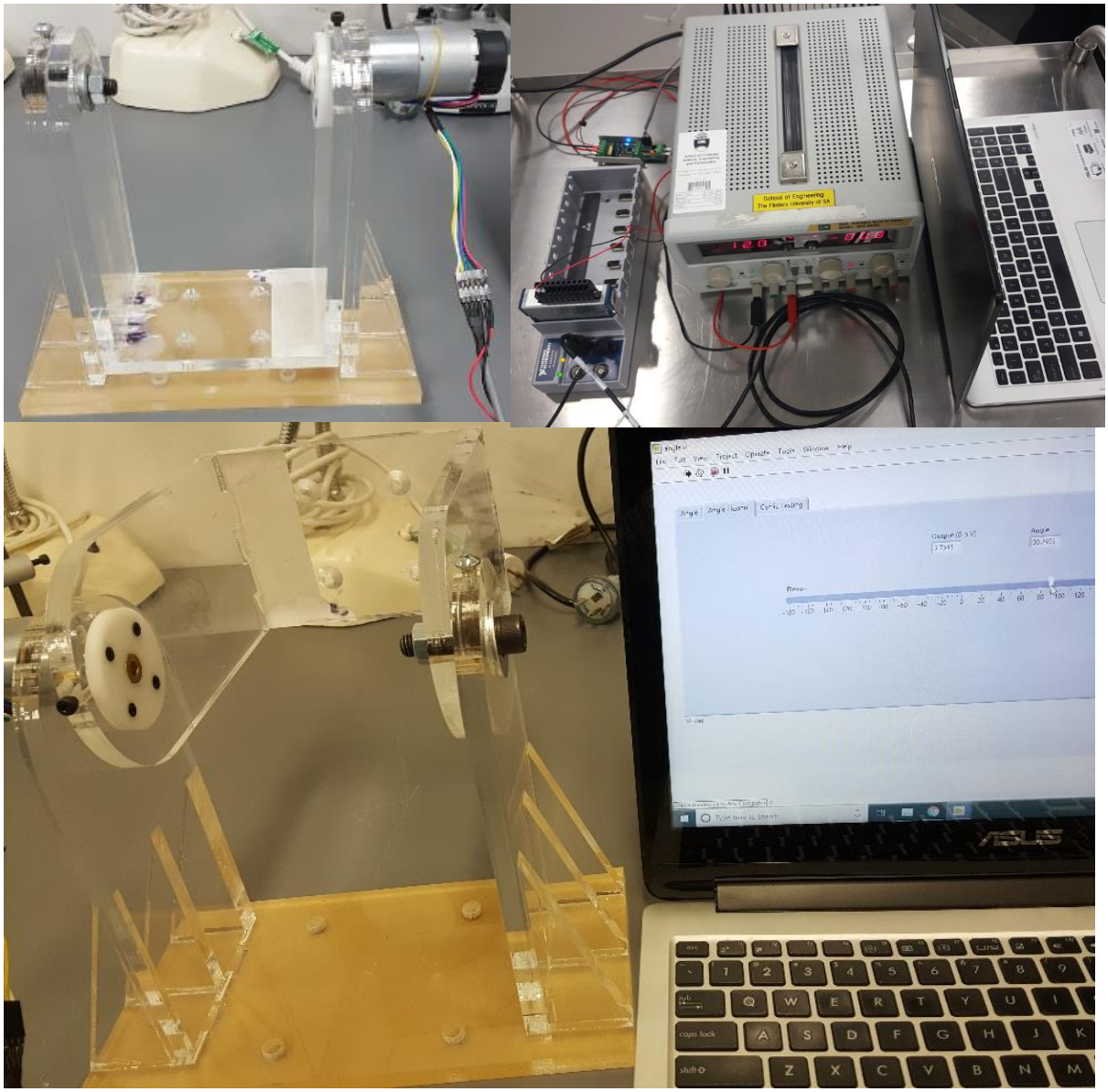

Figure 2.17. Cradle prototype (top) and at 90º run by LabVIEW program (bottom).

2.5.2.2 Comparison of Physical and Computational Geometric Constraints in the Cradle and Hexapod assembly

Measured points of interest were found to check the key dimensions of the hexapod in the x, y and z direction. The z-axis measurement was from the specimen pillar to the specimen coupling plate because the coupling plate was blocking the top plate. The computational measurement was deduced by the encoder coordinate system where z= 0 mm was line with the encoder bottoms and 520 mm was in line with the encoder top. Based off measuring points, 50 mm was taken off for the encoder base plate to the specimen coupling plate and 12 mm for the specimen coupling plate to the end effector. There was a 3 mm difference between the physical and computational calculations (Table 2.3). This could have been due to the encoders being embedded into their magnetic sockets. The x and y axis measurements were taken at 190 mm from the specimen pillar as that was height of the COR of the cradle device. It was demonstrated that the physical measurements in the x and y directions were lower than the computational calculations by approximately 13 mm (Table 2.3).

Table 2.3. Fundamental measurements of the Flinders Hexapod.

Inner space dimensions	**Physical measurement (mm)**	**Computational (mm)**
x direction at z = 190 mm	372	386
y direction at z = 190 mm	330	342
Specimen pillar to specimen coupling plate	455	458

Results comparing physical measurements between cradle and hexapod assembly were obtained. Table 2.4 demonstrated a comparison between physically measured and computational x distance from cradle to encoder at flexion angles between 15º to 120º with 15º increments till 90º and a separate value of 120º. The part of the encoder was also noted as it was important to see the distances came from the same physical component.

Table 2.4. Comparing physical to computational measurements for cradle angles at a neutral robot pose.

Cradle flexion angle (º)	**Distance from closest encoder to cradle (mm)**		**Closest Encoder part**
	Physical measurement	*Computational*	
15º	153	152.27	Base mount
30º	110	108.2	Base mount
45º	70	70.63	Base mount
60º	41	42.03	Base mount
75º	15	17.44	Reader
90º	22	22.62	Reader
120º	23	23.57	Glass scale

Table 2.4 & Table 2.5 demonstrated the comparison between end ranges of motion of the hexapod and the cradle at 90° and 120°, respectively. Each encoder part corresponded computationally and physically. Differences in distances were roughly 1- 3 mm and distances for cradle flexion of 90º and 120º only differed by decimal points. Figure 2.18 demonstrates Rx = $-20°$ for cradle flexions of 90º and 120º.

Table 2.5. Comparison of computational and physical measurements at hexapod end range of motion while cradle flexion angle is at 90°.

Distance from encoder to cradle at 90° (mm)				
Hexapod Robot pose		*Physical measurement*	*Computational*	**Closest Encoder part**
$\boldsymbol{R_x}$	$+20°$	16	17.29	Glass scale
	$-20°$	21	24.51	Reader
$\boldsymbol{R_y}$	$+20°$	6	8.2	Glass scale
	$-20°$	25	24.7	Reader and glass scale
$\boldsymbol{R_z}$	$+15°$	24	26.58	Glass scale
	$-15°$	10	8.61	Glass scale

Table 2.6. Comparison of computational and physical measurements at hexapod end range of motion while cradle flexion angle is at 120°.

Distance from encoder to cradle at 120° (mm)				
Hexapod Robot pose		*Physical measurement*	*Computational*	**Closest Encoder part**
$\boldsymbol{R_x}$	$+20°$	17	17.4	Glass scale
	$-20°$	21	24.8	Reader
$\boldsymbol{R_y}$	$+20°$	9	8.7	Glass scale
	$-20°$	23	23.4	Glass scale
$\boldsymbol{R_z}$	$+15°$	24	26.4	Glass scale
	$-15°$	11	9.3	Glass scale

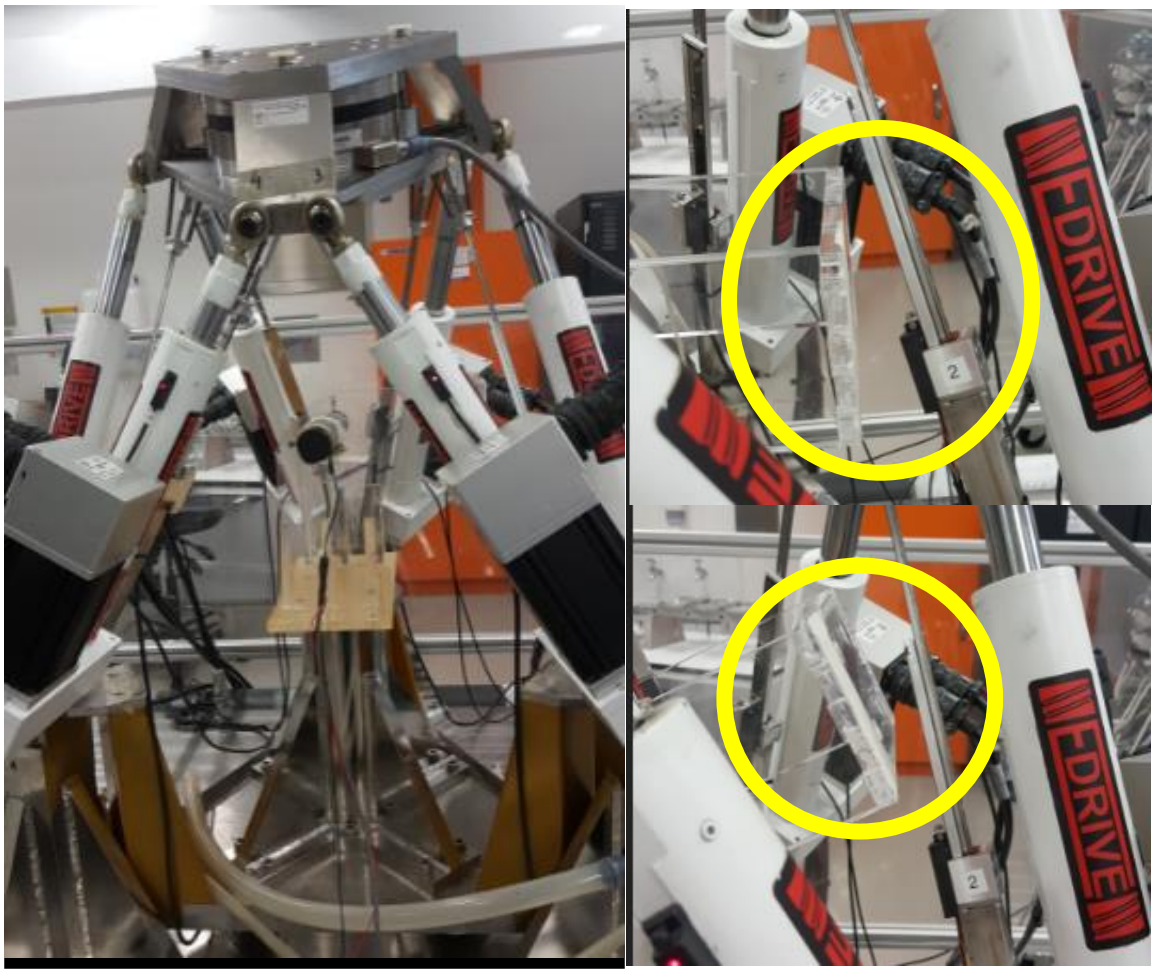

Figure 2.18. The yellow circles indicate the position of the cradle and encoder. Hexapod in $R_x = -20°$ (left) with cradle at 90° (right top) and 120° (right bottom) at a physical distance of 21 mm.

Using this information and relating it to flexion and extension of a joint, the cradle was rotated around the R_y direction and therefore maximum flexion can be seen when the hexapod is flexing toward the cradle in the R_y direction creating a kneeling or squatting motion. Figure 2.19 demonstrated this action with the cradle and hexapod assembly. The physical model validated the geometric computation of 23.4 mm with a measurement of 23 mm. Therefore, the validation of the cradle reaching above 140º range of motion was confirmed. Observing the space, the cradle could be increased even further if required.

Figure 2.19. The yellow circle indicates the position of the cradle and encoder. Hexapod at rotation, $R_y = 20°$ with a cradle flexion of $120°$ and a physical distance between cradle and hexapod of 23 mm.

2.5.2.3 Physical assembly

The physical assembly of the cradle and Hexapod was collated from knowledge of the specimen coupling plate to the specimen pillar. Table 2.3 listed these values as 455 mm physical and 458 mm computational. The physical measurements were used to base the assembly of the specimen in the cradle and Hexapod. The base of the cradle was designed to insert directly into the specimen pillar. This was because there was more space at the base of the hexapod, however this leaves more room from the centre of rotation to the top of the specimen coupling plate. The cradle was designed for the pivot point to be in line with the centre of rotation of the specimen. Therefore, there was be 190 mm to the specimen pillar consisting of the cradle and fixation cup. This left 265 mm to the specimen coupling plate. Normally specimens were truncated at 150 mm, therefore, including the specimen cup depth of 13.5, leaves 101.5 mm that isn't accounted for. For this situation, an offset spacer was inserted to account for the space. This was an existing spacer in the lab, therefore the specimen needed to be cut down to size. Table 2.7 summarizes the parts used for this particular mock set up.

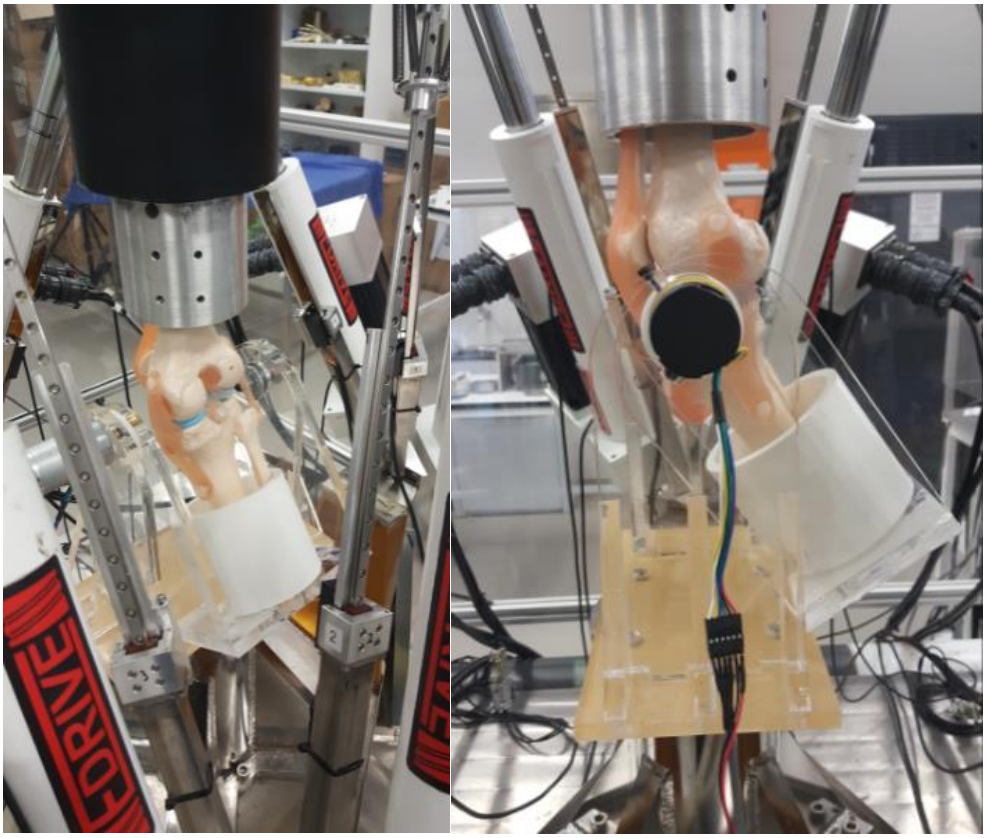

Figure 2.20. Mock specimen set up in cradle and hexapod assembly. Demonstrates the offset black spacer, fixation cups and specimen required (left) and the pivot point and specimen joint center lining up at a cradle flexion of 40°.

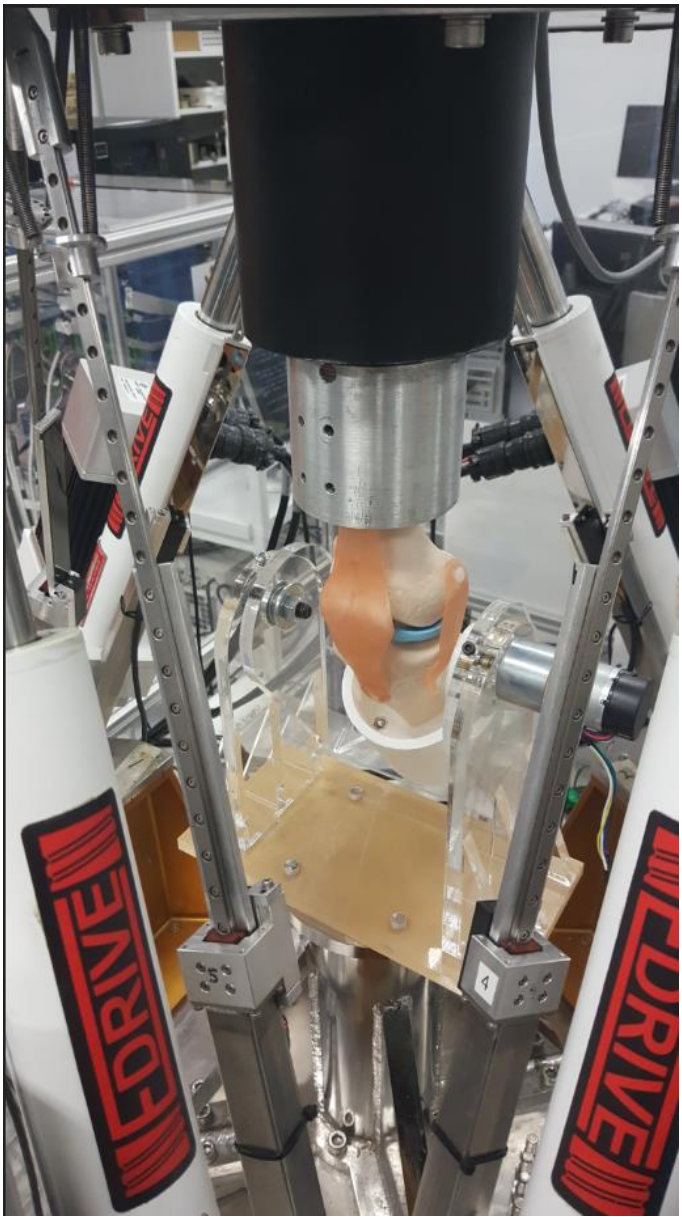

Figure 2.21. Complete set up from specimen coupling plate through to specimen pillar.

Table 2.7. Mock assembly parts and lengths used.

Component	Length (mm)
Spacer	125
Top fixation cup	13.5
Specimen to joint centre	126.5 (only due to spacer)
Joint centre to bottom of cradle	190

2.6 Discussion and Conclusion

Section 2.4.1 outlined the types of graphs and computational results that were possible to obtain from the developed program. The distances shown were the result of the kinematic theory discussed. End cradle dimensions allowed for a physical representation using rectangles. Static poses and corresponding distances showed that the cradle had the ability to flex to 90º and dynamic simulations confirmed it was going to be possible to orientate the hexapod around the cradle in the R_x, R_y and R_z directions. This was demonstrated via the dynamic simulation of kinematic knee data for the cradle flexion and rotation in R_x simulating internal and external rotation. Finally, poses of hexapod end ranges of motion were determined with a cradle pose of 90º. The direction of R_x demonstrated that the cradle could be held at a certain flexion while, for example, additional knee motion could be simulated in the medial to lateral direction. This could be helpful to determine injuries or ligaments and tendons that are elongated during that movement. R_z could represent a twisting like motion of the knee joint. However, the most important is R_y as it rotates in the same direction as the cradle creating more flexion or extension. The results showed that it was theoretically possible to insert the cradle into the hexapod with a successful achievement of 140º flexion and 23.4 mm between the cradles and the encoder. The other direction of R_y found the cradle distance dangerously close to the encoders space with 8.2 mm distance. Luckily, this direction is not important because the cradle has the ability to extend the knee past its neutral position.

Section 2.5.2 of the results compared the difference between the computational and physical environment to question the validity of the computational method. Overall there was a strong association between results. There was a discrepancy when measuring the initial configuration of the hexapod in the x and y direction. For the x direction, the computational calculation was 386 mm and the physical measurement was 372 mm. In the y direction, the distances were 330 mm and 342 mm for the physical and computational calculations respectively. This was mainly due to the very difficult task of measuring the space without touching the encoders or hexapod as well as keeping it at a steady height. This range isn't crucial, but it did show that there was a larger space in the x direction which confirms the validity of the cradle configuration.

There were two key tests performed to inspect the validity of the computational methods and confirm its results. These included a cradle flexion test from 0 to 120º at neutral hexapod pose and secondly inspecting the end ranges of motion poses with the cradle at 90º and 120°. The results show that the computational calculations of the cradle and hexapod assembly provide a close association to the physical relationship within the inner space. The difference between the comparisons are all within 3 mm. Table 2.8 represents the first test with its corresponding percentage change in the comparison between physical measurements and computational. It is demonstrated that there is a large range of percentage change from 0.48% to as high as 15.04% for 75°. The highest percentage change was a 2.44 mm difference which may seem like a large number given the small environment. Percentages were also calculated for the end range of motion robot poses which saw a percentage change as high as 30.98% for Ry flexion with a difference of 2.2 mm. The other stand out percentage changes that were larger than 15% including, -Rx for 90° and 120°, as well as Rz for -90° and 120°.

Table 2.8. Percentage change in physical measurement to computational distance.

Cradle flexion angle (º)	**Distance from closest encoder to cradle (mm)**		**Difference between physical and computational measurement (mm)**	**Percentage change (%)**
	Physical measurement	*Computational*		
15º	153	152.27	0.73	0.47
30º	110	108.20	1.8	1.65
45º	70	70.63	0.63	0.89
60º	41	42.03	1.03	2.48
75º	15	17.44	2.44	15.04
90º	22	22.62	0.62	2.77
120º	23	23.57	0.57	2.44

Discrepancies could be explained by several reasons. There will always be differences in the computational and physical environments. A key physical factor may have been human error due to measurements being obtained from the unaided eye as well as the fact that the encoders cannot be touched or knocked, therefore these measurements were taken at a distance for certain measurements. Also, they were taken to ere on the larger side if a valued seemed to be in between a millimetre. The other major factor was the physical movement of

parts that computation just doesn't account for. The assumption made in the code was that the encoders will be facing inward and parallel to the cradle. Computation provides a perfect vector encoder geometry that is unlikely in the physical environments as the encoders are always adjusted to back to their proper position before testing. Therefore, the assumption they are parallel during the end range motion positions may have provided further discrepancy. Another correlation of this is indicated by the larger difference in the end range of motion tests as opposed to Table 2.8 which demonstrated a smaller percentage change in measurement. This may also provide a reason for the large percentage changes of $-R_x$ and Rz . Further to this, code could be inspected further and account for these geometric changes, however more inspection into the exact motions of the hexapod encoders would need to be heavily analysed and a method to simulate this would be time consuming. Accounting for encoder geometry in the code could also be a source of error due to the width change in four different components. Physically, the encoder movements for positive and negative rotation could be analyse and hopefully the largest encoder changes would be in $-R_x$ and R_z .

Finally, the result from Section 2.5.2.3 demonstrated the physical assembly of the cradle, specimen and hexapod set up. The set up will allow for maximum use within the lower space of the hexapod. However, the problem with the cradle sitting on the bottom pillar is that there will be too much space to the coupling plate. The spacer shown and used was too big however it was used for convenience. The spacer length was 125 mm while the distance calculated for an average specimen was 101.5 mm. This is not a large space which could be accounted for via fixtures or keeping 10 cm more of the specimen. This information can also lead to designing custom fixation devices for different joint such as ankles, hips, shoulders etc. It would mean that parts such as a foot or hemi pelvis would be fixed to the top plate and their respective bones potted in the cradle.

The purpose of the chapter was to determine the geometry of the cradle and its largest flexion motion. Through these calculations and this configuration, the cradle and hexapod can provide at 140º flexion when the cradle is at 120º and R_y at 20º. This validates the requirement for a larger range of motion of the hexapod. The geometry of the cradle dimensions will be clear of any collisions in both the computational and physical results.

Chapter 3 Static Analysis of Cradle Device

3.1 Introduction

A requirement of the cradle device is its ability to undergo static simulation. This involves biomechanical testing performed via the cradle device. Biomechanical testing in static poses are very common for knee testing. Examples may involve locking a knee joint at 90º flexion then loading the joint to failure or performing internal / external rotation on a static knee at various flexions. The cradle must be capable of withstanding those types of tests. Therefore, the highest stiffnesses and loads that are found within the literature will form the specifications required for the cradle.

This chapter aims to investigate the repercussions of static simulation on the cradle device by identifying the required specifications and redesigning the device as required. Consequently, Section 3.2 investigates the theories, specifications and information necessary to design and analyse the device. Following this, Section 3.3 states methods using Autodesk Inventor and Finite Element Analysis (FEA) to design and analyse the cradle during static simulation and results are presented in Section 3.4. Finally, Section 3.5 will discuss and conclude this chapter.

3.2 Theoretical Analysis and Specifications

The most ideal specifications will be the largest values for stiffness and load as well as replicating the Flinders Hexapods specifications (Table 3.1). The maximum specifications for load were found in the literature review, Section 1.2.1. Cleather, Goodwin, and Bull (2013) found a travelling jumping created 10.4 times a person's body weight. If its assumed an average person is roughly 85 kg, the maximum force that may be created is 8672.04 N. Similarly, if a person weighed 100 kg, the maximum force would be 10000 N. It should also be noted that the Flinders Hexapods exerts a maximum load of 21000 N (Ding 2014). However, approximately 2100 kg force exerted onto a cradle with less than 20 mm material thickness will cause significant deformation of the material and therefore failure of the design. Eight thousand newtons will suffice for the hexapod to exert enough force on a joint

to hopefully fail it, however 10000 N is more ideal. Stiffness defines a structures ability to resist specimen deformation. This is extremely important specification as deformation of the specimen needs to be as accurate as possible. To ensure this, the stiffness should be orders of magnitude higher than the specimen. Magnitude orders are important because loads are very high and displacements are very small so errors are quite likely if displacement values are inaccurate, even by decimal points. Costi et al. (2008) notes 5000 N/mm as a benchmark for a spinal unit compressive stiffness. Therefore, it was ideal that the cradle would be order of magnitude higher than this value. The equation to evaluate stiffness is:

$$k = \frac{F}{\delta} \quad (3.1)$$

k denotes stiffness, F represents force and δ represents displacement. Another important consideration is the hexapods specifications. It is ideal to match the stiffness of the hexapod load frame. The stiffness values ranged between 2999-17773 N/mm. Therefore, it is important that the cradle stiffness will be within this range. Finally, to comply with the hexapod structure and material, the cradle will be manufactured in 304 Stainless steel.

Table 3.1: Maximum specifications for static analysis.

Specifications	**Maximum values**
Load (Knee)	10.4XBW travelling jump (≈8672 N for 85 kg person) (Cleather, Goodwin, and Bull 2013)
Stiffness (spine)	5000 N/mm (Costi et al. 2008)
Flinders Hexapod (Ding 2014)	
Stiffness	2999 - 17773 N/mm
Hexapod load	21000 N
Material	Stainless Steel AISI 304

Finite Element Analysis (FEA) was used to analyse this device. FEA is a computational technique which is used to optimise designs by precisely identifying the geometric structure via nodes and elements forming a mesh which is then used to create a set of equations to represent the elements. Then boundary conditions and material properties are applied, and the system is solved via mathematical methods such as differential equations and algebra. Subsequent results of stresses and strains are then calculated.

To fulfil the requirements of a static cradle pose, a lock system will be necessary to hold the position of the cradle. This will ideally be a lock that can withstand up to 10000 N load and increment the cradle to any degree of flexion. It was crucial that the design always maintains precision as accuracy is important for the validity of scientific testing.

3.3 Methods

Autodesk Inventor 2017 was used to design and create a 3D CAD model for the cradle device using fundamental geometry from Section 2.3. The Stress Analysis feature in Inventor was used to perform FEA on the cradle. Analysis and redesign was performed according to the specifications of stiffness and load. To simulate its real environment, the cradle was constrained onto the specimen pillar. Nodes and elements generated were approximately 227500 and 143600 for iteration 1, 288700 and 456990 iteration 2, as well as 446000 and 281508 for iteration 3, respectively. Material properties used were generated by Stainless Steel AISI 304. Poses performed were at 0º, 60º, 90º and 120º with a static load of 10000 N and design was reiterated until a sustainable model was obtained.

Table 3.2 Material properties for Stainless steel AISI 304 used for FEA analysis.

Material	Stainless steel AISI 304
Mass Density	$8\ \mathrm{g/cm^3}$
Yield Strength	$215\ MPa$
Ultimate Tensile Strength	$505\ MPa$
Youngs modulus	$195\ GPa$
Poisson's Ratio	$0.29\ ul$
Shear Modulus	$75.5814\ GPa$

Finally, an option for a cradle locking system will be designed.

3.4 Design results

A 3D CAD model was designed with sustainable mechanical joint connections that withstand specifications required. The mechanical joint consisted of a shaft press fit into the cradle with a grub screw, a ball bearing and housing to secure the joint. The shaft is designed to allow for clearance between the cradle and stand and a diameter capable of withstanding the torsion. The end of the shaft will consist of a washer and screw and be covered up by a bearing retainer. A bearing housing retainer is put on the end to ensure there is no movement of the bearing. The bearing is a radial deep groove ball bearing capable of withstanding load and stiffness as well as precision and fatigue life is required. Figure 3.1 demonstrates the joint design.

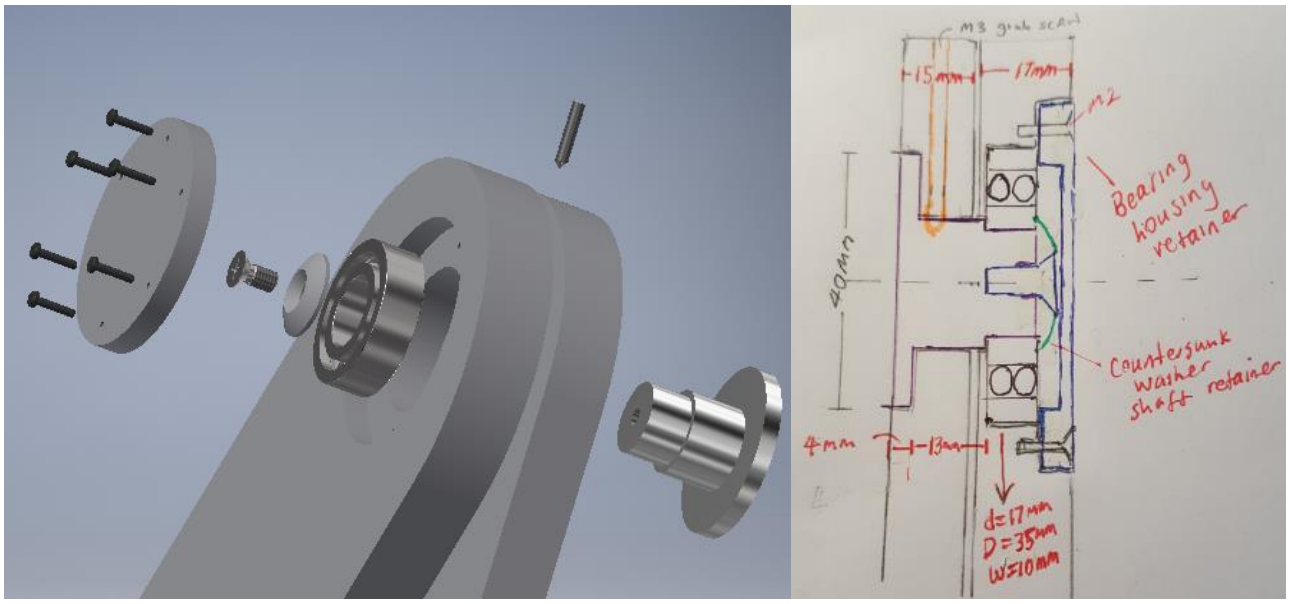

Figure 3.1. Mechanical joint for cradle rotational pivot point. Inventor model parts (left) and cross-sectional drawing of the mechanical joint (right)

Table 3.3 demonstrates the maximum stiffnesses and cradle displacements through 3 iterations. Iteration 1, with the fundamental cradle geometry found in Section 2.3, witnessed high displacements resulting in low stiffnesses. The maximum displacement seen for iteration 1 was 28.632 mm with a stiffness of 349.172 N/mm which will create a very unsuccessful cradle. Iteration 2 demonstrates an increase in thickness of the cradle to 12 mm from 10 mm and the stand and base to 15 mm from 10 mm. This showed an increase in stiffness by an order of a magnitude and therefore contained the same order of stiffness as the spinal segment. However, the lowest iteration is still 3263.03 N/mm with a large displacement on 3.40 mm. The third iteration involved providing further support to the stand and cradle via

gussets welded to the stand and further thickness to the cradle by 3 mm. Iterations 2 & 3 are shown in Figure 3.2. Highest displacements and subsequent stiffnesses are found at a cradle flexion of 90º in the z direction. The was the same angle as the hexapod coordinate system. Otherwise, cradle flexions of 60º and 120º contain the overall higher stiffnesses.

Table 3.3. FEA results for maximum displacement and stiffness values for 0, 60, 90 and 120 through three different iterations of the cradle design undergoing 10000 N load.

Iteration	**Axis**	**Cradle flexion angles (º)**			
		0	**60**	**90**	**120**
		Maximum displacement (mm)			
Iteration 1	**x**	0.45	14.33	6.94	15.99
	y	0.55	11.42	5.52	12.71
	z	0.25	25.26	28.64	27.04
Iteration 2	**x**	0.19	1.489	0.89	1.61
	y	0.19	1.48	0.83	1.61
	z	0.12	3.06	3.41	2.95
Iteration 3	**x**	0.11	1.36	0.58	1.47
	y	0.11	1.36	0.72	1.48
	z	0.10	2.68	3.08	2.70
		Stiffness (N/mm)			
Iteration 1	**x**	22092.9	697.77	1440.59	625.59
	y	18273.7	875.89	1810.93	787.09
	z	39226.9	395.82	349.17	369.87
Iteration 2	**x**	54725.6	6716.01	125053.5	6196.44
	y	52772.4	6725.85	12016.3	6182.42
	z	83810.4	3263.03	2933.51	3398.82
Iteration 3	**x**	87642.4	7355.48	17334.3	6785.64
	y	87926	7367.84	13855.5	6768.33
	z	101420	3724.99	3251.75	3701.67

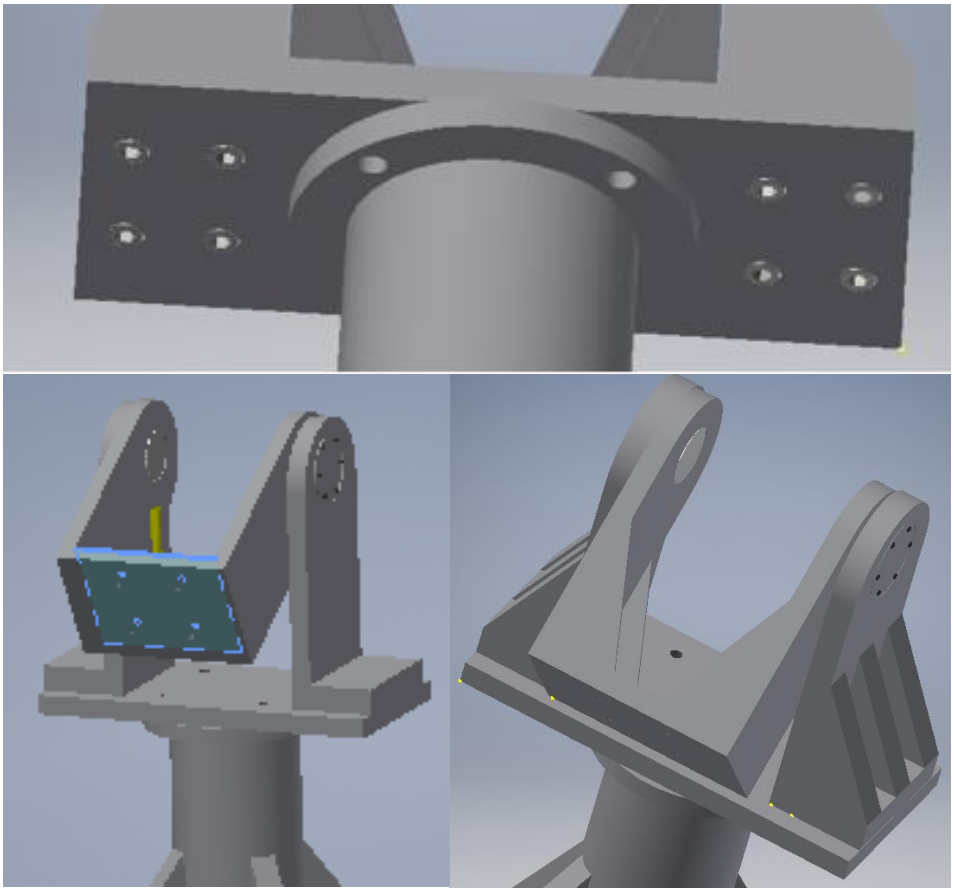

Figure 3.2. Cradle iteration 2 (left) and 3 (right) and bottom of cradle base (top).

The stiffness results were in the same order of magnitude as 5000 N/mm which is the stiffness for a biological specimen and contain the same stiffness range as the Hexapod where its lowest is 2999 N/mm and highest is 17773 N/mm. However, there are still high maximum displacements. The highest seen was 3.07 mm which will not provide accuracy and precision for the cradle. Therefore, a smaller maximum load will need to be determined. Table 3.4 contains values of stiffness for a load of 7000 N where the highest stiffness will be just on 5000 N/mm. Figure 3.3 shows an example of the area that all maximum displacements occur.

Table 3.4. FEA results for maximum displacement and stiffness values for 0, 60, 90 and 120 of cradle design undergoing 7000 N load.

Axis	**Cradle flexion angles (º)**			
	0	**60**	**90**	**120**
	Maximum displacement (mm)			
x	0.07	0.94	0.50	1.02

y	0.07	0.94	0.50	1.03
z	0.06	1.91	2.16	1.88
	Stiffness (N/mm)			
x	15248.9	10574.6	19944.8	9770.01
y	143208	10594.7	19809.8	9752.01
z	175356	5242.99	4639.98	5305.55

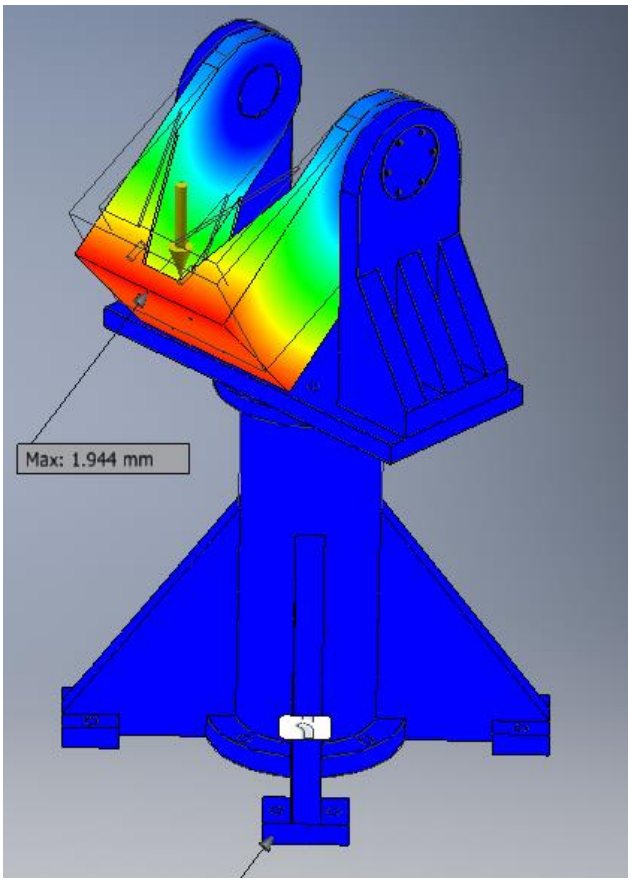

Figure 3.3. Maximum displacement for cradle at 60º of flexion.

To mechanically lock the cradle at certain degrees of flexion, rotational locking systems were explored. There were two viable design options found, including an indexing mechanism with stop and positioning control and a rotary lock system which would require an encoder for position measurement (Figure 3.4 & Figure 3.5). The indexing mechanism works via locking between teeth that are engaged only when a pin is slotted into holes which increase via a certain degree. This lock has 6° increments due to the number of teeth. The cradle shaft would be extended through the cradle and inserted into the bore of the lock. Rotation would occur when the lock is pulled out and the external toothing rotates with the cradle. To lock it,

the mechanism is pushed back in and the teeth will engage. Another system called the Rotary Lock System was found via the E&ESP website and it will lock the shaft in any degree of rotation (ESSP 2018). This lock system is normally locked, and a wrench is used to unlock and change position. Once the wrench is released it will automatically lock again. There is a shaft and keyway hole which the cradle shaft can be extended and inserted into allowing the CAM mechanism to interact with the spring, key system for locking (Figure 3.5). A positive for the indexing mechanism is that it also consists of the positioning tool. However this means that the locking system will not be precise, which is not ideal. Therefore this system was not be ideal. The rotary locking system does not have a positioning device but it does contain a more superior design with the ability to lock anywhere. This will mean that a position measure will need to be considered.

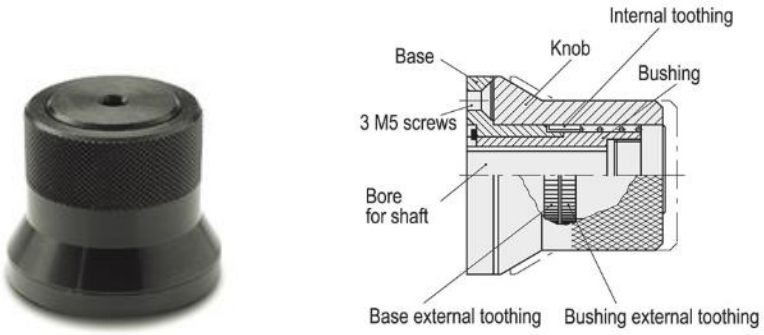

Figure 3.4. A position indexing device as a possible locking mechanism for the cradle. (Elesa 2018).

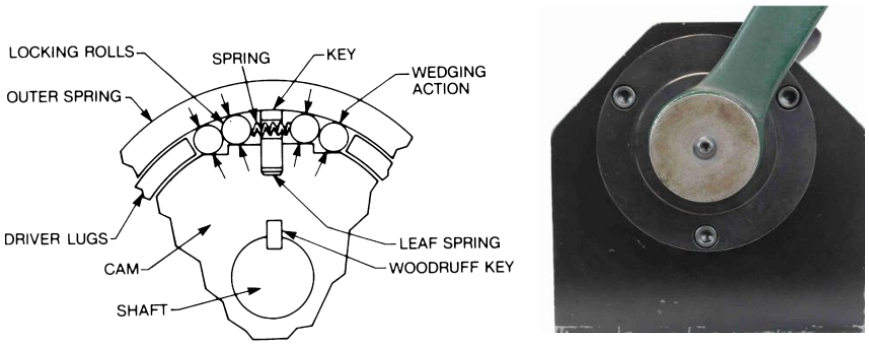

Figure 3.5. A rotary lock system (ESSP 2018).

A shaft diameter of 20 mm can withstand 271.16 Nm which will be capable of withstanding up to 10000 N. Therefore, this option is extremely viable however a position measurement will need to be found. There are many different types of position sensors that could be

chosen. A viable option would be a lightweight device, with high precision, capable of being attached to the other side of the cradle. Resolvers, encoders, magnetic position sensors etc. are all capable of performing this task. A SMART position sensor was chosen due to its weight and compatibility with the design (Honeywell 2018). It senses position through a magnet relative to the shafts position. Figure 3.6 demonstrated the way in which the sensor could be set up on the outside of the stand (Honeywell 2018).

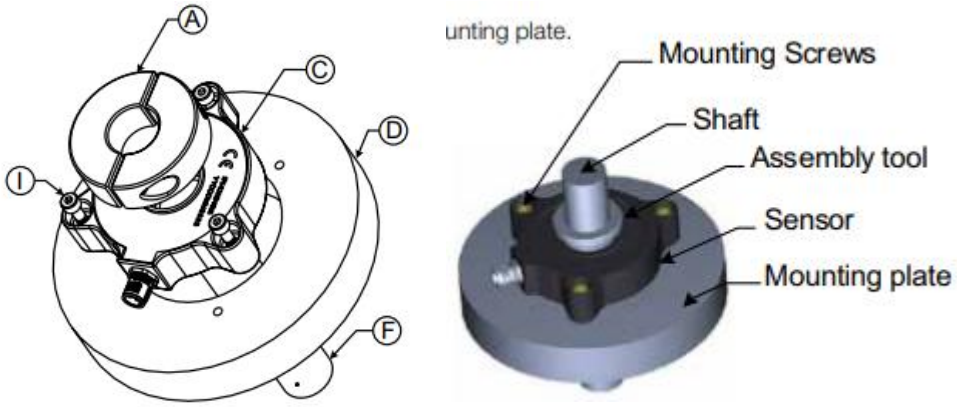

Figure 3.6. SMART position sensor for end of cradle (Honeywell 2018).

There will be only small adjustments to the cradle design. On both sides, the bearing retainer will be removed exposing the shaft. The countersunk screw and washer will be removed, and the shaft will be extended to the required distance. The locking system will require the adjustment of a keyway which will fit into their woodruff key. The shaft will be secured at the end of the lock via a washer and button head screw. Screws will be inserted through the locking system and through to the stand via three equidistance fixation points. The other side will require the shaft to protrude through the stand as well. This time the shaft is attached to an assembly tool which the shaft will be inserted to the position sensor.

3.5 Discussion and Conclusion

FEA was performed on cradle simulations of 0°, 60°, 90° and 120° enduring a load of 10000 N. The design of the cradle with the ideal geometry for the inner space of the cradle was used for iteration 1. However, displacements were as high as 28.83 mm with only 349.172 N/mm of stiffness. This will not suit the application, therefore after thicknesses was increased for the

base, stand and cradle. The adjustments created will result in specimen joints widths of 116 mm and 144.5 mm in length due to a thicker cradle base of 12 mm. A fixation cup of depth 8 mm instead of 13.5 mm can provide the specimen with its desired 150 mm length from joint centre to bottom of specimen. The height of the cradle due to the geometry of the inner space was a crucial part to the design requirements therefore the dimensions could not exceed these specifications. 170 mm from centre of rotation to cradle base demonstrated distances under 10 mm from encoder to cradle base. Therefore, this can't be altered and therefore the cup and specimen length needs to be sacrificed. This increased stiffness by an order of magnitude higher which was in the stiffness range of a biological specimen. To increase the stiffness even further, gussets and stand and cradle width were increased further. However, there was not a large difference between Iteration 2 and 3. The stiffnesses increased by only be 1000's not a full order of magnitude. The results show that the cradle stiffness will be just enough to fulfil the requirements of stiffness however the displacements of 3.04 mm are not ideal. The highest overall stiffnesses seen will be at 60º and 120º of flexion since the torque increased as it rotated through 90º and then beyond. Correspondingly, the highest stiffness will always be in the z direction at cradle flexion angle of 90º. The material used for simulation was Stainless Steel AISI 304 as it is the same material for the hexapod load frame, however other mechanically stiffer materials could be considered. Stiffness for 7000 N was also simulated. This showed an increase in stiffness of roughly 2000 N/mm.

The cradle was designed with the specifications of stiffness and load however further analysis of the pivot points should be performed. The bearing used for the design will not be suitable and a bearing with the ability to withstand high loads, precision and a good fatigue life is required. This will provide accurate information to inspect and simulate the joint further. Furthermore, at this stage an accurate factor of safety and failure analysis can be performed. Once this is performed, a logical step would be to manufacture the cradle with the lock system to see how it performs before adding automation to it. A manual lock system would be simple to set up and there would be no need to interface with the control system. Once again due to the inner space limitations there will only be large constraints of changing the design.

Chapter 4 Dynamic Simulation Analysis of Cradle Device

4.1 Introduction

Another crucial requirement is the ability of the cradle device to simulate dynamic tests. Therefore, the cradle design will need to withstand and cater for these requirements. Almost endless dynamic tests of many movement during various scenarios can be performed on human joints. Kinematic data could be simulated for a knee joint where the cradle will need to flex and extend according to that data while conjunctly withstanding corresponding physiological loads. Cyclic loading, stair climb motion, and numerous amounts of load and/ or position control tests could be simulated. Therefore, the design will require a motor and gearbox to automate the cradle device and be capable of withstanding and recreating the torque, velocities, load, accuracy and fatigue necessary for successful testing. The hexapod specifications will also be taken into consideration.

The aim of this chapter was to design the device to be capable of recreating and withstanding dynamic biomechanical tests. Section 4.2 will discuss the literature in forming specifications and analysing theory behind design and its required parts. Hence, Section 4.3 presents design analysis for integration with a motor and gearbox and discuss design comparisons and analyse costs required.

4.2 Theoretical Analysis and Specifications

4.2.1 Dynamic specifications

Section 1.2.1 discussed joint kinematics and found highest cited values in the literature to be $928.19 \pm 112.87\ °/s$ for plantarflexion of the ankle (Zhong et al. 2017) and torque of knee flexion in a sprint runner to be 218.6 ± 131.0 Nm (Sun et al. 2015). Both occurred while sprinting. These are absolute maximums that would not occur during regular testing, but it is important to know when investigating failure of joints and how to replicate this as closely as possible. The more important measure for velocity will depend on testing frequencies used during biomechanical testing. Frequencies will normally fall in the range of 0 to 1 Hz. 1 Hz

frequency is a full revolution of 360°/s which will be the upper range of frequency used. Torque will be determined via an analysis of the cradle structure while applying the maximum loads. It is also important that the systems accuracy is at least 0.01º. In addition, the cradle will need to withstand ongoing testing that may last 8 hours +. A motor will need to match these specifications as close as possible while keeping in mind the hexapods control specifications and control system. It will be ideal for the actuator to be controlled by the same Aerotech Soloist controller as the hexapod.

Torque represents the rotational force required to rotate an object. Therefore, the peak torque is calculated by the sum of load and inertia torque:

$$T = T_{load} + T_{inertia}$$

Load torques of a structure is defined by $|F||r|\sin(\theta)$ or $k\theta$ while torque inertia is defined by angular acceleration multiplied by inertia (I). Therefore, the torque equation is:

$$T = |F||r|sin(\theta) + I\alpha$$

This was calculated based on the structure of the cradle. First the load torque will be determined. The r value for the cradle is 170 mm. Calculating the highest torque at 90º was 5.53 Nm on one rotational point for a 304 Stainless Steel device. The moment of inertia, I, is determined via the actual cradle's structure where the rotational pivot point is the centroid of the shape. The parallel axis theorem will need to be calculated for the cradle structure to obtain inertia. The structure will be broken down into three components.

$$I = \sum I_y + \sum mdx^2$$

$I_y = \frac{1}{12}m(h^2 + w^2)$ where w represents the width and h represents the height and m represents mass and $x = \frac{\sum yA}{\sum A}$. This value was calculated via Inventor Autodesk. Inertia of the cradle was found to be $0.200443\ kg/m^2$. At a frequency of 1 Hz, the torque will be 6.78 Nm. A load of 1000 N was analysed for torque loads as this was the most important calculation, and results shown in Table 4.1. This torque would simulate kinematic walking for load and position and countless position control studies however it will by no means reach jumping or 10 times body weight. Torque specifications were solely dependent on the highest torque possible for a motor with the correct size. The ability to apply load was also critical, therefore the size of a smaller person can become the minimum value for the lowest torque. A small person could be roughly 60 kg. Substituting this into the load torque equation provided

a torque of 50.99 Nm. Therefore, this was the cradles lowest torque. Finally, specifications were summarised (Table 4.2).

Table 4.1. Determines the torque load for various ranges of cradle flexion at 1000 N

Cradle Flexion	Torque (Nm)
45º	90.151
70º	123.3347
90º	131.2500
120º	113.6658

Table 4.2. Dynamic specifications required to fulfil cradle design.

Specification	**Value**
Torque	Absolute lowest 50 Nm
Speed	60 rpm
Accuracy	0.01º
Fatigue	10^7
IP rating of motor	IP65
Compatibility with hexapod	Motor compatible with soloist controller

4.2.2 Robotic mechanisms

Rotational motors usually come in the form of DC motors which may be brushed, brushless, servomotors or stepper motors. Brushless DC motors are precise and compact due to their ability to achieve maximum torque at any point of rotation. These motors also contain longevity since there are no brushes to maintain. The main feature of stepper motors is their precise positioning due to their poles. However, this application requires high performance for torque and changes in dynamic load as well as position control. Therefore, an ideal motor will be a brushless servomotor. Standard servomotors of 1.3 Nm are roughly 1.5-2 kg, depending on brand, and they are approximately 100 mm in length. This means an appropriate gear will need to be chosen.

A standard planetary gearbox is made up of four components including the sun, planet gear, ring gear and carrier. The sun gear in the input that drives the planet gears which will cause the carrier to change its speed. Multiple sets of these arrangements are set up to increase

torque. Other gear types are trochoidal and cycloid gears which will contain trochoidal and cylindrical shapes to allow for a different configuration of gears which produce the ability to withstand high axial and radial load (Motiontech 2018). Another gear called a strain wave gear minimises space substantially due to its configuration. It is made up of three parts consisting of a wave generator, flex spline and circular spline. The wave generator is an elliptical shape with a thin raced ball bearing that drives the transmission. Rotating this part will create a waveform onto the flex spline which is a stiff and robust component capable of transmitting high torques via its external teeth. The wave generator will be inserted into the flex spline which will recreate its shape by radial deformations. The outside of the flex spline consists of external teeth. Therefore, when this is inserted into the inner area of the circular spline, it will engage with its internal teeth and rotate around the circumference to create a geared system.

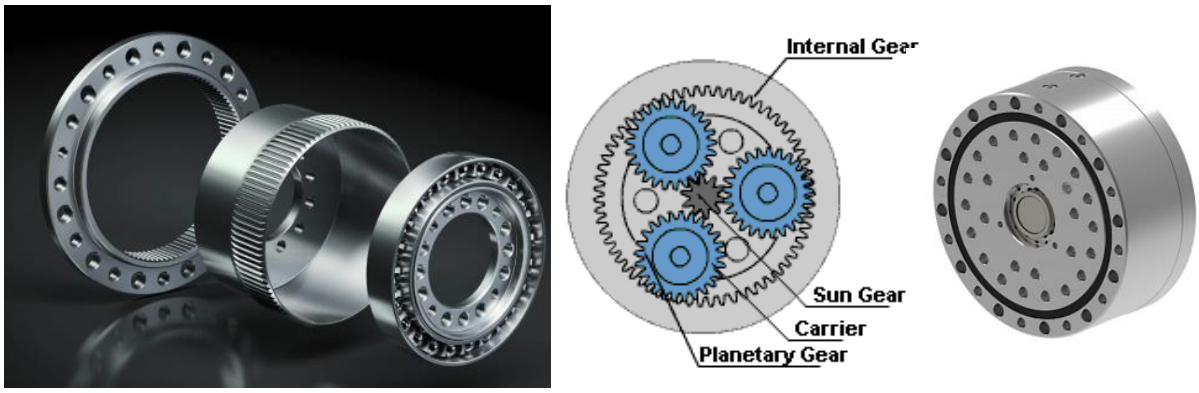

Figure 4.1. Strain wave gear (left), planetary gear (middle) and trochoidal gear (right) (Motiontech 2018; apexdyna 2018; Harmonicdrive 2018).

Some important equations when analysing motor and gearbox options are listed below:

$$\tau_{overall} = \tau_{motor}.\, i_{gear\ ratio}.\, E_{efficiency}$$

$$i_{gear\ ratio} = \frac{n_{motor}}{n_{output\ speed}}$$

$$Inertia\ ratio = \frac{I_l}{I_m}\ where\ I_l\ is\ load\ inertia\ and\ I_m\ is\ motor\ inertia$$

$$T_{average\ torque\ (RMS)} = \sqrt{\frac{T_p^2 t_1 + (T_L + T_F)^2 t_2 + \left(T_J - T_L - T_F\right)^2 t_3}{t_1 + t_2 + t_3 + t_4}}$$

$t_1\ is\ the\ acceleration\ time\ , t_2 is\ the\ run\ time, t_3 is\ the\ deceleration\ time\ t_4 is\ the\ dwell\ time,$
$T_L\ is\ torque\ load, T_F\ is\ torque\ friction, T_J\ is\ torque\ inertia\ and\ T_p\ is\ peak\ torque$

4.3 Design analysis

4.3.1 Motor Selection and design

Research was conducted into specific robot mechanisms and possibilities of satisfying the specified requirements as well as maintain a compact space between the cradle and the hexapod encoders. Many motor and gear combinations were investigated with three distinct styles identified. Each of these styles will be discussed. It is also important to note the space from the side of the cradle stand to the encoders can be found via methods in Chapter 2. The length width calculated to account for the motor will be approximately 100 mm. The space at the front of the hexapod will also allow for room between the encoders as they are 248 mm apart. Figure 4.2 demonstrates the best possible designs for the cradle actuator. The first possibility is a right-angled gear which will allow the motor to lie parallel to the cradle. Therefore, only the gearboxes right angled distance will need to be accounted for. Another solution is a belt and pulley system where the pulley will be attached to the stand and the rotational shaft and there will be a motor sitting parallel to the shaft on the base plate. The third option is the harmonic drive consisting of the strain wave gear.

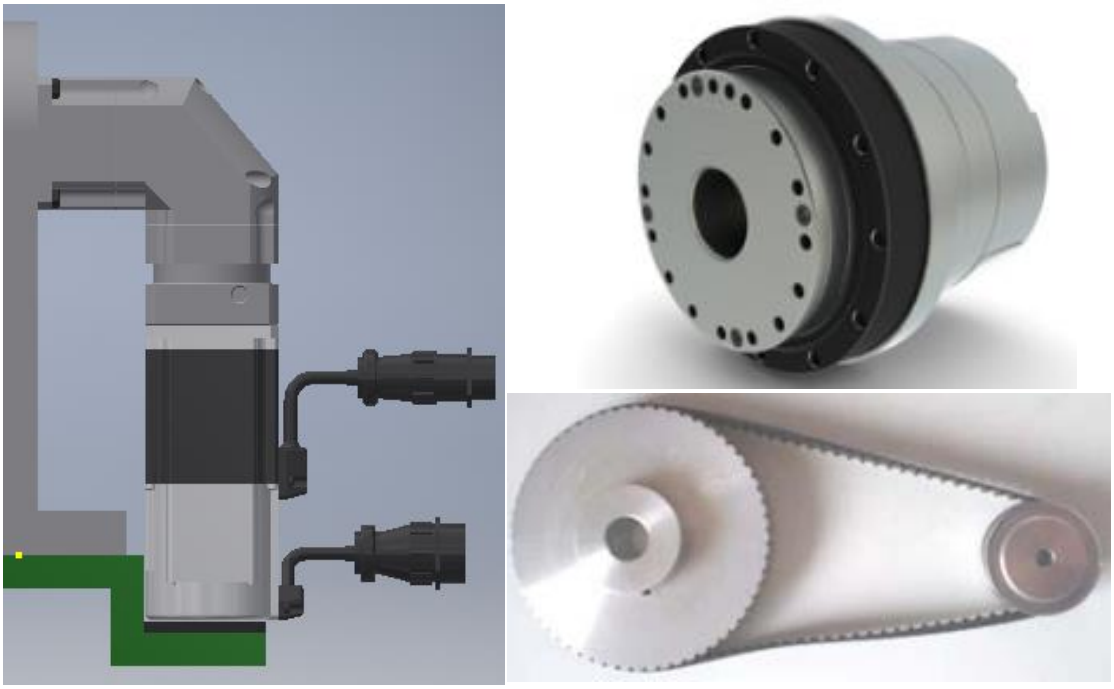

Figure 4.2. Options for dynamic control of cradle. Right angled gear (left), harmonic drive (top right) belt and pulley (bottom right).

Selections for these choices will mainly depend on its size and required specifications. The smallest actuator is required to fulfil the specifications. The right-angled gear found with a nominal torque of 45 Nm was an Apex Dynamics ABR060 stage -1 gear ratio of 25 (apexdyna 2018). A greater torque required a larger sized gearbox. The length to the back of the gearbox is 108 mm with a width of 60 mm. This may mean the encoders and in line with the motor in the y axis. However, the width will mean that the encoders should steer clear as they are 248 mm apart. Other specifications of this gearbox include a zero backlash and a radial load of 1530 N. This means that the gearboxes shaft can't support the load and a capable bearing will need to withstand the load instead. Pairing the gearbox with a standard motor of 1.3 Nm, specifically an Allen Bradley TLY-A230 will provide a continuous torque of 30 Nm with capabilities of producing 50 Nm intermittent. The speed produced by this combination will be 200 rpm. A larger motor that will cost more money, weight and size could be used to slightly increase torque. This torque was the highest that could be achieved in the space with a planetary gear and standard motor. The combination will also provide 2.1 kg weight for the gearbox and 1.8 kg for the motor. Total weight will be 3.9 kg for this system. There are many downfalls with to this combination as it sits on the low range of specifications required for the application. Therefore, this design was abandoned however, it will continue as an option for thorough analysis.

Another option that should be mentioned is a belt and pulley set up. A belt and pulley system would free up the space at the side of the cradle and avoid any danger of reaching the encoders. The configuration for the motor and pivot point is demonstrated in Figure 4.3. The rotational shaft would be extended and attached to a bearing pillow and pulley via a keyway. This configuration should be less than approximately 60mm. A timing v belt would be used to attach to the corresponding parallel pulley. This pulley would be attached to the shaft with a bearing pillow supporting the outside. The base plate would need to support this load exerted on the back of the plate. With this configuration, the type of motor and gearbox could be extended as long as required. However, this design will also bring in more room for error. There may be issues with the tension, belt stretching, slippage and deterioration. This may cause differences in the speed of testing and wear quicker with fatigue testing. It will also increase the load of the shaft and bearing which is already an issue. The speed from the driven pulley will also be less than the motor pulley which may cause issue as the speed has been significantly decreased from the gearing. There will also be a large weight for the motor which will sit on the end of the base plate. This section of the base plate will not be secured

to anything as the specimen pillar is less than 130 mm in circumference. Despite this, it is still a viable option if designed carefully.

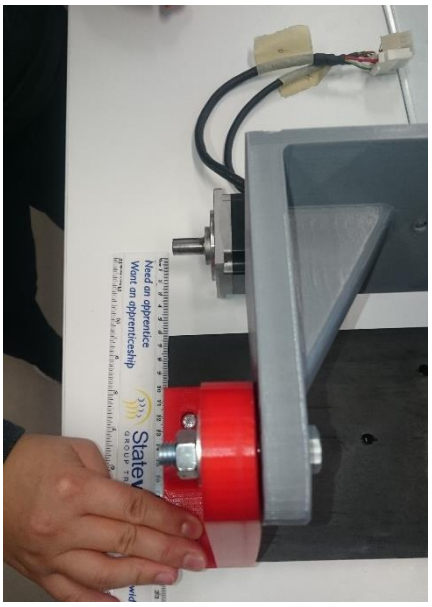

Figure 4.3. Configuration for possible tooth belt and pulley system.

The next option involves a specialised strain wave gear. The option from this variety was the SHA actuator (25A81SG) from Harmonic Drive. This is a Japanese company specialising in strain wave gears. This system includes features that largely align with the specifications. This actuator is a brushless servomotor that includes the unique gear which significantly decreases the length of the motor. The chosen motor has a length of 93.5 mm from fixation to the stand extending through the actuators back. This will be just perfect to insert into this space. The combination of gear and motor is also already combined into one package which will decrease risks of a gearbox and motor system that is paired together without testing. The actuator produces a continuous torque of 58 Nm with a maximum torque of 178 Nm. These values are quite substantial for the size and weight of motors. While torque would ideally be higher, it would be capable of simulating kinematics of motion and loading during walking and position control simulations. It also just fulfils the speed requirements at 59.3 rpm continuous. The brake and encoder parts are also combined in with this system to allow for accurate position feedback and static testing. Further specifications can be found in Appendix D.

Provided that the actuator will coincide with the inner space of the cradle and hexapod assembly, the specifications and size deemed it as an extremely superior system which should be investigated further. Appendix D provides a drawing of the actuator. Figure 4.4 demonstrates the connection of the SHA actuator to the cradle device. It contains a hollow shaft rotating gearhead which will need to be attached to the cradle. Countersunk screws were inserted through the inside of the cradle, protruding out and into the gearhead containing 15 M4x7 holes. The outer part of the actuator contains fixation holes which will be attached to the stand. The stand will consist of a space for the rotating gear and 1 mm clearance. Countersunk screws will fixate the actuator from the inside of the stand through the outside and into the actuator. The screw will protrude out of the motor and a nut will be threaded on to the end of the screw.

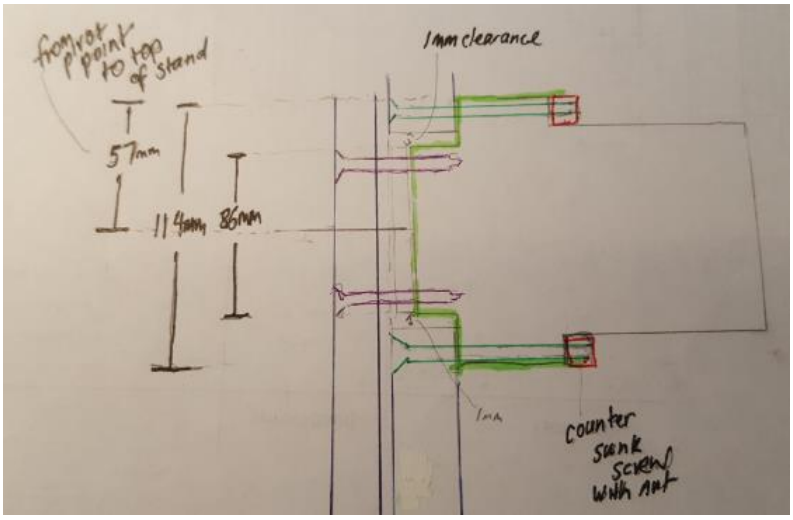

Figure 4.4. SHA actuator connection to cradle via stand. Countersunk screws used to secure cradle to motor (purple) and motor to stand (green).

Figure 4.5 & Figure 4.6 demonstrates the cradle and actuator assembly. These dimensions were derived in Chapter 3 and provided here for the design. The dimensions include a cradle thickness of 15 mm, with the rotational pivot point of 162 mm. Each side was altered to suit the mechanical connection. The stand thickness is 17 mm with an overall height of 237 mm. The rotational point will also be increased by 5 mm as the base thickness was increased by 5 mm. The actuators diameter at the fixation point is 114 mm. This meant that the stand width

was increased to suit the actuator, however the cradle itself was left at 100 mm as the geometry of the hexapod cannot account for another increase in width. Drawings of these parts are found in Appendix E. The geometry will need to be reassessed using methods in Chapter 2.

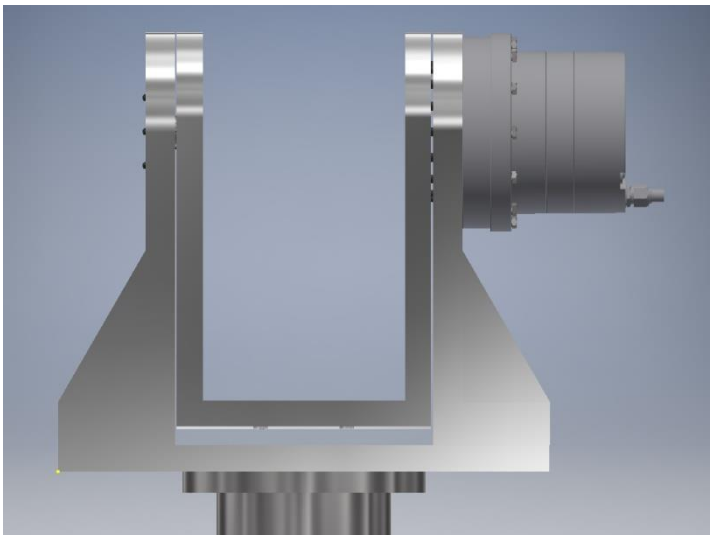

Figure 4.5. Front view of cradle device with SHA actuator from Harmonic Drive.

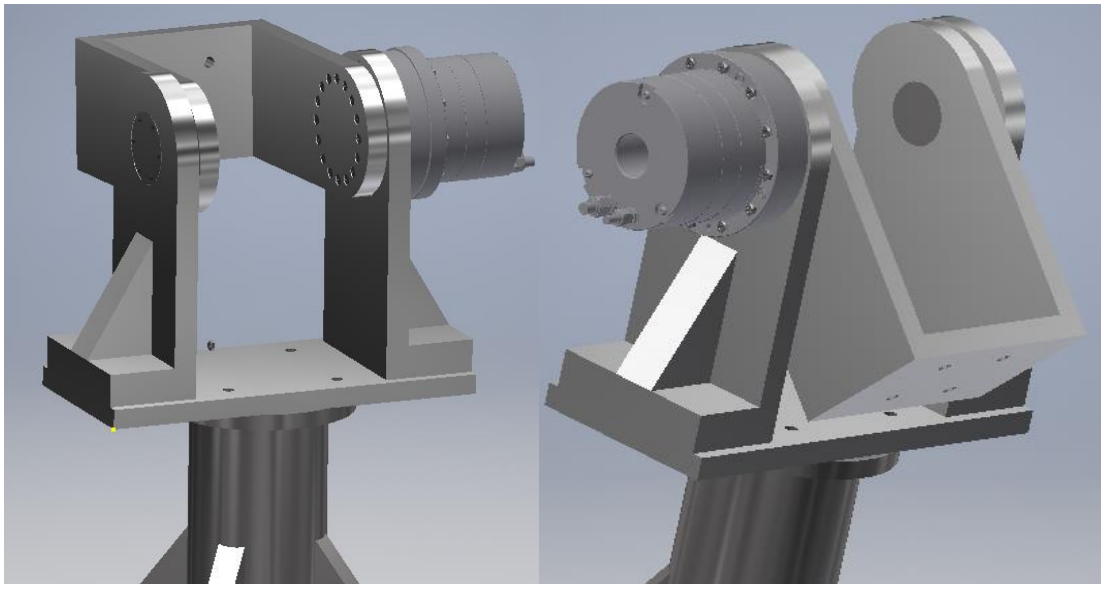

Figure 4.6 View of cradle and SHA actuator assembly at 90° (left) and motor view side (right).

4.3.2 Confirming overall Geometric Constraints

It is crucial that these actuation systems are confirmed with the geometry of the hexapod. Therefore, the program used to produce the distance between encoder to cradle in Chapter 2 is required. Analysis was performed by picking the edges of the motor geometry that would be closest to the related encoder part. The closest motor point to encoder was determined via

the width. This was performed on both sides because the distance closest to the encoder will be determined via the robot pose. The neutral pose was determined first to check the calculations. The SHA distance to encoder 4 in the y direction was -12.04 mm and 79.01 mm in the x direction. Its overall distance for encoder 4 and 3 was calculated to be 79.92 mm and 80.55 mm, respectively. The right-angled gear protrudes further through the hexapod inner space. The decrease in width of the gear will improve the distance. Therefore, the distances from the gearbox to encoder 4 and 3 were 95.51 mm and 96.16 respectively. Table 4.3 demonstrates the computational calculations for the end ranges of motion. It confirms that the space in the x direction between encoder 4 and 3 provide the distance required for either motor.

Table 4.3. Computational measurement from hexapod encoder to motor.

Hexapod pose		**Distance from encoder to motor**			
Position	**Angle (°)**	**SHA actuator**		**Right angled gear**	
		Encoder 4	*Encoder 3*	*Encoder 4*	*Encoder 3*
Rx	**20**	90.15	90.78	106.66	107.25
	-20	65.42	66.13	81.92	82.63
Ry	**20**	78.11	80.08	94.61	96.58
	-20	79.44	78.76	95.94	95.26
Rz	**15**	97.22	61.28	113.72	77.78
	-15	60.54	97.77	77.04	114.27

Chapter 5 Overall Cradle Design Choice

5.1.Design Comparison

5.1.1. Cradle design options

Specifications for the Harmonic Drive versus Apex Dynamics gearhead (right-angled gear) and motor are listed in Table 5.1. The Harmonic drive was far superior over the right-angled gear with a difference in continuous torque of 33 Nm. However, the opposite was shown for speed as the right-angled gear had a speed of 150 rpm while the harmonic drive was 59.3 rpm. The more important specification is torque. It is crucial to withstand as much load as possible. Another factor to consider is the weight of both devices. The harmonic drive is 3.1 kg and sits on the pivot point with its load distributed around it, whereas the right-angled gear is 3.96 kg which is approximately 800 grams more. This is quite heavy to have on the pivot point of a small structure like the cradle. Anything above 4 kg for these designs should not be considered. Both also maintain an IP65 water/dust rating and no backlash. These will meet the specifications of the cradle. Lastly, the specifications for the encoder and brake were also sufficient as they will be compatible with the Soloist controller. This controller contains 10/20 Amps for continuous and peak current which far exceed the current required for the both systems. From these specifications it is seen that the Harmonic Drive is superior in specifications and will more closely align with the requirements than the right-angled gear. However, the delivery time is 30-40 weeks. Another design to remember is the belt / pulley system. This was not listed on the table because the design will benefit motor specifications as more room will allow for a bigger motor and gear. Therefore, specifications can be flexible. However, ramifications of a large load at the end of a base that is sitting in mid-air will need to be analysed further.

Table 5.1. Specification comparison between harmonic drive and right-angled configuration

Specifications	**Option 1: Harmonic Drive**	**Option 2: Apex Dynamics Gearhead ABR060 20:1 + HIWIN motor FRLS4020506A**
Torque (Nm)	58 / 178 (cont.) (other option: 35 / 127)	25 (cont.) 40-50 (20 sec intermittent)
Speed (rpm)	59.3 (94.1)	150 (rated speed) 225 (no load maximum)
Weight (kg)	3.1	2.1 + 1.86 = 3.96

Backlash (arc-min)	0	Micro P0, P1 <=4, P2 <=6
IP	IP54	IP65
Dimension (mm) (width of gear)	93.5	108
Current (A) (cont./peak)	4.7/13.0	2.5/7.5
Brake max voltage	DC24V ± 10%	24 VDC ±10%
Encoder interface	multi-turn magnetic absolute encoder, 17 bits,	Incremental signal/hall signal
Timeframe	30 to 40 weeks	2-4 weeks

Unfortunately, all cradle design options did not meet specifications of joint failure. Even though the torque for the SHA actuator is 58 Nm, Table 4.1 demonstrates that torque for a load of 1000 N will be greater than 113.66 Nm. Therefore, the SHA actuator will not be capable of withstanding 10000 N or even 7000 N. The specifications for failure may be farfetched for the design and geometric constraints. Larger actuators could be explored further and other actuators from Harmonic Drive may provide larger torques and still be suitable for the cradle and hexapod assembly. The method to secure the cradle to the SHA motor will also need to be analysed further as it may not be strong enough to withstand loads. The SHA motor can currently perform position tests as well as loading such as walking however the right-angled gear may have difficulty even doing that. Trade-offs for specifications will need to be negotiated for the success of the device. One positive was that geometric requirements were successful for both designs.

5.1.2. Cost Analysis

Budget constraints will also play a role in deciding what kind of design is suitable. Table 5.2 summarises quotes received for the SHA actuator and Right-angled gearbox combination. The pulley system was approximated. Because the motor can be a similar combination to the right-angled gear just with more possibilities and an inline gear. The cost comparison indicates the SHA actuator will be the most expensive at $4936. However, the pulley system is only going to be approximately $1000 less. Considering this train of thought would suggest that $1000 is worth investing in for an accurate and superior system. The right angled-gear is the cheapest but still expensive for its specifications.

Table 5.2. Cost comparison for parts used in each system.

Part ($)	SHA actuator	Right angled	Pulley system
Motor	4936 SHA25A81SG	1230 TLY-A230P (incl. encoder and brake)	≈1230
Gearbox	incl. above	1413.10 ABR060-025-P0-S2	≈1413.10
Cables	incl. above	200	
V-belt and pulley	-	-	≈1000
Total ($)	4936	2843.1	≈3643.1

5.2. Final Cradle Design Choice

The most desirable system will be the cradle device driven by the SHA actuator. This system will provide the cradle with the ability to form any static or dynamic position testing. Cyclic testing with smaller loads will also be satisfactory. The cradle stiffness and structure will suffice for these types of tests however they still need to be analysed further if load of up to 10000 N is necessary. Further analysis should also be performed on the mechanical connections and deformation of the cradle at 90°. The main success for the cradle design was the geometry. This is the most crucial constraint as failure of this would result in encoder damage. The analysis provided in Chapter 2 will be useful moving forward and for any other design in the hexapod. Another point to discuss is the fund to purchase the actuator. This may require time to generate however it should be invested in as it is the key hope for a successful increase in range of motion in the hexapod. A fall-back design will be the belt and pulley configuration as it will be capable of meeting specifications however the design will need to account for all the additional factors that could go wrong.

Figure 5.1 & Figure 5.2 demonstrate a successful implementation of the cradle in the Flinders Hexapod. Figure 5.1 provides a front view from the side which shows the actuator does not come near the encoder on the right side (third leg). Figure 5.2 validates the cradle base and second encoder interaction while showing the actuator will be at a safe distance away from encoders 3 and 4.

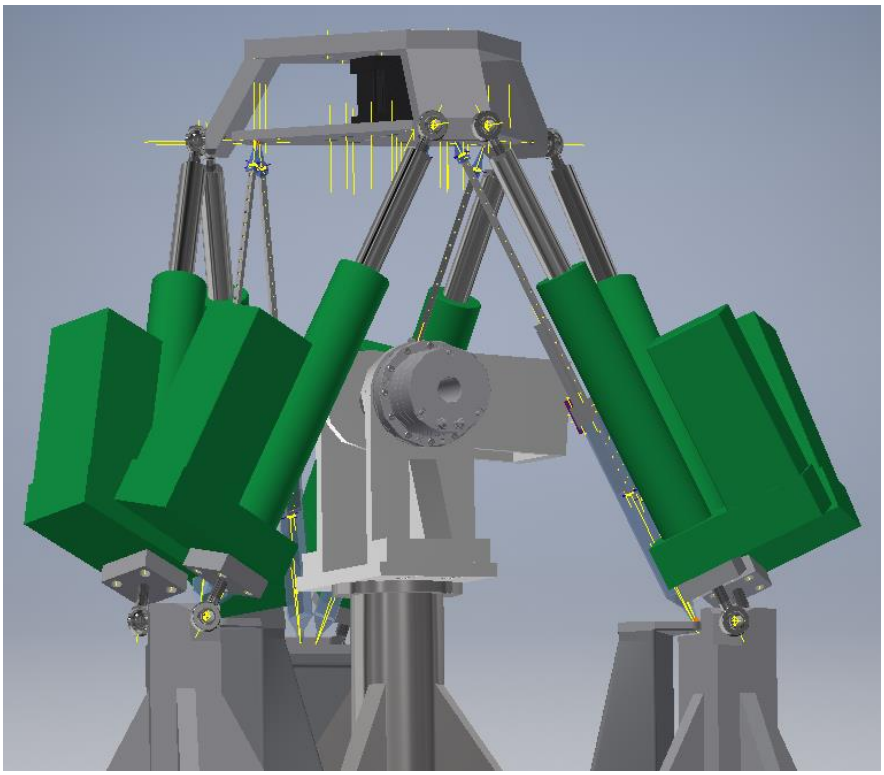

Figure 5.1. The hexapod, cradle and SHA actuator assembly.

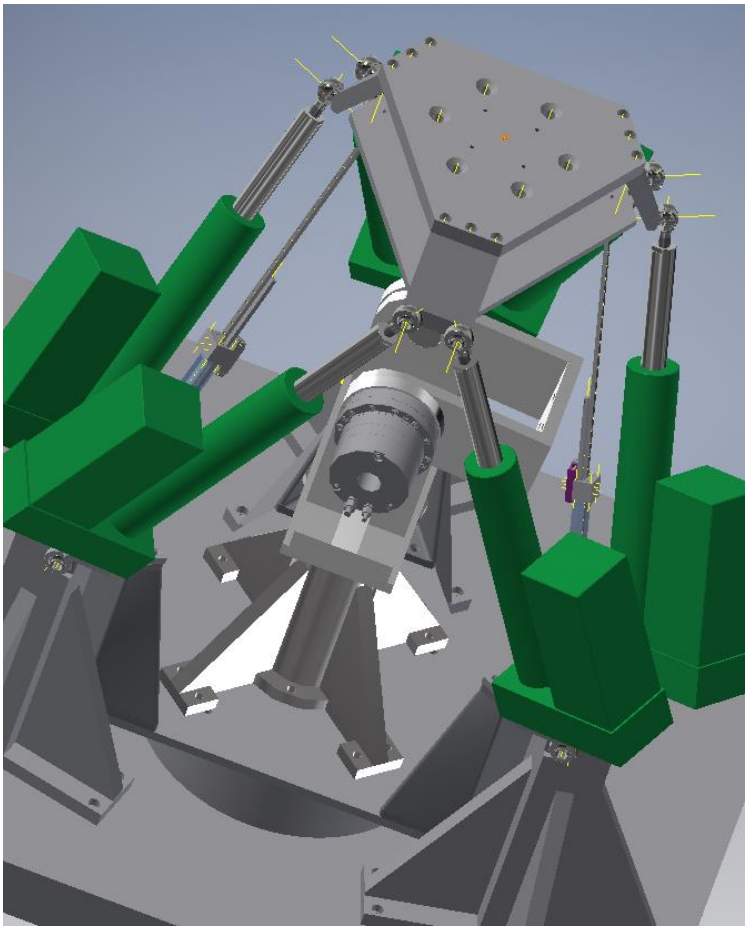

Figure 5.2. Birds eye view of the cradle, hexapod and SHA actuator assembly.

The project has many complexities due to the challenging requirements, small inner space of the hexapod and the already complex control system. The cradle and hexapod assembly geometry demonstrates that it is possible to perform biomechanical testing for large range of motion. However true physiological loading requirements is and will always be difficult to cater for.

A realistic plan is required to bring the cradle to fruition. The first step is to redefine and reanalyse the cradle requirements. The design cannot not afford many other changes in geometry while cradle gussets did not sustainably improve the stiffness. Research into a suitable a bearing is required and therefore the alterations to shaft and mechanical joint. Once this has occurred, the cradle can be manufactured with the rotary locking system on one side. This will only involve protruding the shaft to through the stand, then altering it with a keyway and attaching the stand to the lock. This model should take into consideration the geometry required for the cradle with the SHA actuator. Considering possible swap of lock and motor allows the cradle to be remanufactured. Since the stands are bolted in with M8

screws through the base plate and up to the stand, a suitable stand can be remade for the SHA actuator, and the cradle will just need to also be readjusted to suit the SHA actuator. This method of using the lock system first will ensure the cradle structure success and confirm the success of kinematics of cradle and hexapod assembly. This can be a short-term plan for research requiring a large range of motion. During this time, expertise into integrating the cradle into control system and applying for funds to purchase the cradle can take place. The hexapod is currently undergoing updating and re-programming therefore it is realistic for the cradle actuator and control system to be implemented after this. The backup plan for the cradle will be the pulley and belt system. This plan will ensure the safety of the hexapod and validity of the research performed. Finally, there are many risks in implementing this kind of device into the already complex control system. This means safety measures will be crucial to include as the interaction between the cradle and hexapod need to be exactly right. Encoder coverings should also be a consideration as the encoders and in a risky position.

Chapter 6 Conclusion and Future Work

6.1 Conclusion

The cradle was successfully implemented kinematically and spatially. However, the static and dynamic specifications were not met for the cradle design. The specifications were based on failure loads found in the literature which, in hindsight, were unrealistic for the cradle design and requirements should be redefined. Despite this, the best design of the motor and cradle was found given the inner space of the hexapod as the geometric constraints. The geometry is number one priority.

Geometric constraints as well as hexapod and cradle kinematics were explored computationally and physically. Computational methods were explored using kinematics and 3D vector geometry. Validation methods included a prototype and physical assembly of the device. End ranges of motion of the hexapod and cradle confirmed a tight but feasible gap in all direction. -R_y maintained the smallest distance however this wouldn't be realistically used for testing. Instead, the cradle could create extension. More importantly, it was found that the hexapod could successfully flex 20° in the R_y direction while the cradle flexion was 120°. Therefore, a complete range of motion for the hexapod and cradle assembly was 140°.

Static analysis of the cradle was investigated. Reiterations of the cradle design was performed using FEA to analyse the stiffnesses. The cradle was successfully in the order of magnitude of a biological specimen and hexapod however the deformations of 3.07 mm were still undesirable. A rotary locking system was also included as a method for static analysis. Dynamic simulation requirements were discussed, and an analysis of motor and gearbox selection was performed. The final selection was a Harmonic Drive system called the SHA actuator which uses a unique strain wave gear that minimises the space required. A realistic plan to completely integrate the cradle was discussed. First the cradle should be made with a locking system which will validate the cradle and provide short term testing. Then the SHA actuator can be implemented when funding and expertise is provided for the control system.

The cradle increases range of motion within the hexapod which provides the simulator with the ability to test more joints. This device improves the research depth for in vitro biomechanical testing and the Flinders Biomechanics & Implants laboratory.

6.2 Future Work

Section 5.2 presents the final cradle design for this thesis. First, the cradle should be produced with the rotary locking system to validate its structure and geometry. Once integration into the hexapod control system is possible, the SHA actuator can be implemented. Further checks and detailed inspections should also be made to ensure the safety and fatigue of the design. This will also involve renegotiating requirements and specifications. Possible larger sized torques can be found with other Harmonic Drive actuators. This should be investigated.

Funding for manufacturing and purchase of the SHA actuator should be found first. Parts can then be purchased. Manufacturing time will need to be organised with the Engineering Services Group at Flinders University.

Implementation of the control system should include methods for accuracy of cradle, error propagation and validation of entire system. LabVIEW should be used to integrate the cradle control system into the Hexapods. A suitable user interface should be developed with safety features for the hexapod and the cradle.

References

Anandacoomarasamy, A., I. Caterson, P. Sambrook, M. Fransen, and L. March. 2007. 'The impact of obesity on the musculoskeletal system', *International Journal Of Obesity*, 32: 211.

Annemieke V, H, Karel D, R, Tom, C, Matthieu D, B, Peter, V, Patrick De B. 2013. 'Pilot validation study on a quasi-static weight-bearing knee rig', *Proceedings of the Institution of Mechanical Engineers, Part H: Journal of Engineering in Medicine*, 227: 229-33.

apexdyna. 2018. 'Right Angle Planetary Gearboxes', Accessed 10/10. http://www.apexdyna.com.au/index.php/products/right-angle-gearboxes.

Bell, K M., R A. Hartman, L G. Gilbertson, and J D. Kang. 2013. 'In Vitro Spine Testing Using a Robot-Based Testing System: Comparison of Displacement Control and "Hybrid Control"', *Journal of Biomechanics*, 46: 1663-69.

Bell, Kevin M., Fabio V. Arilla, Ata A. Rahnemai-Azar, Freddie H. Fu, V Musahl, and R E. Debski. 2015. 'Novel technique for evaluation of knee function continuously through the range of flexion', *Journal of Biomechanics*, 48: 3728-31.

Bergmann, T F., and D H. Peterson. 2010. *Chiropractic Technique 3rd Edition Principles and Procedures* (Elsevier Mosby: St. Louis, Missouri).

Bonner, Tara F., Robb W. Colbrunn, John J. Bottros, Amar B. Mutnal, Clay B. Greeson, Alison K. Klika, Antonie J. van den Bogert, and Wael K. Barsoum. 2015. 'The Contribution of the Acetabular Labrum to Hip Joint Stability: A Quantitative Analysis Using a Dynamic Three-Dimensional Robot Model', *Journal of Biomechanical Engineering*, 137: 061012-12-5.

Chevalier, A, M Verstraete, C M Ionescu, and R De Keyser. 2017. 'Decoupled control for the bicycling UGent knee rig : design, implementation, and validation', *IEEE-ASME TRANSACTIONS ON MECHATRONICS*, 22.

Chokhandre, S, R Colbrunn, C Bennetts, and A Erdemir. 2015. 'A Comprehensive Specimen-Specific Multiscale Data Set for Anatomical and Mechanical Characterization of the Tibiofemoral Joint', *PLoS One*, 10: e0138226.

Cleather, D J., J E. Goodwin, and A M. J. Bull. 2013. 'Hip and knee joint loading during vertical jumping and push jerking', *Clinical biomechanics (Bristol, Avon)*, 28: 98-103.

Colbrunn, R. W., J. J. Bottros, R. S. Butler, A. K. Klika, T. F. Bonner, C. Greeson, A. J. Van Den Bogert, and W. K. Barsoum. 2013. 'Impingement and stability of total hip arthroplasty versus femoral head resurfacing using a cadaveric robotics model', *Journal of Orthopaedic Research*, 31: 1108-15.

Coles, L. G., S. Gheduzzi, and A. W. Miles. 2014. 'In vitro method for assessing the biomechanics of the patellofemoral joint following total knee arthroplasty', *Proceedings of the Institution of Mechanical Engineers, Part H: Journal of Engineering in Medicine*, 228: 1217-26.

Costi, J. John, A. Ian Stokes, G. Mack Gardner-Morse, and C. James Iatridis. 2008. 'Frequency-Dependent Behavior of the Intervertebral Disc in Response to Each of Six Degree of Freedom Dynamic Loading: Solid Phase and Fluid Phase Contributions', *Spine*, 33: 1731-38.

Debski, R E., S Yamakawa, V Musahl, and H Fujie. 2017. 'Use of Robotic Manipulators to Study Diarthrodial Joint Function', *Journal of Biomechanical Engineering*, 139: 021010-10-7.

Ding, B. 2014. "A study of a Gough-Stewart platform-based manipulator for applications in biomechanical testing." In, edited by Boyin Ding, Benjamin Seth Cazzolato, John Jack Costi, Steven Drummond Grainger and Engineering School of Mechanical.

Ding, B, R M Stanley, B S Cazzolato, and J J Costi. 2011. "Real-time FPGA control of a hexapod robot for 6-DOF biomechanical testing." In *IECON 2011 - 37th Annual Conference of the IEEE Industrial Electronics Society*, 252-57.

Duan, X, J Mi, and Z Zhao. 2016. 'Vibration Isolation and Trajectory Following Control of a Cable Suspended Stewart Platform', *Machines*, 4: 20.

Elesa. 2018. 'GN 200 Indexing mechanisms with stop and positioning device ', ELESA S.p.A., Accessed 10/10. https://www.elesa.com/en/elesab2bstoreoc/Control-elements--Indexing-mechanisms-with-stop-and-positioning-device--GN200-A#listtype=search&term=GN%20200http://tripleellc.com/products/rotary-lock-system/.

ESSP. 2018. 'Rotary Lock ', Accessed 10/10. https://www.eesp.co/html/Downloads/PDF/A44_45.pdf.

Ferreira, L M., J A. Johnson, and G J. W. King. 2010. 'Development of an active elbow flexion simulator to evaluate joint kinematics with the humerus in the horizontal position', *Journal of Biomechanics*, 43: 2114-19.

Fujie, H, G A. Livesay, M Fujita, and S L. Y. Woo. 1996. 'Forces and moments in six-DOF at the human knee joint: Mathematical description for control', *Journal of Biomechanics*, 29: 1577-85.

Fujie, H, K Mabuchi, S L. Y. Woo, G A. Livesay, S Arai, and Y Tsukamoto. 1993. 'The Use of Robotics Technology to Study Human Joint Kinematics: A New Methodology', *Journal of Biomechanical Engineering*, 115: 211-17.

Fujie, H, T Sekito, and A Orita. 2004. 'A Novel Robotic System for Joint Biomechanical Tests: Application to the Human Knee Joint', *Journal of Biomechanical Engineering*, 126: 54-61.

Fujie, H, S L. Y. Woo, G A. Livesay, and K Mabuchi. 1994. 'Application of Robotics to Studies of Joint Biomechanics.' in Yasusuke Hirasawa, Clement Blount Sledge and Savio Lau-Yuen Woo (eds.), *Clinical Biomechanics and Related Research* (Springer Japan: Tokyo).

Fukubayashi, T, P. A. Torzilli, M. F. Sherman, and R Warren. 1982. *An in vitro biomechanical evaluation of anterior-posterior motion of the knee. Tibial displacement, rotation, and torque*.

Furqan, M, M Suhaib, and N Ahmad. 2017. 'Studies on Stewart platform manipulator: A review', *Journal of Mechanical Science and Technology*, 31: 4459-70.

Goertzen, D J., and G N. Kawchuk. 2009. 'A novel application of velocity-based force control for use in robotic biomechanical testing', *Journal of Biomechanics*, 42: 366-69.

Goldsmith, M T., M T. Rasmussen, T Lee Turnbull, C A. C. T, R F. LaPrade, M J. Philippon, and C A. Wijdicks. 2015. 'Validation of a six degree-of-freedom robotic system for hip in vitro biomechanical testing', *Journal of Biomechanics*, 48: 4093-100.

Goldsmith, Mary T., Sean D. Smith, Kyle S. Jansson, Robert F. LaPrade, and Coen A. Wijdicks. 2014. 'Characterization of robotic system passive path repeatability during specimen removal and reinstallation for in vitro knee joint testing', *Medical Engineering & Physics*, 36: 1331-37.

Grassmann, R. Stephanie, R. T Oxland, R. U Gerich, and R. L- P. Nolte. 1998. 'Constrained Testing Conditions Affect the Axial Rotation Response of Lumbar Functional Spinal Units', *Spine*, 23: 1155-62.

Hahn, D, M Olvermann, J Richtberg, W Seiberl, and A Schwirtz. 2011. 'Knee and ankle joint torque–angle relationships of multi-joint leg extension', *Journal of Biomechanics*, 44: 2059-65.

Harmonicdrive. 2018. 'SHA-SG Rotary Actuator', Harmonic Drive, Accessed 10/10. http://www.harmonicdrive.net/products/rotary-actuators/hollow-shaft-actuators/sha-sg.

Hocking, B. 2015. 'Mechanical Design to Increase the Range of Motion Capabilities of the Biomechanics Hexapod Robot', Flinders University

Honeywell. 2018. 'SPS-R360D-NBMS0101', Accessed 10/10. https://sensing.honeywell.com/SPS-R360D-NBMS0101-smart-position-sensors-sps-series.

Hoy, D, J-A Geere, F Davatchi, B Meggitt, and L H. Barrero. 2014. 'A time for action: Opportunities for preventing the growing burden and disability from musculoskeletal conditions in low- and middle-income countries', *Best Practice & Research Clinical Rheumatology*, 28: 377-93.

Johnson, J A., D A. Rath, C E. Dunning, S E. Roth, and G J. W. King. 2000. 'Simulation of elbow and forearm motion in vitro using a load controlled testing apparatus', *Journal of Biomechanics*, 33: 635-39.

KUKA. 2018. 'KR 60', Accessed 04/02/2018. https://www.kuka.com/en-au/products/robotics-systems/industrial-robots/kr-60.

Lawless, I. M., B. Ding, B. S. Cazzolato, and J. J. Costi. 2014. 'Adaptive velocity-based six degree of freedom load control for real-time unconstrained biomechanical testing', *Journal of Biomechanics*, 47: 3241-47.

Leatt. 2018. 'Knee braces C-Frame pro carbon pair', Accessed 10/10. https://www.leatt.com/shop/moto/knee-braces/knee-brace-c-frame-pro-carbon-pair.html.

Lertwanich, P, A Plakseychuk, S Kramer, M Linde-Rosen, A Maeyama, F H. Fu, and P Smolinski. 2016. 'Biomechanical evaluation contribution of the acetabular labrum to hip stability', *Knee Surgery, Sports Traumatology, Arthroscopy*, 24: 2338-45.

Lewis, J. L., W. D. Lew, and J. Schmidt. 1988. 'Description and Error Evaluation of an In Vitro Knee Joint Testing System', *Journal of Biomechanical Engineering*, 110: 238-48.

Mabuchi, K, H Fujie, Y Yamatoku, M Yamamoto, and T Sasada. 1992. 'A New Methodology with an Application of Robotics to Control the Mechanical Environment Around Experimentally Fractured Bone.' in Shigeo Niwa, Stephan M. Perren and Tomokazu Hattori (eds.), *Biomechanics in Orthopedics* (Springer Japan: Tokyo).

Mae, T, K Shino, T Miyama, H Shinjo, T Ochi, H Yoshikawa, and H Fujie. 2001. 'Single–versus two–femoral socket anterior cruciate ligament reconstruction technique: Biomechanical analysis using a robotic simulator', *Arthroscopy: The Journal of Arthroscopic & Related Surgery*, 17: 708-16.

Marc, J. P, A. C. T Christiano, M T. Goldsmith, T. R Matthew, J. S Adriana, L Sverre, and F. L Robert. 2017. 'Biomechanical Assessment of Hip Capsular Repair and Reconstruction Procedures Using a 6 Degrees of Freedom Robotic System', *The American Journal of Sports Medicine*, 45: 1745-54.

Motiontech. 2018. 'Spinea Twinspin Bearing Reducer ', Accessed 2018. http://www.motiontech.com.au/products/spinea-twinspin-bearing-reducer/.

Mutnal, A, B M. Leo, L Vargas, R W. Colbrunn, R S. Butler, and J W. Uribe. 2015. 'Biomechanical Analysis of Posterior Cruciate Ligament Reconstruction With Aperture Femoral Fixation', *Orthopedics (Online)*, 38: 9-16.

Noble, Jr L D., R W. Colbrunn, D-G Lee, A J. van den Bogert, and B L. Davis. 2010. 'Design and Validation of a General Purpose Robotic Testing System for Musculoskeletal Applications', *Journal of Biomechanical Engineering*, 132: 025001-01-12.

Ohori, T, T Mae, K Shino, Y Tachibana, H Fujie, H Yoshikawa, and K Nakata. 2017. *Varus-valgus instability in the anterior cruciate ligament-deficient knee: effect of posterior tibial load*.

Philippon, Marc J., Christiano A. C. Trindade, Mary T. Goldsmith, Matthew T. Rasmussen, Adriana J. Saroki, Sverre Løken, and Robert F. LaPrade. 2017. 'Biomechanical Assessment of Hip Capsular Repair and Reconstruction Procedures Using a 6 Degrees of Freedom Robotic System', *The American Journal of Sports Medicine*, 45: 1745-54.

Qi, W, A Hosseini, T-Y Tsai, J-S Li, H E. Rubash, and G Li. 2013. 'In vivo kinematics of the knee during weight bearing high flexion', *Journal of Biomechanics*, 46: 1576.

Roaas, A, and G B. J. Andersson. 1982. 'Normal Range of Motion of the Hip, Knee and Ankle Joints in Male Subjects, 30–40 Years of Age', *Acta Orthopaedica Scandinavica*, 53: 205-08.

Scully, T. 2012. 'To the limit: more people are surviving to older ages than ever before, pushing life expectancy from birth to unprecedented highs. Further gains will require tackling age-related conditions, across the world, with ramifications for society as a whole', *Nature*, 492: S2+.

Stokes, I A., M Gardner-Morse, D Churchill, and J P. Laible. 2002. 'Measurement of a spinal motion segment stiffness matrix', *Journal of Biomechanics*, 35: 517-21.

Sun, Y, S Wei, Y Zhong, W Fu, L. I. Li, and Y. U. Liu. 2015. 'How Joint Torques Affect Hamstring Injury Risk in Sprinting Swing–Stance Transition', *Medicine and Science in Sports and Exercise*, 47: 373-80.

Tashjian, R Z. 2016. *The Unstable Elbow : An Evidence-Based Approach to Evaluation and Management* (Cham: Springer International Publishing: Cham).

Thomas, J. W, J. H Laura, M. W Edward, and A. A-M James. 2006. 'The Relationship between Quadriceps Muscle Force, Knee Flexion, and Anterior Cruciate Ligament Strain in an in Vitro Simulated Jump Landing', *The American Journal of Sports Medicine*, 34: 269-74.

Ünal, M, O Akkuş, and R E. Marcus. 2016. 'Fundamentals of Musculoskeletal Biomechanics.' in Feza Korkusuz (ed.), *Musculoskeletal Research and Basic Science* (Springer International Publishing: Cham).

UNFPA. 2009. 'United Nations Population Fund (UNFPA). 2009. State of the World Population Report 2009, Facing a Changing World: Women, Population and Climate.(RESOURCES FROM THE INFORMATION & DOCUMENTATION CENTRE)(Report)', *Arrows For Change*, 15: 9.

Van Arkel, R J., and J R. T. Jeffers. 2016. 'In vitro hip testing in the International Society of Biomechanics coordinate system', *Journal of Biomechanics*, 49: 4154-58.

Verstraete, M A., and J Victor. 2015. 'Possibilities and limitations of novel in-vitro knee simulator', *Journal of Biomechanics*, 48: 3377-82.

Walker, M, and J Dickey. 2007. 'New methodology for multi-dimensional spinal joint testing with a parallel robot', *Medical & Biological Engineering & Computing*, 45: 297-304.

WHO, World Health Organization. 2011. 'Obesity and Overweight factsheet from the WHO ', Accessed 21/11/2017. http://www.thehealthwell.info/node/82914.

Wijdicks, C A., M T. Goldsmith, K S. Jansson, S D Smith, L Engebretsen, and R F. LaPrade. 2013. 'Biomechanical Comparison of Anatomic Single and Double Bundle ACL Reconstructions: An In Vitro Study', *Arthroscopy: The Journal of Arthroscopic & Related Surgery*, 29: e37-e38.

Woo, S L. Y., R E. Debski, E K. Wong, M Yagi, and D Tarinelli. 1999. 'Use of robotic technology for diathrodial joint research', *Journal of Science and Medicine in Sport*, 2: 283-97.

Woo, S L. Y., and M B. Fisher. 2009. 'Evaluation of Knee Stability with Use of a Robotic System', *The Journal of Bone and Joint Surgery. American volume.*, 91: 78-84.

Woolf, A D., and B Pfleger. 2003. 'Burden of major musculoskeletal conditions', *Bulletin of the World Health Organization*, 81: 646-56.

Woolf, A. 2000. 'The Bone and Joint Decade 2000-2010', *Annals of the Rheumatic Diseases*, 59: 81-82.

Zavatsky, A. B. 1997. 'A kinematic-freedom analysis of a flexed-knee-stance testing rig', *Journal of Biomechanics*, 30: 277-80.

Zhong, Y, W Fu, S Wei, Q Li, and Y Liu. 2017. 'Joint Torque and Mechanical Power of Lower Extremity and Its Relevance to Hamstring Strain during Sprint Running', *Journal of Healthcare Engineering*, 2017: 8927415.

Appendix

Appendix A. MATLAB Code

```
%----- Calculating 7DOF geometry static-----%
% Tiffany Teh 2018 Dynamic
% Input the robots end effector pose and cradle position.
%
% This code will determine the encoder leg lengths, and vector, their position in
the
% coordinate system, the cradle base and motor position, and the relationship
between
% cradle base and encoder lengths.
%
% edit the height of the robot end-effector with respect to the base at middle
stroke.
%
% Axis: x,y,z. {0,0,0} is at base middle of hexagon
% output units mm and deg

%%%----- hexapod cyclic motion
r_deg = 10; %cyclic
no = linspace(0,2*pi,50);
f = r_deg*sin(no);
%%%---- cradle cyclic or kinematic
%cyclic
% FA_deg = 25
% num = linspace(0,2*pi,50)
% n = FA_deg*sin(num)
num = xlsread('knee_kinematics.xlsx')
%n = num(:,2)
%%%%----- vid
enc_to_crad = [];
v = VideoWriter('newfile_dynRxyz.avi','Motion JPEG AVI');
v.FrameRate = 15;
open(v)
for i = 1:length(num(:,2))
%%% --------- Input static pose
%
p = [0 0 0 f(i) 0 0]';%robot end effector pose
FA = num(i,2);
%%% ---------- Define cradle geometry
%
BOS_w = 130; %base of stand width
BOS_l = 162; %base of stand length
c_0 = 50;    %middle of base of cradle (top of first specimen pillar)
BOS_to_COR = 190; %cradle stand
COR_to_CB = 170; %length from COR to cradle base
CB_l = 70; %cradle base length
CB_w = 50; %cradle base width
%%% -------- Define encoder geometry
%
BM_t = 14.35;  %base mount thickness
BM_l = 230;    %length of base mount
R_t = 34;      %reader thickness
R_l = 48;      %reader length
GS_t = 10.2;   %glass scale thickness
GS_l = 161;    %glass scale thickness
MR_t = 4.7;    %minature rail thickness
%%% ----------- Encoder geometry - put in code to calculate the encoder End
Position Matrices
% Note that 0 is base and 1 is top
% This section is extracted from Boyin Dings (hexapod developer) inverse
```

```
% kinematics code (2015)
%
xe0 = 6.855;            % encoder base leg 1 x point
ye0 = 316.867;          % encoder base leg 1 y point
%
xe1 = 125.834;          % encoder top leg 1 x point
ye1 = 82.0440;          % encoder top leg l y point
%
%return a 3x6 matrix for all 6 leg hexagon coordinate
E0 = geom(xe0,ye0);        %calculates end coordinates (only x, y) for bottom
hexagon
E1 = geom(xe1,ye1);         %calculates end cooridnates (only x,y) for top hexagon
%
% Rotation Matrix
r = p(4:6);
deg2rad = pi/180;       % Conversion from degrees to radians
M0 = rotxyz(r*deg2rad);
%
% Offset Vector
d = [0; 0; 520]+p(1:3);    % Height of top platform with respect to the base plate,
mm
D0 = repmat(d,1,6);
TP0 = [p(1); p(2) ; D0(3)-p(3)]; %top platform coordinate
%
% Encoder Link Vector
VE0 = M0*E1+D0-E0;  %the directional vector of each leg
%
% Lengths of Encoder Links
LE0 = sqrt(sum(VE0.*VE0)); %length of each leg

%----------------plot encoders points
%
 figure;
for j = 1:6
    top_point = E0(:,j) + VE0(:,j);
    encoder = [E0(:,j)';top_point'];
    plot3(encoder(:,1), encoder(:,2), encoder(:,3),'black')
    hold on
end

hold on;
rotate3d on;
grid on;
az = 190;
el = 10;
view(az, el);
xlabel ('X mm')
ylabel ('Y mm')
zlabel ('Z mm')
title('Kinematic flexion, Hexapod Rx ±10°')
hold on
%real encoder geometry - inside
for k =1:6
r_ = [0 -90 0];            %rotate
M0_ = rotxyz(r_*deg2rad);  %rotate encoder line
perpen_EV = M0_*E1(:,k)-E0(:,k); %encoder vector rotated - perpendicular
unitEV(:,k) = VE0(:,k)/norm(VE0(:,k));  %unit vector of encoder
%base mount (BM)
para_OBM(:,k) = E0(:,k)+perpen_EV./norm(perpen_EV).*BM_t/2; %new line to certain
distance
paraVE_BM(:,k) = para_OBM(:,k) + unitEV(:,k)*BM_l; %new parallel line for base
mount
hold on;
plot3([E0(1,k) para_OBM(1,k)],[E0(2,k) para_OBM(2,k)],[E0(3,k) para_OBM(3,k)]);
hold on;
plot3([para_OBM(1,k) paraVE_BM(1,k)],[para_OBM(2,k) paraVE_BM(2,k)],[para_OBM(3,k)
paraVE_BM(3,k)]);
%reader and read switch mount (R)
```

```
pt_2 = E0(:,k)+VE0(:,k)/norm(VE0(:,k))*BM_l;  %define new point
para_OR(:,k) = pt_2 + perpen_EV./norm(perpen_EV).*R_t/2; %new perpendicular line
paraVE_R(:,k) = para_OR(:,k) + unitEV(:,k)*R_l; %new parallel line
hold on
plot3([pt_2(1) para_OR(1,k)],[pt_2(2) para_OR(2,k)],[pt_2(3) para_OR(3,k)])
hold on
plot3([para_OR(1,k) paraVE_R(1,k)],[para_OR(2,k) paraVE_R(2,k)],[para_OR(3,k)
paraVE_R(3,k)])
%glass scale (GS)
pt_3 = E0(:,k)+VE0(:,k)/norm(VE0(:,k))*(BM_l+R_l);  %define new point
para_OGS(:,k) = pt_3 + perpen_EV./norm(perpen_EV).*GS_t/2; %new perpendicular line
paraVE_GS(:,k) = para_OGS(:,k) + unitEV(:,k).*GS_l; %new parallel line
hold on;
plot3([pt_3(1) para_OGS(1,k)],[pt_3(2) para_OGS(2,k)],[pt_3(3) para_OGS(3,k)])
hold on;
plot3([para_OGS(1,k) paraVE_GS(1,k)],[para_OGS(2,k) paraVE_GS(2,k)],[para_OGS(3,k)
paraVE_GS(3,k)])
%Minature Rail (MR)
pt_4 = E0(:,k)+VE0(:,k)/norm(VE0(:,k))*(BM_l+R_l+GS_l);  %define new point
para_OMR(:,k) = pt_4 + perpen_EV./norm(perpen_EV).*MR_t/2; %new perpendicular line
paraVE_MR(:,k) = para_OMR(:,k) + unitEV(:,k).*(LE0(k)-(BM_l+R_l+GS_l)); %new
parallel line
hold on;
plot3([pt_4(1) para_OMR(1,k)],[pt_4(2) para_OMR(2,k)],[pt_4(3) para_OMR(3,k)])
hold on;
plot3([para_OMR(1,k) paraVE_MR(1,k)],[para_OMR(2,k) paraVE_MR(2,k)],[para_OMR(3,k)
paraVE_MR(3,k)])
hold on;
end


%%% ------ base and stand plot---------
%%% points of cradle stand and base
b1 = [-BOS_w/2 -BOS_l/2 c_0 ]; %rs, b base
b2 = [BOS_w/2 -BOS_l/2 c_0 ];  %ls, b base
b3 = [BOS_w/2 BOS_l/2 c_0 ];   %ls, f base
b4 = [-BOS_w/2 BOS_l/2 c_0 ];  %rs, f base
s1m = [-BOS_w/2 -BOS_l/2 c_0+BOS_to_COR]; %motor f  stand
s2m = [BOS_w/2 -BOS_l/2 c_0+BOS_to_COR ]; %motor f stand
s1 = [BOS_w/2 BOS_l/2 c_0+BOS_to_COR ]; %b stand
s2 = [-BOS_w/2 BOS_l/2 c_0+BOS_to_COR ]; %b stand
rectangle_plot(b1,b2,b3,b4)
rectangle_plot(b1,s1m,s2m,b2)
rectangle_plot(b3,s1,s2,b4)
%%% actual cradle relationship --------
theta = FA*pi/180; %flexion angle rad
ninety = 90*pi/180; %90 deg
c_m = [0 0 c_0+BOS_to_COR];                                    %COR cradlde mid
c_mb = [-COR_to_CB*sin(theta) 0 (c_0+BOS_to_COR)-(COR_to_CB*cos(theta))]';   %point
for base at an angle
cradle_mid = [c_m; c_mb'];
plot3(cradle_mid(:,1), cradle_mid(:,2), cradle_mid(:,3),'black') %line for specimen
bottom
%---- cradle base
if FA <= 90
c_b1 = [-COR_to_CB*sin(theta)+CB_w*cos(theta) CB_l (c_0+BOS_to_COR)-
(COR_to_CB*cos(theta))-CB_w*sin(theta)]'; %ls,f
c_b2 = [-COR_to_CB*sin(theta)-CB_w*cos(theta) CB_l (c_0+BOS_to_COR)-
(COR_to_CB*cos(theta))+CB_w*sin(theta)]' ;%rs,f
c_b3 = [-COR_to_CB*sin(theta)+CB_w*cos(theta) -CB_l (c_0+BOS_to_COR)-
(COR_to_CB*cos(theta))-CB_w*sin(theta)]'; %ls,b
c_b4 = [-COR_to_CB*sin(theta)-CB_w*cos(theta) -CB_l (c_0+BOS_to_COR)-
(COR_to_CB*cos(theta))+CB_w*sin(theta)]'; %rs,b
rectangle_plot(c_b3,c_b4,c_b2, c_b1) %plot cradle base
elseif FA > 90
c_b1 = [-COR_to_CB*sin(theta)-CB_w*cos(ninety-(theta-ninety)) CB_l
(c_0+BOS_to_COR)-(COR_to_CB*cos(theta))-CB_w*sin(ninety-(theta-ninety))]'; %ls,f
```

```
c_b2 = [-COR_to_CB*sin(theta)+CB_w*cos(ninety-(theta-ninety)) CB_l
(c_0+BOS_to_COR)-(COR_to_CB*cos(theta))+CB_w*sin(ninety-(theta-ninety))]'; %rs,f
c_b3 = [-COR_to_CB*sin(theta)-CB_w*cos(ninety-(theta-ninety)) -CB_l
(c_0+BOS_to_COR)-(COR_to_CB*cos(theta))-CB_w*sin(ninety-(theta-ninety))]'; %ls,b
c_b4 = [-COR_to_CB*sin(theta)+CB_w*cos(ninety-(theta-ninety)) -CB_l
(c_0+BOS_to_COR)-(COR_to_CB*cos(theta))+CB_w*sin(ninety-(theta-ninety))]'; %rs,b
rectangle_plot(c_b3,c_b4,c_b2, c_b1) %plot cradle base
end
%-------finding encoder distance to cradle base
unitV_CB = (c_b2-c_b1)/norm(c_b2-c_b1); %defining a vector
unitV_CB(isnan(unitV_CB))=0;
if c_b2(3)>= (BM_l+R_l) %extends beyond base mount + reader, find all 3 distances
    %glass scale RS cradle
    t_rsGS = (c_b2(3)-para_OGS(3,2) )/unitEV(3,2);  %determine t parametric
    x_rsGS = para_OGS(1,2) + t_rsGS*unitEV(1,2);    %calculate x encoder
coordinates
    y_rsGS = para_OGS(2,2) + t_rsGS*unitEV(2,2);    %calculate y encoder
coordinates
    enGS = [x_rsGS y_rsGS c_b2(3)];                   %coordinate of closest
encoder to CB
    distGS_r = c_b2(1) - x_rsGS
    if c_b2(3)> para_OR(3,2) && c_b2(3) <paraVE_R(3,2)
    %reader RS cradle   (have encoder coordinates, find cradle coordinates)
    t_rsR = (paraVE_R(3,2)-c_b1(3))/((c_b2(3)-c_b1(3))./norm(c_b2-c_b1));
    x_rsR = c_b1(1)+unitV_CB(1)*t_rsR;
    y_rsR = c_b1(2)+unitV_CB(2)*t_rsR;
    distR_r = x_rsR - paraVE_R(1,2)
    end
    if FA < 90
    %base mount
    t_rsBM = (paraVE_BM(3,2)-c_b1(3))/((c_b2(3)-c_b1(3))./norm(c_b2-c_b1));
    x_rsBM = c_b1(1)+unitV_CB(1)*t_rsBM;
    y_rsBM = c_b1(2)+unitV_CB(2)*t_rsBM;
    distBM = x_rsBM - paraVE_BM(1,2)
    end
    if FA > 90
     if c_b1(3)>= para_OGS(3,2) && c_b1(3)<= paraVE_GS(3,2)
     %glass scale LS cradle
     t_lsGS = (c_b1(3)-para_OGS(3,2) )/unitEV(3,2);%determine t parametric
     x_lsGS = para_OGS(1,2) + t_lsGS*unitEV(1,2);    %calculate x encoder
coordinates
     y_lsGS = para_OGS(2,2) + t_lsGS*unitEV(2,2);    %calculate y encoder
coordinates
     distGS_l = c_b1(1) - x_lsGS
     end
     if c_b1(3)> para_OR(3,2) && c_b1(3) <paraVE_R(3,2)
     %reader LS cradle
     t_lsR = (c_b1(3)-para_OR(3,2) )/unitEV(3,2);%determine t parametric
     x_lsR = para_OR(1,2) + t_lsR*unitEV(1,2);    %calculate x encoder coordinates
     y_lsR = para_OR(2,2) + t_lsR*unitEV(2,2);    %calculate y encoder coordinates
     distR_l = c_b1(1) - x_lsR
     end
    end
 ans = min([ distGS_l distR_l distBM distR_r distGS_r]
elseif c_b2(3)>= BM_l && c_b2(3)< (BM_l+R_l)
    %reader
    t_rsR = (c_b2(3)-para_OR(3,2) )/unitEV(3,2);
    x_rsR = para_OR(1,2) + t_rsR*unitEV(1,2);    %calculate x encoder coordinates
    y_rsR = para_OR(2,2) + t_rsR*unitEV(2,2);    %calculate y encoder coordinates
    enGS = [x_rsR y_rsR c_b2(3)];                   %coordinate of closest encoder
to CB
    distGS = c_b2(1) - x_rsR
    %base mount
    t_rsBM = (paraVE_BM(3,2)-c_b1(3))/((c_b2(3)-c_b1(3))./norm(c_b2-c_b1));
    x_rsBM = c_b1(1)+unitV_CB(1)*t_rsBM;
    y_rsBM = c_b1(2)+unitV_CB(2)*t_rsBM;
    distBM = x_rsBM - paraVE_BM(1,2)
    ans = min([distBM distGS ];
```

```
elseif c_b2(3)< BM_l %just find base mount distance to encoder
    t_rsBM = (c_b2(3)-para_OBM(3,2) )/unitEV(3,2);
    x_rsBM = para_OBM(1,2) + t_rsBM*unitEV(1,2);    %calculate x encoder
coordinates
    y_rsBM = para_OBM(2,2) + t_rsBM*unitEV(2,2);    %calculate y encoder
coordinates
    distBM = c_b2(1) - x_rsBM;
    ans = distBM;
end
%
if LE0>=644
    disp('encoder maximum reached')
end
enc_to_crad(i) = ans;
    %----
    %table
 %h1 = figure();
 set(gcf,'Visible', 'off');
set(gca,'position',[0.12 0.12 0.64 0.72])
 M(i) = getframe(gcf);

  writeVideo(v,M(i))
end
T = table(num(:,2),enc_to_crad')
T.Properties.VariableNames = {'Deg' 'Dist'}
figure;
axes('Visible', 'off')
movie(M,5,10)
close(v)
```

Appendix B. LabVIEW

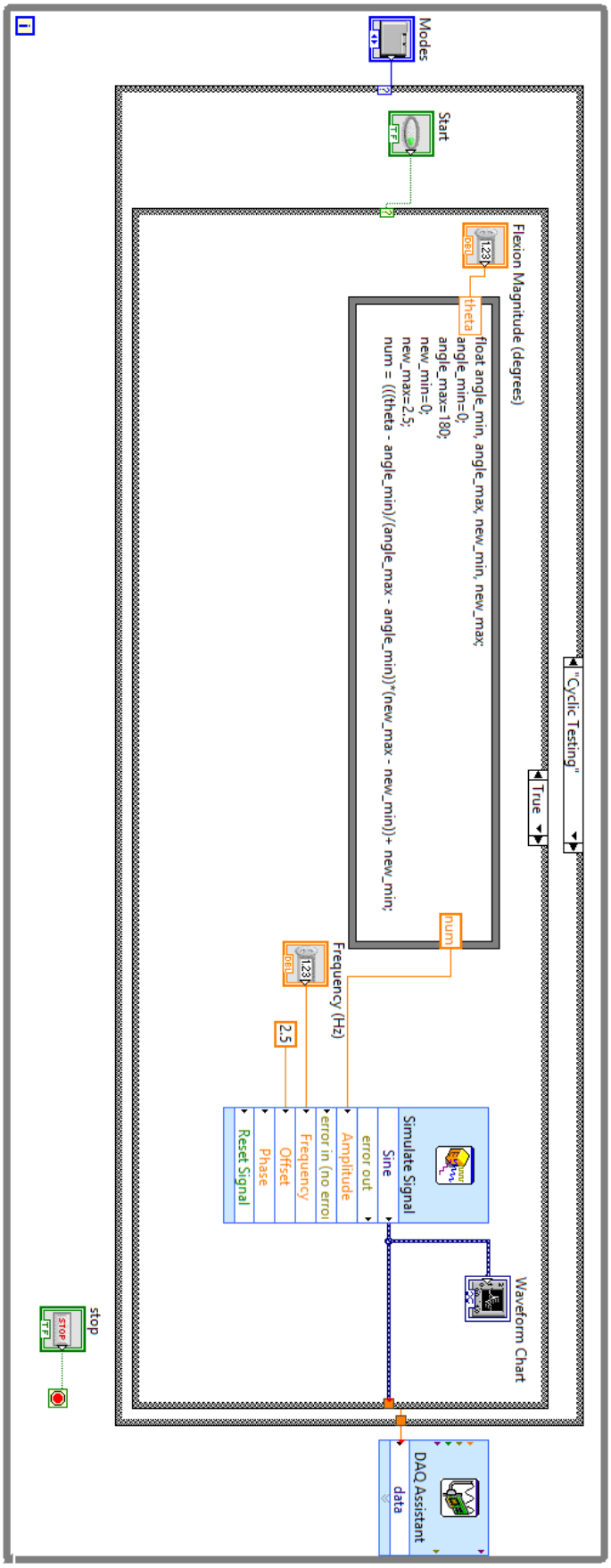

Appendix C. Prototype Design

Cradle prototype drawings.

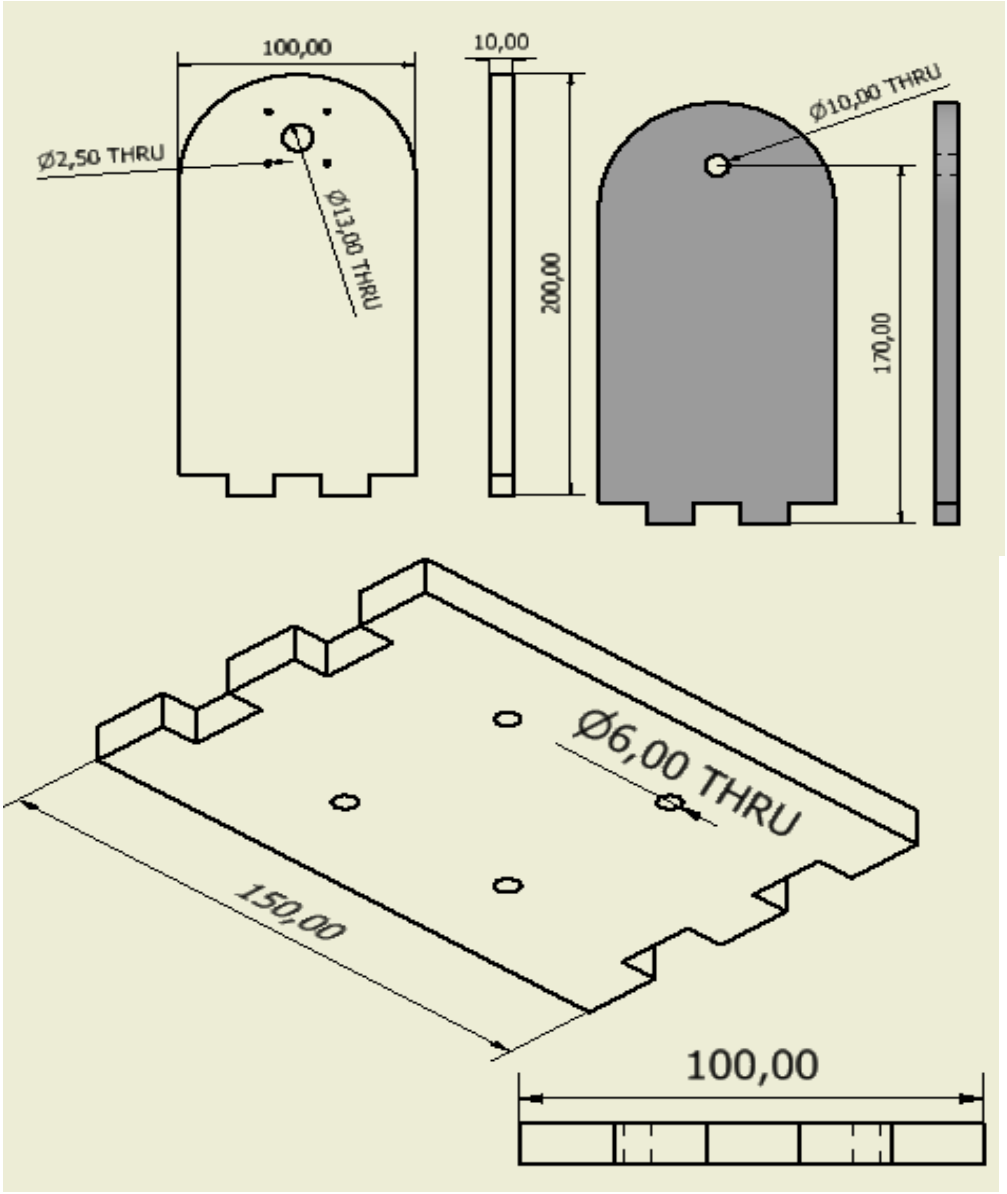

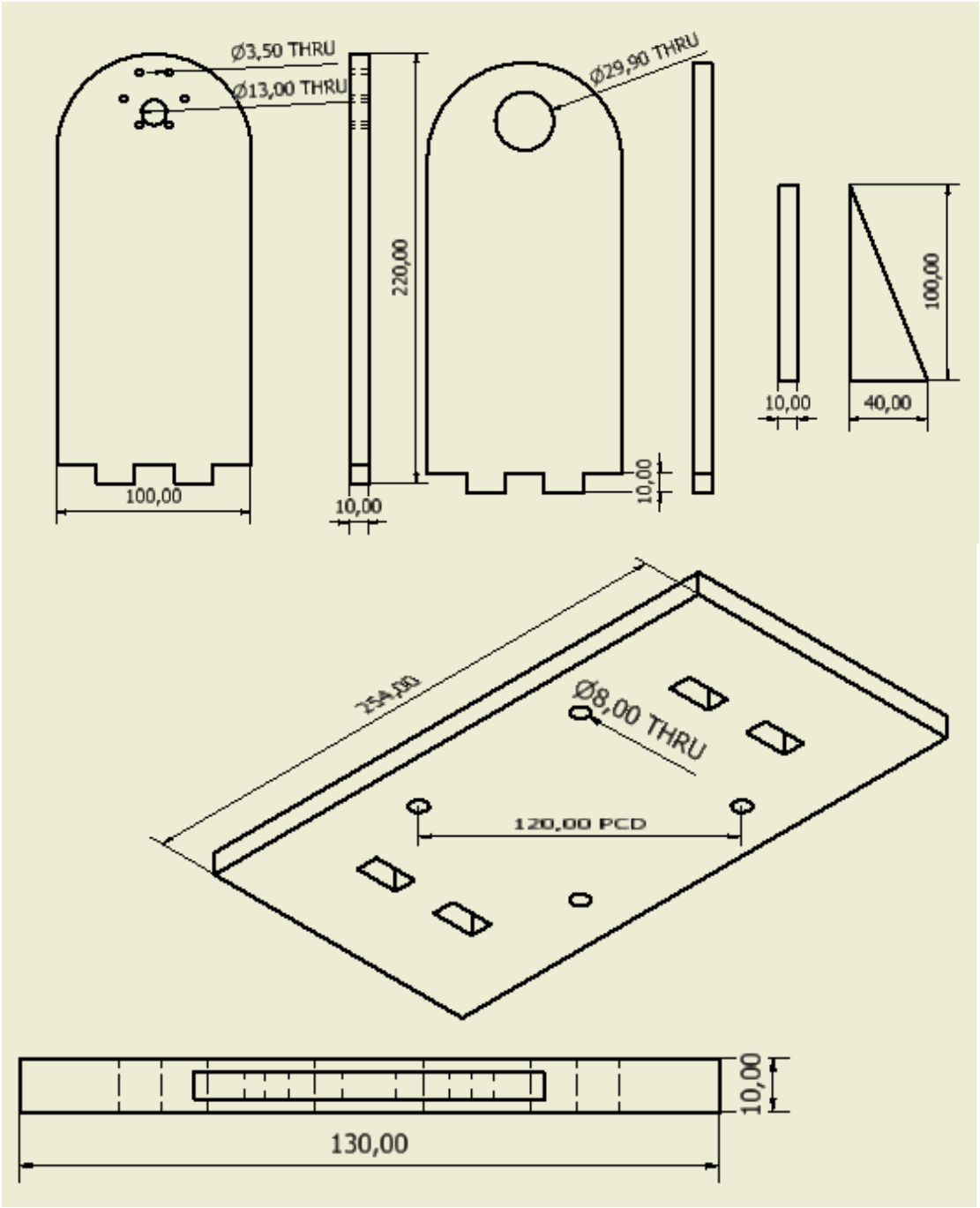
Ø3,50 THRU
Ø13,00 THRU
220,00
Ø29,90 THRU
100,00
10,00
10,00
10,00
40,00
100,00
254,00
Ø8,00 THRU
120,00 PCD
10,00
130,00

Appendix D. SHA Actuator Specifications and Drawing

Exert from Harmonic Drive website catalogue for SHA Actuator. (Harmonicdrive 2018)

SG/HP type

Item \ Model		SHA25A (Motor input voltage 100V)					SHA25A (Motor input voltage 200V)					
		51	81	101	121	161	11	51	81	101	121	161
Servo Drive		REL-230-18 HA-800□-6D/E-100					REL-230-18 REL-230-36 HA-800□-3D/E-200					
Max. torque*1	Nm	127	178	204	217	229	26	127	178	204	217	229
	kgf·m	13	18.2	20.8	22.1	23.4	2.7	13	18.2	20.8	22.1	23.4
Allowable continuous torque*1*2	Nm	35	58	73	81	81	9.0	41	67	81	81	81
	kgf·m	3.6	5.9	7.4	8.2	8.2	0.92	4.2	6.8	8.2	8.2	8.2
Max. rotational speed*1	rpm	94.1	59.3	47.5	39.7	29.8	509.1	109.8	69.1	55.4	46.3	34.8
Torque constant*1	Nm/A	11.1	17.9	22	27	36	4.2	19	31	39	46	62
	kgf·m/A	1.1	1.8	2.3	2.7	3.6	0.43	2.0	3.2	4.0	4.7	6.3
Max. current*1	A	14.9	13.0	12.1	10.9	9.0	8.9	8.6	7.5	7.0	6.3	5.2
Allowable continuous current*1*2	A	4.7	4.7	4.7	4.5	3.7	3.0	3.0	3.0	2.9	2.6	2.1
EMF constant*3	V/(rpm)	1.3	2.0	2.5	3.0	4.0	0.47	2.2	3.5	4.3	5.2	6.9
Phase resistance (20℃)	Ω	0.4					1.2					
Phase inductance	mH	1.0					3					
Inertia moment (without brake) GD²/4	kg·m²	0.56	1.4	2.2	3.2	5.6	0.029	0.56	1.4	2.2	3.2	5.6
Inertia moment (without brake) J	kgf·cm·s²	5.7	14	22	32	57	0.30	5.7	14	22	32	57
Inertia moment (with brake) GD²/4	kg·m²	0.66	1.7	2.6	3.7	6.6	0.034	0.66	1.7	2.6	3.7	6.6
Inertia moment (with brake) J	kgf·cm·s²	6.7	17	26	38	67	0.35	6.7	17	26	38	67
Reduction ratio		1:51	1:81	1:101	1:121	1:161	1:11	1:51	1:81	1:101	1:121	1:161
Permissible moment load	Nm	258					410	258				
	kgf·m	26.3					41.8	26.3				
Moment stiffness	Nm/rad	39.2×10^4					37.9×10^4	39.2×10^4				
	kgf·m/arc min	11.6					11.3	11.6				
One-way positional accuracy	Sec.	50	40	40	40	40	120	50	40	40	40	40
Encoder type		Magnetic absolute encoder										
Single motor revolution Encoder resolution		2^{17} (131,072)										
Motor multi revolution counter		2^{16} (65,536)										
Output resolution	Pulse/rev	6,684,672	10,616,832	13,238,272	15,859,712	21,102,592	1,441,792	6,684,672	10,616,832	13,238,272	15,859,712	21,102,592
Mass (without brake)	kg	2.95					5.0	2.95				
Mass (with brake)	kg	3.1					5.1	3.1				
Environmental conditions		Operating temperature: 0 to 40℃/Storage temperature: -20 to 60℃ Operating humidity/storage humidity: 20 to 80%RH (no condensation) Resistance to vibration: 25 m/s² (frequency: 10 to 400Hz)/Shock resistance: 300 m/s² *4 No dust, no metal powder, no corrosive gas, no inflammable gas, no oil mist To be used indoors, no direct sunlight Altitude: less than 1,000 m above sea level										
Motor insulation		Insulation resistance: 100MΩ or more (by DC500V insulation tester) Dielectric strength: AC1,500V/1 min Insulation class: A										
Mounting direction		Can be installed in any direction.										
Protection structure		Totally enclosed self-cooled type (IP54)										

The table shows typical output values of actuators.
*1: When combined with a HA-800 driver.
*2: Value after temperature rise and saturation when the 350 x 350 x 18 [mm] aluminum radiation plate is installed.
*3: Value of phase induced voltage constant multiplied by 3.
*4: For testing conditions, refer to [1-12 Shock resistance] (P49) and [1-13 Vibration resistance] (P50).

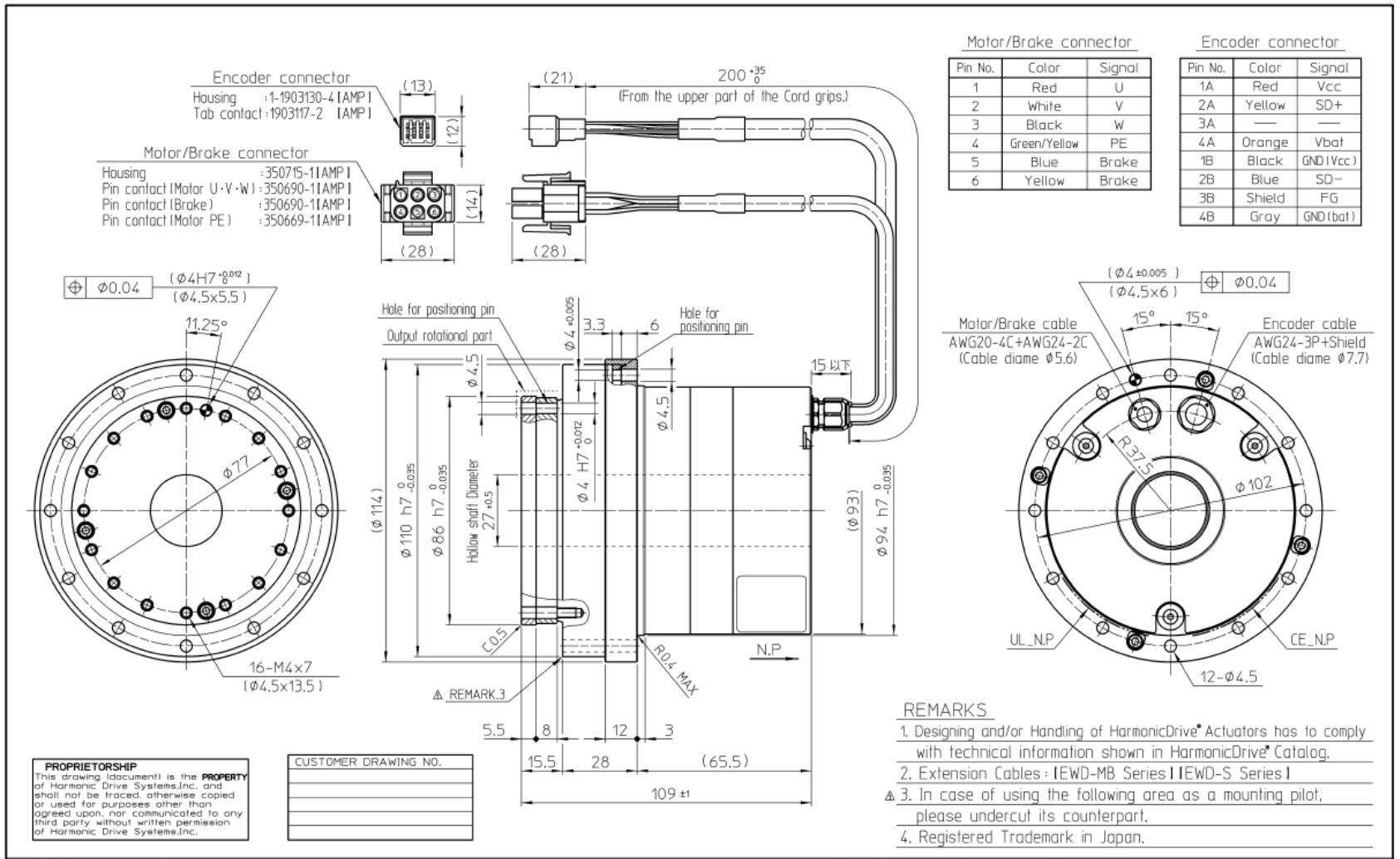

PROPRIETORSHIP
This drawing (document) is the PROPERTY of Harmonic Drive Systems,Inc. and shall not be traced, otherwise copied or used for purposes other than agreed upon, nor communicated to any third party without written permission of Harmonic Drive Systems,Inc.

CUSTOMER DRAWING NO.

REMARKS

1. Designing and/or Handling of HarmonicDrive® Actuators has to comply with technical information shown in HarmonicDrive® Catalog.
2. Extension Cables : (EWD-MB Series) (EWD-S Series)
3. ⚠ In case of using the following area as a mounting pilot, please undercut its counterpart.
4. Registered Trademark in Japan.

訂正 REV	履歴 DESCRIPTION	
1	Change drawing to comply with actual product. Add a Remark.	
仕様 SPEC		尺度 SCALE: Free

機械加工記号公差	0 / 0.5	0.5 / 6	6 / 30	30 / 120	120 / 315	315 / 1000	1000 / 2000
GENERAL TOLERANCE	±0.05	±0.1	±0.2	±0.3	±0.5	±0.8	±1.2

備考 REMARKS : 特記無き角はC0.2以下、すみの丸みはR0.4以下
無記号表面アラサ SURFACES MARKED EXCEPT AS NOTED ▽→▽50S ▽▽→▽▽25S ▽▽▽→▽▽▽6.3S

DWG SIZE	UNIT	THIRD ANG
A3	mm	

設計 DESIGN	Y.Saito	Nov- 7-14
検図 VRFD	N.NAKAMURA	Nov- 7-14
承認 APPD	T.ICHIKAWA	Nov- 7-14

HARMONIC DRIVE SYSTEMS INC TOKYO JAPAN

タイトル TITLE: OUTLINE DRAWING
製品名 ARTICLE: SHA25A81SG-B09B200-10S17bA-C
図番 DWG No: B2T0268 − A

TP-0E3

Appendix E Drawings for Cradle components compatible with SHA actuator

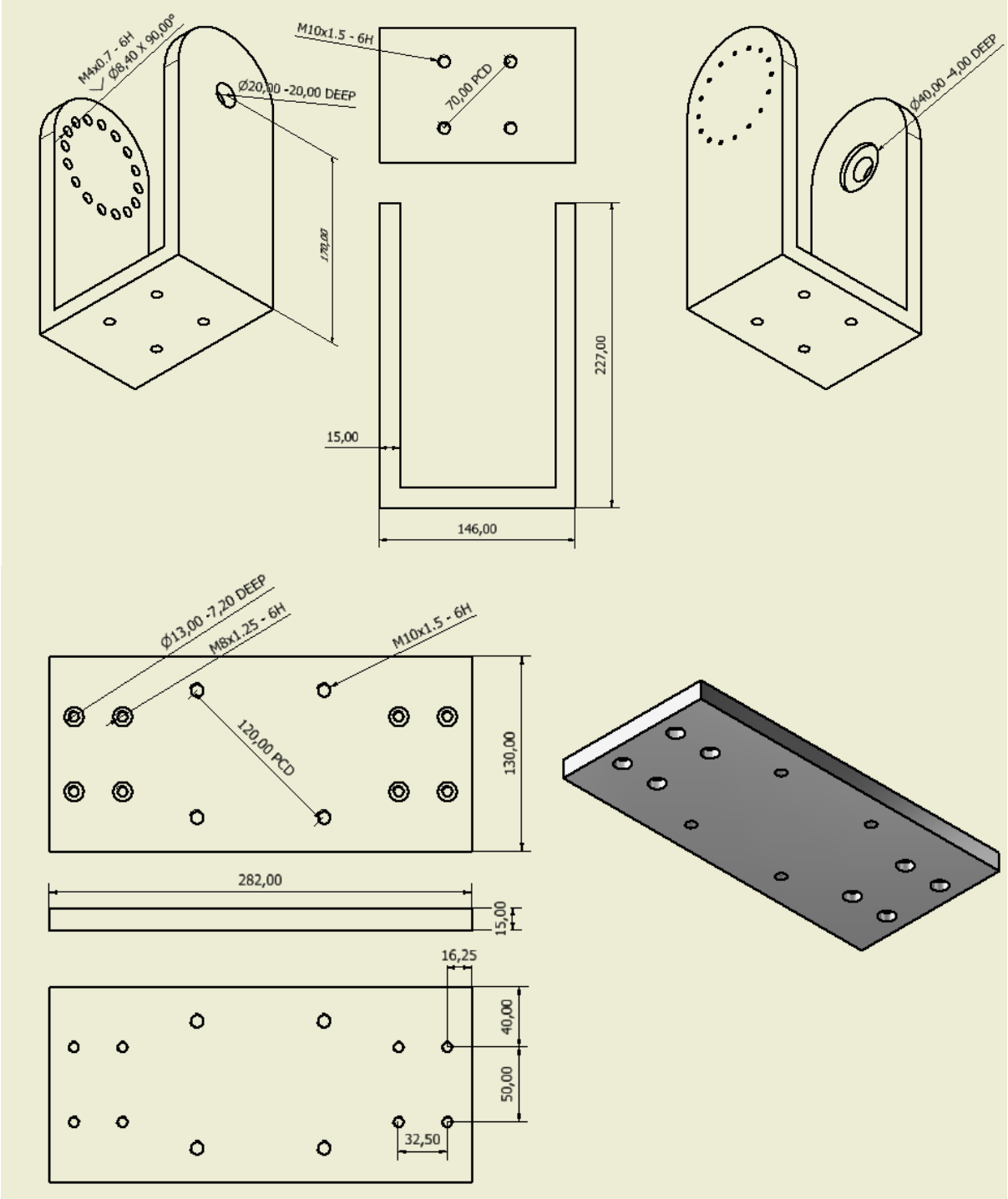

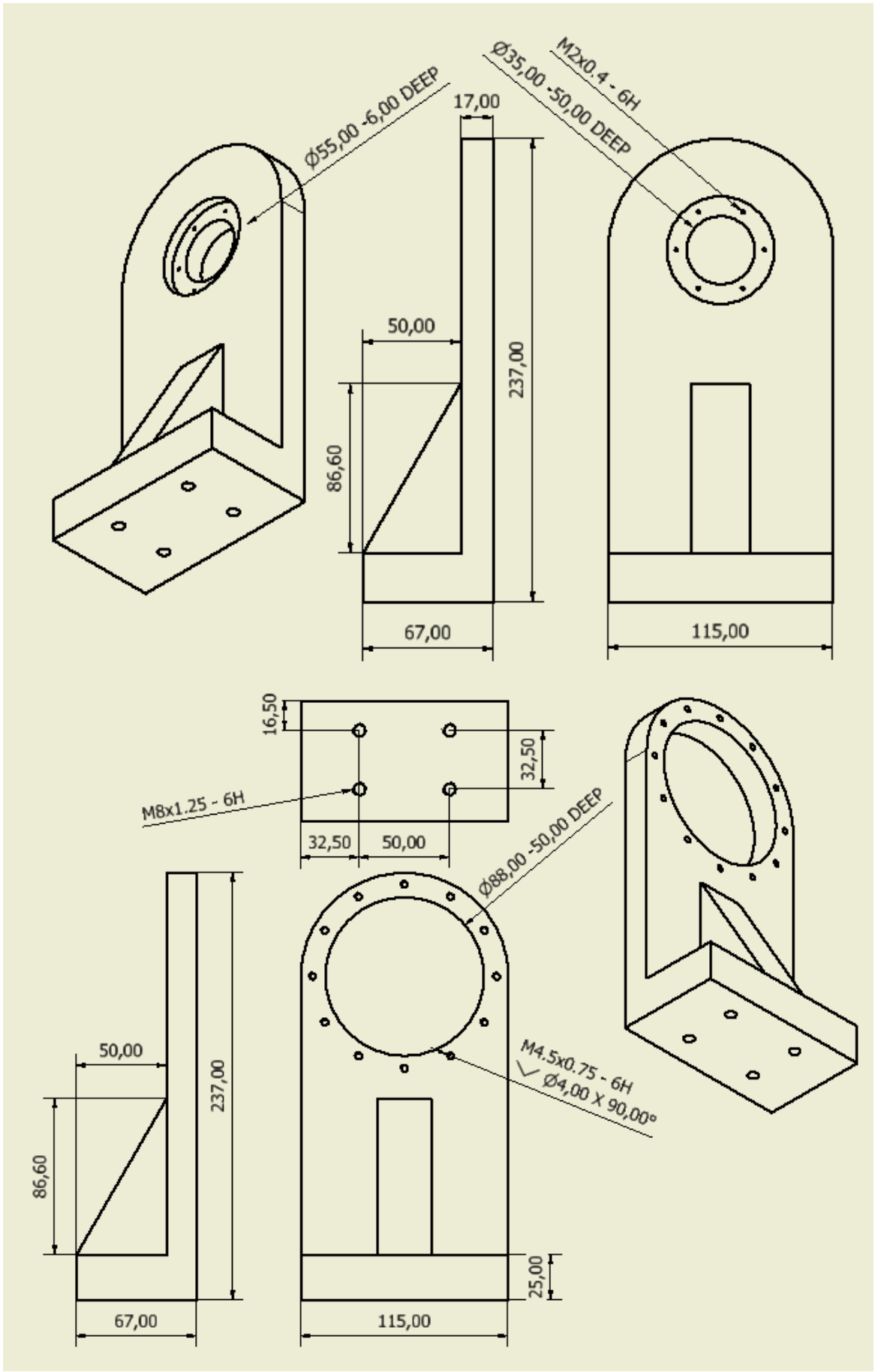
Ø55,00 -6,00 DEEP
Ø35,00 -50,00 DEEP
M2x0.4 - 6H
17,00
50,00
237,00
86,60
67,00
115,00
16,50
32,50
M8x1.25 - 6H
32,50
50,00
Ø88,00 -50,00 DEEP
M4.5x0.75 - 6H
Ø4,00 X 90,00°
25,00